Progress in Materials Science 133 (2023) 101037

Contents lists available at ScienceDirect

Progress in Materials Science

journal homepage: www.elsevier.com/locate/pmatsci

Progress in atomic-resolution aberration corrected conventional transmission electron microscopy (CTEM)

Knut W. Urban [a,*], Juri Barthel [a], Lothar Houben [b], Chun-Lin Jia [c], Lei Jin [a], Markus Lentzen [a], Shao-Bo Mi [d], Andreas Thust [a], Karsten Tillmann [a]

[a] Ernst Ruska-Center for Microscopy and Spectroscopy with Electrons (ER-C), Forschungszentrum Jülich GmbH, 52425 Jülich, Germany
[b] Department of Chemical Research Support, Weizmann Institute of Science, PO Box 26, Rehovot 7610001, Israel
[c] School of Microelectronics, Xi'an Jiaotong University, Xi'an 710049, China
[d] State Key Laboratory for Mechanical Behavior of Materials, Xi'an Jiaotong University, Xi'an 710049, China

ARTICLE INFO

Keywords:
Aberration corrected electron microscopy
Atomic resolution
CTEM
EFTEM
Electron microscopy
Ferroelectrics
In-situ experiments
Oxides

ABSTRACT

Transmission electron microscopy is an indispensable tool in modern materials science. It enables the structure of materials to be studied with high spatial resolution, and thus makes a decisive contribution to the fact that it is now possible to understand the microstructure-related physical and chemical characteristics and to correlate these with the macroscopic materials properties. It was tantamount to a paradigm shift when electron microscopy reached atomic resolution in the late 1990s due to the invention of aberration-corrected electron optics. It is now generally accepted practice to perform picometer-scale measurements and chemical analyses with reference to single atomic units. This review has three objectives. Microscopy in atomic dimensions is applied quantum physics. The consequences of this for practical work and for the understanding and application of the results shall be worked out. Typical applications in materials science will be used to show what can be done with this kind of microscopy and where its limitations lie. In the absence of relevant monographs, the aim is to provide an introduction to this new type of electron microscopy and to enable the reader to access the literature in which special issues are addressed. The paper begins with a brief presentation of the principles of optical aberration correction. It then discusses the fundamentals of atomic imaging and covers typical examples of practical applications to problems in modern materials science. It is emphasized that in atomic-resolution electron microscopy the quantitative interpretation of the images must always be based on the solution of the quantum physical and optical problem on a computer.

1. Introduction and overview

The dimension of modern materials science spans ten orders of magnitude between the picometer and the centimeter range. An indispensable tool for the study of structure-related problems, from the mesoscopic scale down to fractions of atomic dimensions, is transmission electron microscopy. There is hardly an area in physics, chemistry, materials science and engineering in the study of which transmission electron microscopy has not made important, often decisive contributions. However, judging by the number of publications, this field has been in a phase of most intense activity for more than two decades now, unprecedented since the invention

* Corresponding author.
E-mail address: k.urban@fz-juelich.de (K.W. Urban).

https://doi.org/10.1016/j.pmatsci.2022.101037
Received 11 September 2021; Received in revised form 12 October 2022; Accepted 22 October 2022
Available online 4 November 2022

of transmission electron microscopy in the 1930s. The reason for this is a fundamental advancement in electron optics that has dramatically increased the resolving power. This allows the study of materials with true atomic resolution. In parallel, there has been an extraordinarily successful development of quantum physical and optical imaging theory in atomic dimensions. This now allows us to understand microscopic imaging quantitatively to the point that electron microscopy has undergone a paradigm shift from a purely imaging method to a quantitative measurement technique in dimensions that are fractions of atomic distances.

Two different types of microscopes are used in modern transmission electron microscopy. The first is the directly imaging electron microscope as invented by Knoll and Ruska in 1931 [1–3]. In order to distinguish it from the second type of microscope this is termed *conventional transmission electron microscope*. Here the specimen as a whole is illuminated by the electron beam and the image is created all at once in a single shot. The second is the *scanning transmission electron microscope* invented by von Ardenne in 1937 [4,5]. In this instrument, the sample is scanned with a finely focused electron beam whose diameter also determines the resolution. The image is then formed sequentially based on the transmitted electrons, which are registered with various detectors located behind the sample. In either case the quality of electron microscopic imaging is limited by the aberrations of the electron optical lenses employed. Therefore, early on, ways were sought to minimize these aberrations. However, the path to aberration-corrected lenses proved difficult. A particularly critical point was that due to Gauss' law of magnetism it is fundamentally impossible to construct diverging lenses with round magnetic fields. This blocked the path that Abbe had taken in light optics [6], namely to compensate the spherical aberration of a converging lens by combining it together with a suitable diverging lens to form a system whose resulting aberration is negligible. In fact, Scherzer was able to prove in 1936 that for fundamental reasons spherical aberration cannot be avoided in systems with round magnetic lenses [7]. It was also Scherzer who, in 1947, pointed out the path that was subsequently taken, and which was ultimately successful, namely to correct spherical aberration with the aid of multipole lenses [8]. However, it was to take a good 50 years to realize such systems for practical use and thus actually achieve the purpose of such technology, namely to achieve a higher resolving power [9–12]. The first aberration corrected direct imaging transmission electron microscope was realized in 1997 by Haider et al. using a double-hexapole corrector [13,14]. Compared to the uncorrected basic instrument, a Philips CM200, this immediately showed twice the resolution. The first aberration-corrected scanning transmission electron microscope whose resolving power exceeded that of the uncorrected basic instrument was realized by Krivanek et al. in 2001, using a quadrupole-octupole corrector [15]. These inventions set electron microscopy on a completely new track, and they were the starting point of steady advancements both in the field of electron optics and in applications, which continue to this day.

Aberration-corrected transmission electron microscopy offers a great variety of powerful research opportunities. Of these a prominent field is that of investigations in *atomic dimensions*. This applies to both *conventional transmission electron microscopy* (CTEM) and to *scanning transmission electron microscopy* (STEM)[1]. Aberration-corrected transmission electron microscopes operating at electron energies of typically 200 to 300 keV today offer a Rayleigh resolution of about 50 picometers and a precision in the order of 1 picometer. This forms the basis for imaging and measuring atoms with previously unknown high precision. This review article deals with this in the case of CTEM. Its aim is to describe the recent progress by the introduction of aberration-corrected electron optics from classical electron microscopy to atomic-resolution electron microscopy. In doing so, we focus on the following aspects in particular: (1) The results of atomic resolution electron microscopy are now widely used in materials science. It therefore seems appropriate to describe, also for non-specialists, how these results were obtained, what is behind this technique and what the images produced with it really show. (2) Quantitative measurements in atomic dimensions are very involved and very different from classical electron microscopic techniques. As a result, scientists working with other electron microscopy applications, including those working predominantly with STEM, may have difficulty accessing quantitative CTEM. (3) Since this field is still very young, there is a lack of appropriate monographs. Details, both regarding theory and experimental practice, can therefore only be found in the mostly very technical literature, which is not always so easily accessible for those interested in a first introduction. (4) There are now quite a number of studies that have been done employing quantitative aberration-corrected CTEM. They demonstrate the potential applications for working in materials science at atomic scales. Facilitating access to the relevant application-related literature is therefore another goal of this article.

In the two and a half decades that have passed since the construction of the world's first aberration-corrected transmission electron microscope, atomically resolved images in the context of solving materials science problems have become an everyday phenomenon. Therefore, right at the beginning, we would like to recall that the atomic world is the world of quantum physics. Regardless of whether we perform CTEM or STEM, microscopy in atomic dimensions is therefore nothing else than applied quantum physics. It is thus subject to the restriction that the images are *a priori* not accessible to an intuitive interpretation. This may seem grotesque at times, especially when the images in publications correspond to certain presumptions and seem to resemble a projection of an atomic "ball-and-stick model". In fact, in reality and in contrast to simple light-optical microscopy, there are no conditions which - independent of the sample itself - would only have to be set in order to be able to "see" the structure of the object of interest directly. *The iterative fitting of a computed intensity distribution to that measured experimentally in the image is the fundamental process of the actual understanding of an electron microscopic image in atomic dimensions.* Only on this basis can such elementary questions be answered as to how and under what conditions, the atoms actually appear light on a dark background or, conversely, dark on a light background, and what information can be obtained from the fact that one atomic position appears brighter or darker than another. And, of course, one of the first questions is whether the atomic contrast appears at all at the position in the image where it is expected according to a structural model. If the intensity maximum that belongs to an atomic site appears shifted in the image compared to that of another site, then it must be clarified

[1] In the literature, the acronyms CTEM and STEM are used for both the instruments and the mode of operation of these. To avoid confusion, they are used here throughout to refer exclusively to the mode of electron microscope operation.

whether this observation is an imaging artifact or an interesting physical reality.

The contents of this article is organized as follows. We begin, in Section 2, with a brief outline of previous attempts to image structures in the electron microscope with atomic resolution using uncorrected optics. This section also serves to introduce important terminology that will be used on an ongoing basis in the following. In Section 3 we discuss briefly the basics of multipole lens systems to correct the optical aberrations of the objective lens of electron microscopes used for CTEM. In Sections 4 and 5 the principles of atomic-resolution imaging in aberration-corrected CTEM will be dealt with. Practical examples will be treated in Section 6. These examples are chosen such that each one of them describes one or more specific aspects of working under special high-resolution and high-precision conditions. In order to broaden the overview of typical applications of aberration-corrected CTEM, this section also contains short presentations of other and especially recent work. In Section 7 experiments performed in the aberration-corrected electron microscope *in situ* under direct observation at atomic resolution are treated. In Section 8 we discuss element-specific energy-filtered transmission electron microscopy (EFTEM) in an instrument corrected for spherical and chromatic aberration equipped with an imaging electron spectrometer.

In the following, occasional reference is made to the classical textbooks (written before aberration correction was available), Reimer and Kohl [16], Williams and Carter [17], and Spence [18] where the reader can find further information on the general principles of electron microscopy. A detailed introduction to aberration-corrected electron optics is given by Rose [19] and Erni [20]. For early reviews on the application of aberration-corrected CTEM in materials science we refer to Refs. [21–25]. For reasons of space and because of the fact that this has developed into a separate field, electron microscopy at low electron energies (15 to 80 keV) is not dealt with in this review. References [26–29] can serve as a guide to the respective literature. Since microscopy of graphene is particularly related to aberration-corrected microscopy at electron energies below 80 keV [e.g. 30,31], we would like to cite here also the review paper Ref. [32].

2. Historical and definitions with respect to atomic resolution

Most of the earlier high-resolution work carried out in non-corrected electron microscopes, in spite of the fact that the images looked like atomic, was in reality not truly atomically resolving. This will be briefly discussed here, because the comparison of images taken in aberration-corrected electron microscopes with images taken earlier in uncorrected instruments has repeatedly caused confusion. Before doing so, however, let us define more precisely what we mean today by atomic resolution of an electron microscopic image. In fact, this term has been defined very differently over the decades according to the corresponding state of the art in electron microscopy.

Most problems of applying CTEM to condensed matter involve crystalline samples. In general these are oriented for microscopy in such a way that the incident electron beam is parallel to a Laue orientation, i.e. a low-indexed direction of the crystal lattice, which is parallel to the z-axis in a corresponding Cartesian coordinate system. Since in this way the crystal atoms, in the projection, come to lie on top of each other, one "sees" atomic columns from above (end on), so that in general, due to the sequential scattering of the electrons, an atomic light or dark contrast stands for a whole column of atoms. Although, on the basis of quantitative measurement of local intensity and quantitative image calculation CTEM today allows measurements on the *vertical* arrangement of atoms in a given atomic column with atomic resolution (see below), the term *atomic resolution* is primarily understood as *lateral* resolution. It is constitutive for genuine atomic resolution that the position in the x-y-plane and the intensity of an atomic contrast in the image is determined *only* by the corresponding atomic column in the object, and that neighboring columns have no influence whatsoever on it. We will see in the following that this condition of "locality" of intensity and contrast is an extremely critical condition which is generally not fulfilled in images taken with uncorrected optics. In such a case, for example, measurements of the intensity at a given atomic position in the image are corrupted since they are influenced (as a result of aberration-induced "crosstalk") by the atoms in neighboring positions in the object. In this case, the contrast is termed "delocalized" and the intensity distribution in the image does not allow without further ado to conclude on the arrangement or the chemical nature of atoms in the object.

Before the advent of aberration-corrected electron optics, in the study of crystalline samples the so-called "lattice-fringe technique" was frequently employed [16–18]. For this an aperture is inserted in the back focal plane of the objective lens, the diameter of which is selected so large that several diffracted beams, characterized by a reciprocal lattice vector $\boldsymbol{g}$, contribute to the formation of the image simultaneously. The resulting image consists of a superposition of electron wave interference fringes perpendicular to the connection vector $\boldsymbol{g}_j - \boldsymbol{g}_i$ of pairs of interfering beams i and j. Due to the angular dependence of spherical aberration, the rays contributing to the image are subject to different phase shifts, which inevitably leads to artifacts. Thus, this method does not even fulfill the minimum requirements of an image formation. Neither the position of a given interference line, nor the distances between the lines, nor the local intensity of the resulting intensity maxima and minima are directly related to the atomic lattice. At best, one can extract crystallographic information from these images, for example certain symmetry properties. These are *non-local* properties of the whole collective of atoms but not of individual atoms. Further artefacts, which are not easily recognizable as such in the images, are discussed in Refs. [17,22].

The common reference for high-resolution CTEM in the pre-aberration-correction era was Scherzer's phase-contrast theory of 1949 [33]. This theory follows the principles of Zernike's phase-contrast theory in light microscopy. In the latter, the phase shift in which the information about the object is encoded is converted into visible amplitude information by advancing the phase of the diffracted beams by means of the $\lambda/4$ phase plate (λ-electron wave length) acting only on the diffracted beams and thus bringing them into counterphase to the transmitted beam [34,35]. As a result, in brightfield, the scattering areas appear dark against a bright background. Corresponding physical phase plates are difficult to realize in electron microscopy since the wavelength is shorter by more than 5 orders of

magnitude [36–40]. For this reason, the phase shift between the transmitted beam and the diffracted beams is realized in the Scherzer method exploiting the phase-shifting effect of the objective-lens' spherical and defocus aberration. This defines the dilemma of high-resolution electron microscopy that, on the one hand, aberrations must be reduced because they lead to a degradation of the image quality, but that, on the other hand, these aberrations are needed to convert the phase contrast of the atoms into amplitude contrast. The consequence is that an optimized setting must be sought with regard to both requirements. Formulated at a time where, at a fixed value of the objective-lens spherical aberration parameter, the only variable to optimize contrast was the objective-lens focal length, Scherzer's theory provides as a result a value for the lens defocus[2] yielding optimum contrast up to a certain spatial frequency g_S (the inverse of this frequency is termed Scherzer resolution). Unfortunately the Scherzer focus setting leads to a rather high value of contrast delocalization, higher than the value of the Scherzer resolution itself [41–43]. Because of the violation of the "locality" condition, images of crystal lattices taken under Scherzer conditions in non-corrected microscopes, however good they may look, are generally not atomically resolved in reality. Neither the intensity nor the location of a contrast maximum can be easily traced unambiguously to an atom or atomic column in the object because of the overlap of the contrast with that of neighboring atoms. This drastically limits the usefulness of images taken under Scherzer conditions[3].

For modern CTEM employing aberration-corrected optics Scherzer's theory is to be replaced by Lentzen's phase contrast theory [42,43]. Here the electron microscope is operated as an instrument with variable aberration. This means that one can also use the other rotationally symmetric aberrations besides the defocus aberration, i.e. the spherical aberration of third and also (if there is a setting option for this) fifth order, as variables suited to optimize contrast not only for optimum resolution but also (simultaneously) for minimum contrast delocalization. Both Scherzer's theory and Lentzen's theory are theories assuming ideally weak objects. They permit an understanding, to a first approximation, of the origin of electron microscopic contrast and how it can be optimized by adjusting the microscope parameters accordingly. In materials science, however, in reality most objects are strong scatterers. As a consequence, as the electron wave propagates in the sample, the phase shift between the incident beam and the diffracted beams takes on large ($\gg\pi/2$) and rapidly increasing values with increasing sample depth or thickness. The basic requirement for Zernike contrast theory is thus no longer fulfilled. The additional phase shift necessary to optimize the contrast thus becomes thickness-dependent (see also the second paragraph in Section 4.4). Furthermore, the assumption of a pure phase object is no longer valid. In addition to phase contrast, amplitude contrast always occurs in real material science objects, which, as we will see below, can be (with respect to phase contrast) of the opposite sign depending on the selected imaging parameters. We point out already here that this amplitude contrast has nothing to do with electron absorption, but is a consequence of the scattering of the electron wave in the interatomic potential. Thus an accurate theoretical description requires the dynamic theory of electron diffraction since also multiple scattering cannot be neglected. We emphasize once again that while the simplified schemes have their advantages for the purpose of initial qualitative orientation, working under real and trustworthy atomic resolution conditions (*"you always obtain an image, the question is whether you can trust it"*) requires recalculating the entire quantum physical scattering problem using quantitative image simulation on the computer.

To illustrate what has just been said and, at the same time, to demonstrate at the very beginning of this article the progress that aberration correction has brought to electron microscopy in materials science, we show in Fig. 1 computer-based image simulations that allow a comparison between an image taken with an uncorrected microscope (under Scherzer conditions) and an image of the same structure taken under optimal conditions with an aberration-corrected instrument. (a) shows schematically the atomic arrangement of strontium titanate, $SrTiO_3$, projected along the crystallographic [011] direction. We treat here the hypothetical but impressive case of an object containing three nanoholes in the form of a completely missing strontium-oxygen, a missing titanium, and a missing oxygen atom column (arrows). The corresponding diffraction pattern in the back-focal plane of the objective lens is shown in (b). Two aperture diaphragms are indicated[4]. The radius of the smaller one (dashed line) corresponds to $\boldsymbol{g}_S$, the maximum spatial frequency under Scherzer conditions in the uncorrected microscope. The radius of the larger aperture (full line) corresponds to $\boldsymbol{g}_I$, the spatial frequency at the information limit of the corrected instrument. It is evident that in the non-corrected case (c) the atomic structure is not resolved, and due to delocalization and a too low resolution the nanoholes cannot be recognized as such. For comparison, (d) shows an image taken in an aberration-corrected microscope. The agreement with the real structure (including the three nanoholes) is obvious.

3. Aberration correctors

A detailed account of the function of the various types of aberration correctors is beyond the scope of this review. The following

[2] In the following, as is usual in electron microscopy, the setting of the objective lens is characterized by means of the defocus. It denotes the deviation of the real focal length of the lens from the value under ideal Gaussian imaging conditions.

[3] Unfortunately this fact is generally not mentioned in the literature on the Scherzer setting. This may be one of the reasons why the very limited informative value of Scherzer imaging is hardly known. Moreover, this imaging mode is sometimes referred to as "under point resolution conditions", incorrectly implying that imaging under Scherzer conditions would be largely free of aberration-induced errors.

[4] The focal plane of the objective lens is the plane in which the diffraction pattern is formed. By placing an appropriate aperture stop there, it is possible to select the range of spatial frequencies that contribute to the formation of the image. Contributing is the range of spatial frequencies that lies inside the aperture, the range of frequencies that lies outside, at larger diffraction angles, is blocked.

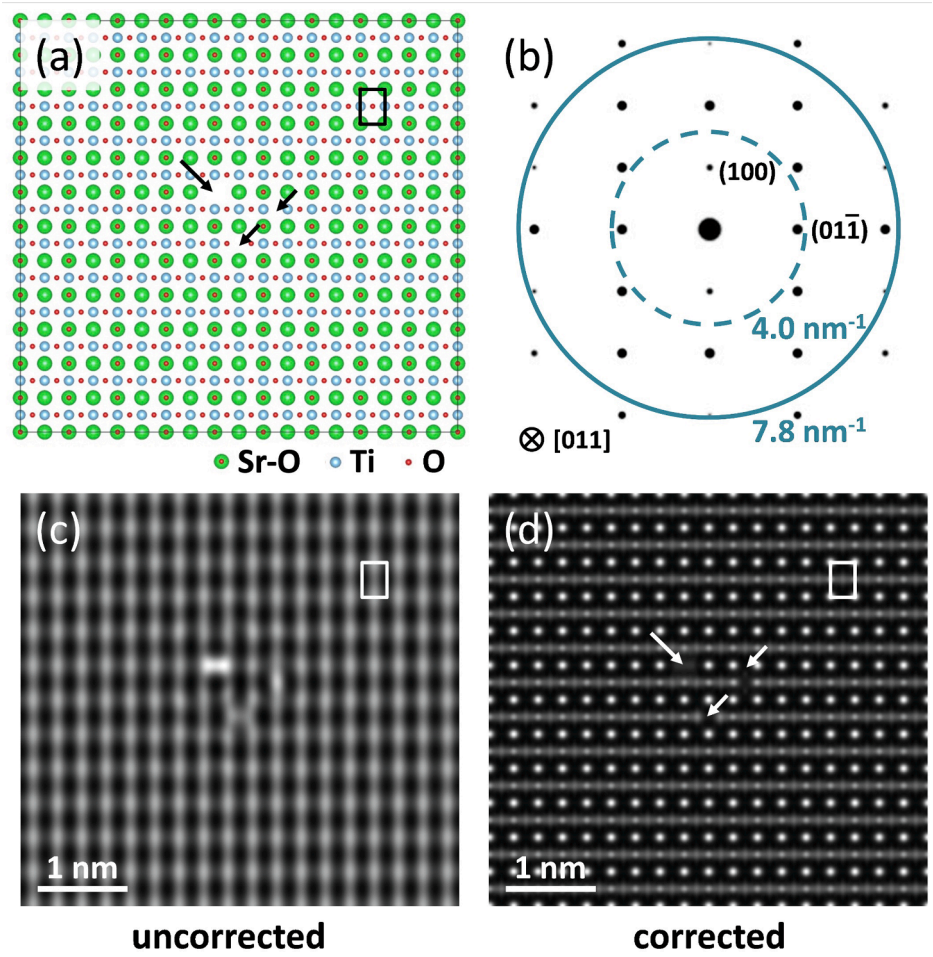

Fig. 1. Comparison of an image taken in an aberration-corrected electron microscope with an image taken in an uncorrected electron microscope. Computer-simulated images of a $SrTiO_3$ crystal acquired with the viewing direction parallel to the crystallographic [011] zone axis. (a) Schematic of the projected atomic structure; the SrO, Ti, and O atomic columns are indicated (along the viewing direction Sr-atom positions and O- atom positions are overlapping). The upright rectangle marks the position of 4 projected SrO atomic columns. Note that (to show an extreme case for demonstration) an entire SrO, an entire Ti, and an entire O atom column is missing in the center ("nano-holes"; arrows). (b) Diffraction pattern in the back focal plane of the objective lens. Two aperture diaphragms, centered with respect to the zero-order (transmitted) beam are indicated. The radius (4.0 nm^{-1}) of the smaller one (dashed line) corresponds to $\boldsymbol{g}_S$, the maximum spatial frequency under Scherzer conditions in the uncorrected microscope. The radius of the larger aperture (7.8 nm^{-1}; full line) corresponds to $\boldsymbol{g}_I$, the spatial frequency at the information limit of the corrected instrument. (c) Image in the uncorrected instrument under Scherzer conditions; atom positions appear dark on a bright background. (d) Image in the corrected instrument: Negative spherical aberration imaging (NCSI) conditions applied; atom positions appear bright on a dark background. It is obvious that in (c) the atomic structure is not resolved, and due to delocalization and insufficient resolution, although the contrast is locally changed, the nanoholes cannot be recognized as such. On the other hand, (d) shows full atomic resolution; all types of atoms are visible and the nanoholes are perfectly imaged. Calculations for an electron energy of 200 keV, C_S=+1.23 mm; Z = -68 nm for (c) and C_S = -41 μm; Z=+11 nm for (d). Sample thickness: 2.76 nm.

brief introductory remarks must suffice here, and we will limit ourselves to correctors for CTEM employed in the instruments with which the materials science results discussed here were achieved. For further technical details, we refer to the literature [19,20,44,45].

We start with correctors based on hexapole lenses that correct geometrical aberrations [46][5]. At quite an early stage, hexapoles were treated theoretically with respect to their possible use in spherical-aberration correction systems. Hawkes, in 1965 [47,48] , was the first to point out that in a second approximation extended hexapoles exhibit (in addition to other aberrations) third-order aberrations equivalent to those of round lenses, and it could be shown that this spherical aberration can have a negative sign [49,50]. In 1979, Beck proposed the use of hexapole fields to compensate the spherical aberration of an electron microscope objective lens for

[5] Geometrical aberrations lead to distortions of the image intensity distribution. However there is no loss of information. This allows to recover the original object structure by computer-based processing if the values of the aberration parameters are known. In contrast chromatic aberration is an incoherent aberration reducing the image contrast in an irreversible way.

STEM [51]. In contrast to the case of STEM where only the axial aberrations of the probe-forming lens have to be compensated a corrector for the objective lens in CTEM has to be able to compensate also off-axial aberrations over the whole extension of the field of view employed in imaging. The corresponding electron optical problems were solved by Rose who suggested and computed theoretically a corrector system for CTEM based on two hexapoles in 1990 [44]. This system was technically realized by Haider et al. [13,14,52] between 1991 and 1997. Rose's corrector, since the case of CTEM is the more comprehensive one, automatically and without further ado corrects (with inverted ray path) the spherical aberration also in STEM [20,53][6].

Fig. 2 schematically shows the set up and the ray path of the corrected objective lens system as it was used in the world's first aberration-corrected transmission electron microscope [13,14]. It consists of a Riecke-Ruska condenser-objective lens [16,54], two hexapole lenses and two transfer telescopic round-lens doublets. This system allows to compensate the third-order spherical aberration of the objective lens, characterized by the spherical-aberration coefficient C_3 (in the following also denoted by C_S) to zero or to set specific (positive or negative) values of some tens of micrometers in order to optimize the contrast (see below). The fifth-order spherical aberration parameter C_5 is very small (<10 mm) and in the design of [13,14] it was not intended to reduce this value further. The corrected objective lens is termed a *semi-aplanat* since the corrector compensates for the third-order radial (isotropic) part of the off-axial coma but only partly for the anisotropic azimuthal coma [19,44,45]. This corrector design is also the basis of the commercial CEOS CETCOR spherical-aberration-corrected objective lens [55,56]. An improved version is the CEOS B-COR based on a hexapole triplet. It also includes correction of azimuthal off-axial coma and fifth-order spherical aberration [56].

For chromatic aberration correction in addition to spherical aberration correction multipole magnetic elements are not sufficient but additional electrostatic quadrupoles are indispensable [57]. Fig. 3 shows schematically the ray path of the quadrupole-octupole CEOS C-COR corrector developed within the TEAM project at Lawrence Berkeley National Laboratory [58–60]. It also corrects, besides spherical aberration, axial chromatic aberration (characterized by the parameter C_C). To allow for a particularly large field of view, the lens system also corrects for the off-axial coma. This makes the imaging achromatic and aplanatic. The corrected system is therefore termed an *achroplanat*. It contains two multipole modules and six magnetic transfer lenses. Each of the two multipole modules (quintuplets) comprises four magnetic quadrupoles/octupoles and one electrostatic-magnetic (Wien-filter like) element. It has been found that the spatial resolution of this corrector and thus of the TEAM instrument is limited by an incoherent image spread attributed to Johnson noise (see below) [61,62]. For this reason, for the Jülich spherically and chromatically corrected PICO (FEI Titan G3 50-300) instrument a with respect to Johnson noise optimized version, the CEOS C-COR+ corrector, was designed and implemented [63].

The adjustment of the aberration corrector is part of the adjustment procedure of the microscope. The basis is an analysis of the Zemlin tableau [13,14,20,52,64] , which allows the axial and off-axis aberrations of the objective lens system to be measured. For this purpose, diffractograms of an amorphous object, which is assumed to scatter electrons with a more or less uniform distribution over a sufficiently large range of angles, are generated under defined tilt angle (the polar angle in a spherical coordinate system) of the illumination as a function of the azimuthal angle. The automatic evaluation procedure is coupled to the alignment. It measures and adjusts the coefficients C_1 (defocus, later also denoted by Z), C_3, A_1 (twofold astigmatism), A_2 (threefold astigmatism), B_2 (second-order axial coma), A_3 (fourfold astigmatism), S_3 (third-order star aberration), A_4 (fivefold astigmatism)[7]. If applicable (C-COR +), also C_5 can be adjusted. When changing from the amorphous sample to the sample to be investigated, it must be ensured that the settings do not change (e.g. due to a change in the vertical sample position). The temporal stability of the set values of the aberration coefficients was examined in [65,66] by means of a new ultra-precise method for the evaluation of diffractograms. The result, for the type of instruments studied and for the state of the art at that time, was that the duration of the stability phase of C_1 and A_1 is in the order of minutes, that of B_2 and A_2 of hours, and that of C_3, A_3 and S_3 of days. In any case, it is advisable to additionally treat the values of the aberration coefficients valid at the time of image acquisition as fit parameters within the quantum-physical and optical image simulation and thus to confirm or correct them *ex post*.

4. The principles of atomic resolution imaging

4.1. Resolution and point spread

Since we lack the space here for a systematic sequential treatment of the electron passage through the object and the change of the electron wave field by the electron optics, in the following we will use the results of a complete dynamic treatment of electron scattering in the computer and the classical simplified treatment, which is more favorable for a qualitative understanding, side by side. For the following it is of great importance that we today have powerful curated software packages at our disposal that make it possible to implement this modern electron microscopy, in which experimental observation is carried out "in tandem" with image interpretation mediated by computer simulation [67–74].

The original goal of atomic-resolution work is to measure the set of individual atom positions in a sample. However, quantitative CTEM allows also to measure the chemical composition. In the simulation performed on the computer the nature of the scattering atoms enters into the calculation of the atomic scattering potential. In addition, in the case of a mixed occupation of the atomic columns, the local concentration of the different types of atoms enters as a variable. Due to the fact that electron scattering and contrast

[6] In fact, more than 95% of all instruments used in today's CTEM and STEM employ a Rose type double-hexapole corrector or use a corrector design derived from it.

[7] With regard to the designation of the aberration coefficients we refer to [52,56].

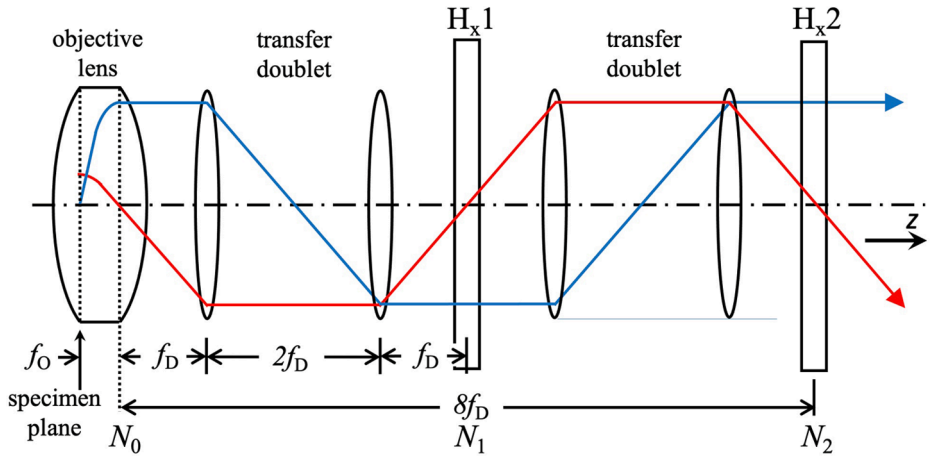

Fig. 2. Schematic of the semi-aplanatic objective lens system of the first aberration-corrected transmission electron microscope [13,14]. It consists of the original objective (immersion) lens of the uncorrected instrument (focal length f_O), of two hexapoles H_x1 and H_x2 as well as two telescopic round-lens transfer doublets. Axial ray: blue. Off-axial field ray: red (for the ray definition cf. [20]). N_0, N_1, and N_2 denote the position of the outer nodal planes of the transfer doublets of focal length f_D. The *primary* aberration of a hexapole distorts a cylindrical bundle of parallel rays into a bundle with triangular shape. Imaging the first hexapole into the second hexapole of inverted polarity with unit magnification by centering the hexapoles at N_1 and N_2, respectively, allows to eliminate this primary aberration. "Long" hexapoles also exhibit a *secondary* aberration. This is rotationally symmetric and proportional to the square of the hexapole strength and thus independent of the hexapole polarity. The sign of the appertaining coefficient of spherical aberration is opposite to that of the objective lens. Accordingly, the spherical aberration of the entire system can be eliminated by exciting the hexapoles appropriately. (By permission of CEOS GmbH).

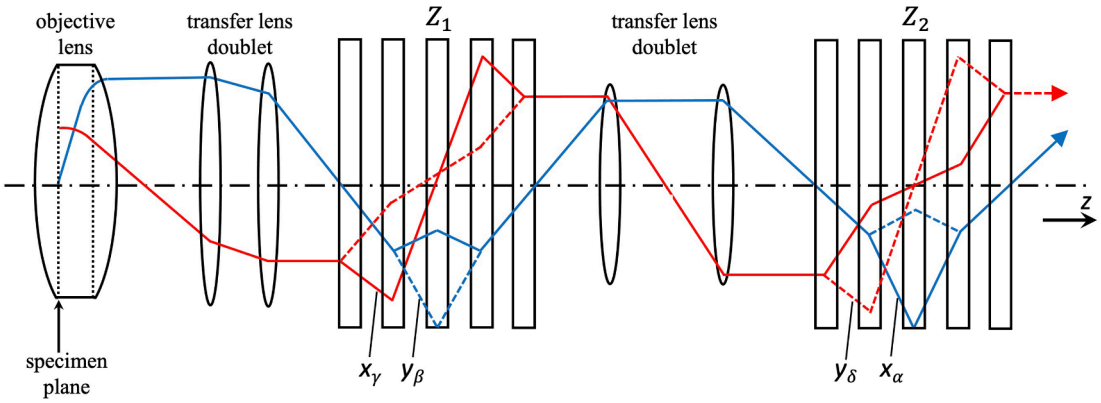

Fig. 3. Ray path of the lens system developed within the TEAM project. It is corrected for both spherical and chromatic aberration and also for off-axial coma. It consists of two multipole modules and six magnetic transfer lenses (the transfer-lens doublet between the corrector and the selected area plane is not shown). Each of the two multipole modules (quintuplets) comprises four magnetic multipoles and one principal electrostatic-magnetic (Wien-filter like) correction element. The four magnetic multipole elements generate the quadrupole fields and additional weak multipole fields with even and odd symmetry for alignment. Z_1 and Z_2 denote the centers of the multipole elements. Axial ray: blue; field ray: red. Dashed lines refer to the fact that, for visualization in this scheme, the electron trajectories in the *x*-*z*-plane and in the *y*-*z*-plane were projected together into one plane. (By permission of CEOS GmbH).

are generally sensitively dependent on local stoichiometry, this can be measured at atomic resolution as part of the computer fit. Further access to the chemical composition of the sample employing EELS spectroscopy is provided by EFTEM as described in Section 8.

We are treating here the case of a crystalline sample. We employ an electron wave field represented for simplicity by a single plane wave (amplitude normalized to 1)

$$\psi_0(\boldsymbol{r}) = \exp(2\pi i \boldsymbol{k}_0 \cdot \boldsymbol{r}) \tag{1}$$

incident on the upper sample surface. Here $\boldsymbol{k}_0$ denotes the wave vector whose modulus is the inverse of the electron wave length λ. $\boldsymbol{r}$ denotes the general position vector. On its way through the specimen this wave field interacts with the atomic scattering potential $V(\boldsymbol{r})$. At electron energies of typically 200 to 300 keV the wave function of the relativistic electrons $\psi(\boldsymbol{r})$ in the crystal is given as a solution of

the Dirac equation subject to the boundary conditions at the surface. Neglecting spin polarization, and in an approximation for weak scattering potentials, the equation adopts a Schrödinger-type form with relativistically corrected mass and wavelength [16–18,75].

The wave function in the plane of the lower specimen surface, the exit-plane wave function ψ_e, contains all the information on the specimen that the electrons can supply us with. In the general case this information is not directly accessible but encoded in a complicated way determined by the quantum physical interaction inside the specimen. After leaving the specimen, in the potential-free space, the exit-plane wave field can be described as a superposition of plane waves. Written as a Fourier integral we thus obtain

$$\psi_e(\boldsymbol{r}) = \int \psi(\boldsymbol{g})\exp(2\pi i\boldsymbol{g}\cdot\boldsymbol{r})d\boldsymbol{g} \tag{2}$$

with the modulus of the reciprocal vector $\boldsymbol{g}$ representing the spatial frequency. It is this wave field (and strictly speaking not the sample itself) which is then the *object* of the objective lens of the microscope. The intensity distribution in the image plane is given by the vector of the electron current density which, in a small-angle approximation, is proportional to the electron probability density, i.e. the absolute square of the wave function,

$$I(\boldsymbol{r}) \propto \frac{ih}{4\pi m}(\psi\nabla\psi^* - \psi^*\nabla\psi) \propto |\psi|^2 \tag{3}$$

where h is Planck's constant and m is the relativistically corrected electron mass[8].

If the lens has optical aberrations, these have the effect that the individual components $\psi(\boldsymbol{g})$ of the exit-plane wave function are multiplied by the phase factor

$$\exp[-2\pi i\chi(\boldsymbol{g})] \tag{4}$$

where

$$\chi(\boldsymbol{g}) = \frac{1}{2}Z\lambda\boldsymbol{g}^2 + \frac{1}{4}C_S\lambda^3\boldsymbol{g}^4 + \frac{1}{6}C_5\lambda^5\boldsymbol{g}^6 + \cdots \tag{5}$$

is the wave-aberration function (expressions comprising also higher-order terms can be found in [52,76,77]). The first term is the lens defocus aberration with Z denoting the defocus parameter[9]. The second term is due to third-order spherical aberration, where C_S denotes the spherical aberration parameter[10].

The presence of aberrations has the consequence that a point in the object plane is not imaged into a sharp corresponding point in the image plane but rather into an error or point-spread disk whose radius is given by the point spread function which also characterizes contrast delocalization

$$R = \max\left|\frac{\partial\chi}{\partial g}\right| = \max\left|Z\lambda g + C_S\lambda^3 g^3 + \cdots\right|; 0 \le g \le g_{max} \tag{6}$$

where the maximum has to be taken over the whole range of spatial frequencies (up to g_{max}) contributing to the image [41,42]. In the fully aberration-corrected case, $C_S = 0$ and $Z = 0$, point spread becomes zero. Any finite values of Z and of C_S (e.g. applied when taking focal series as described below or for optimizing contrast) will lead to finite values of R. However, as shown below, the values of R can be kept sufficiently small not to affect most practical high-resolution work in the aberration-corrected electron microscope.

4.2. Contrast

As emphasized above, in order to fully exploit the wealth of quantitative information that modern aberration-corrected transmission electron microscopy is able to provide, the problem of contrast should be discussed on the basis of a numerical treatment. That

[8] Example: At an electron energy of 300 keV: $\lambda = 1.97$ pm; $m = 1.59\,m_0$ (m_0 - rest mass of the electron).

[9] Unfortunately, there are two systems of choosing the sign of Z in the literature. This is unproblematic as long as one stays within the same system. Otherwise, especially since the conflict is normally not addressed in the literature (an exception is [17]), this can be confusing. Both systems agree that, if the object and image planes (of the Gaussian case) are held fixed, a weakening of the magnetic excitation of the lens, i.e. an extension of the focal length, is called "underfocusing". In case of stronger excitation of the lens, i.e. a shortening of the focal length, this is called "overfocusing". Scherzer in his fundamental work of 1949 [33] fixed the sign of Z in such a way that it appears in the expression for the wave aberration with reversed sign with reference to C_S . This prevents that in the expression for the Scherzer focus, which describes underfocusing, one has to put a minus in front of the numerical specification for Z. This definition was also adopted by Reimer in his textbook [16]. In contrast, the more recent literature consistently defines Z and C_S with the same sign. This sign convention is also followed in the present work. Example: As the focal length is increased, the image plane moves away from the lens, and a fixed image plane appears to move toward the lens. This is described by a negative sign of Z.

[10] Different systems can be found in the literature to denote aberration coefficients. Furthermore the "ray" and the "wave" picture are used side by side. The ray aberration is proportional to the derivative of the wave aberration with respect to g. For example, $C_3 = C_S$ in Eq. (5) (in the wave aberration system) occurs there in an expression containing g^4 but is nevertheless termed "third-order" spherical aberration, employing the ray-aberration system in which g occurs as to the third power. On the other hand, the radius of the point spread function R is formulated within the ray aberration system. For details we refer to Refs. [20,52,76].

in the following we nevertheless start with the classical approach to treat the simplified cases of weak phase and weak amplitude objects serves a schematic understanding of contrast formation. On the other hand such a discussion will also allow us to point out the limitations of such treatments.

We start the discussion with phase contrast. This means, that access to the specimen structure is obtained exploiting the information contained in the locally varying phase of the exit-plane wave field. As in light microscopy under Zernike phase contrast conditions [34,35] the problem arises that the atomic phase contrast has to be converted into amplitude contrast. While in light microscopy the phase shifts are small the phase shifts in electron microscopy, depending on atomic number and specimen thickness, can be quite large. Nevertheless, for the sake of illustration, we assume for the moment that the phase change is small, i.e. we apply the weak phase object (WPO) approximation [16].

For this the exit-plane wave function is written as a plane wave related to the incident wave ψ_0

$$\psi_e(\boldsymbol{r}) = \psi_0 \exp[i\varphi(\boldsymbol{r})] \approx \psi_0 \left[1 + i\varphi(\boldsymbol{r}) - \frac{1}{2}\varphi^2(\boldsymbol{r}) + \cdots\right] \tag{7}$$

If the specimen-induced phase change is small, terms beyond the linear one in the Taylor series expansion can be neglected.

Schematically the conditions can be illustrated in the Gaussian complex number plane. The incident wave is characterized by a vector along the real axis. The diffracted wave is represented by a short vector along the imaginary axis taking account of the fact that the basic physical phase shift of a diffracted wave is $\pi/2$ with respect to the incident wave [46]. The sum of both is a vector rotated in mathematically positive direction by a small angle but of essentially the same amplitude as that of the incident wave. In light microscopy an additional $\pi/2$ phase shift is imposed on the scattered wave by the insertion of the $\lambda/4$ phase plate bringing the scattered wave into antiphase to the incident wave. Now, summing up yields a shorter resulting vector and a corresponding intensity reduction. As a result the scattering regions give dark contrast on a bright background. This is called *positive* phase contrast [16–18,43].

Phase contrast is governed by the phase-contrast transfer function (PCTF) $\sin 2\pi\chi(\boldsymbol{g})$ [16–18]. Ideally, for perfect imaging, the modulus of this function should take the value 1 for the entire range of spatial frequencies transmitted by the microscope optics into the image plane. The PCTF in the case of Scherzer imaging in an uncorrected instrument, for which, for a fixed value of the spherical aberration parameter, the value of the objective lens focus was optimized, is shown in Fig. 4a[11]. How this optimization is done depends on the preferences. Scherzer in optimizing the defocus value, followed the strategy of making the plateau, with relatively high magnitudes of the transfer function, as wide as possible, while pushing the onset point g_S of the contrast oscillations to the highest possible values. In order to avoid a contribution of the contrast oscillations, which would complicate the interpretation of the image, a lens aperture diaphragm is then used, the radius of which is chosen in such a way that rays with $g > g_S$ are blocked. This means that beyond the Scherzer resolution g_S^{-1} information could still be transferred by the microscope, but it does not contribute to the formation of the image. The corresponding PCTF for an aberration-corrected instrument is displayed in Fig. 4b. It was derived by Lentzen et al. [42,43,76,77] taking advantage of the fact that now the defocus and additionally the third-order spherical aberration are available for the optimization of the aberration function. First of all the goal is to eliminate the contrast oscillations for $g_S \leq g \leq g_I$, where g_I denotes the spatial frequency marking the information limit determined by partial spatial and temporal coherence of the illumination system (see below) [78–80]. It is defined by the value of the spatial frequency where the amplitude of the transfer function drops to $1/e^2 = 0.135$. The second goal is to reduce point spread to a fraction of g_I^{-1}. Finally care has to be taken that the low-contrast, poor transfer region at low spatial frequencies is kept as narrow as possible. There is a trade-off in the sense that increasing g_I is widening the low-spatial-frequency gap. The optimum settings for *positive* phase contrast in an aberration-corrected instrument are then given by

$$Z_{opt} = -\frac{16}{9}\left(\lambda g_I^2\right)^{-1} \tag{8}$$

$$C_{S,opt} = +\frac{64}{27}\left(\lambda^3 g_I^4\right)^{-1} \tag{9}$$

$$R_{opt} = \frac{16}{27} g_I^{-1} \tag{10}$$

Values for $C_{S,opt}$, Z_{opt} and R_{opt} are given in Table 1a[12]. With typical values of 0.5 to 1.2 mm for C_S in an uncorrected instrument it is evident, that the residual values required for optimum contrast in the corrected instrument are only a few percent of the original values of the spherical aberration parameter. A corresponding treatment of *positive* phase contrast including variable fifth-order spherical aberration, C_5, is given in [77] (Table 1b):

[11] For this figure, as for the entire article it is assumed that the microscope has a field emission source (FEG). In aberration-corrected electron microscopy, field emission electron sources in the form of cold emitters or heated Schottky emitters are used throughout. Compared to the classical thermionic LaB_6 emitter, these sources are characterized by a higher coherence, a brightness that is orders of magnitude higher and by a very low energy spread of the electron beam. Additional energy filters in the beam-forming system are often used to further narrow the energy width. For a detailed discussion of electron sources we refer to [16,17].

[12] We point out that in Table 1, in order not to have to show this table twice, the values for NCSI are given (see Section 4.3), which, with the exception of R_{opt}, have opposite sign.

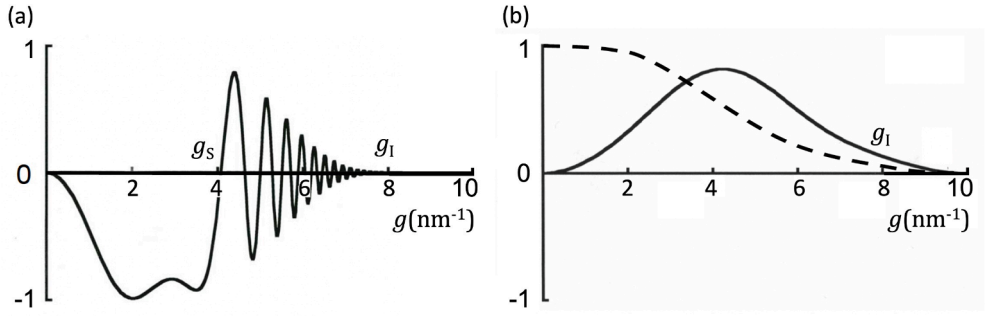

Fig. 4. The value of the phase contrast transfer function $\sin 2\pi\chi(g)$ as function of spatial frequency g at an electron energy of 200 keV assuming an information limit of 0.125 nm and a semi-convergence angle of the illumination of 0.2 mrad. $\chi(g)$ is the wave-aberration function (compare Eq. (5)). It is assumed that the electron source consists of a field emission gun (FEG). (a) Scherzer conditions (positive phase contrast) for a non-corrected microscope; spherical aberration parameter $C_S = 1.23$ mm. The inverse of g_S is the Scherzer resolution. g_I is the spatial frequency corresponding to the information limit. (b) Plot for Lentzen's settings, assuming NCSI conditions (full line; negative phase contrast) in an aberration-corrected instrument (see text). The region of optimized contrast expands up to the information limit. Note the bell shape of the curve. This shows that the information transfer of the microscope, from the object to the image, is far from the ideal case, which would require a uniform amplitude independent of the magnitude of the spatial frequency. The amplitude contrast transfer function $\cos 2\pi\chi(g)$ is also given schematically (dashed line). (Reproduced from [76] with permission from Cambridge University Press).

Table 1
Negative spherical-aberration imaging (NCSI). Typical optimum values for the spherical aberration parameter $C_{S,opt}$, the defocus parameter Z_{opt}, and the radius of the point spread function R_{opt}, calculated by means of Eqs. (8) to (14) for the electron energy E and the information-limit spatial frequency g_I. The sign of the coefficient of spherical aberration and of defocus is chosen for NCSI (i.e. the signs in Eqs. (8,9,11,12,13) are inverted; see text). (a) FEI Titan® 80-300, measured values for g_I of [78]; (b) FEI PICO with CEOS C-COR+; $C_{5,opt}$ is the optimum value of the fifth-order spherical aberration parameter.

(a) E (keV)	g_I^{-1} (nm)	$C_{S,opt}$ (μm)	Z_{opt} (nm)	R_{opt} (nm)
300	0.08	-12.7	5.8	0.05
200	0.11	-21.9	8.6	0.07
80	0.19	-42.3	15.4	0.11

(b) E (keV)	g_I^{-1} (nm)	$C_{5,opt}$ (mm)	$C_{S,opt}$ (μm)	Z_{opt} (nm)	R_{opt} (nm)
300	0.05	7.1	-12.5	4.8	0.03
200	0.05*)	2.1	-6.1	3.8	0.03
80	0.075	1.9	-6.7	5.1	0.04
50	0.09	1.6	-6.3	5.6	0.05

*) corresponding to the value measured in [63].

$$Z_{opt} = -15\left(4\lambda g_I^2\right)^{-1} \tag{11}$$

$$C_{S,opt} = +15\left(\lambda^3 g_I^4\right)^{-1} \tag{12}$$

$$C_{5,opt} = -105\left(8\lambda^5 g_I^6\right)^{-1} \tag{13}$$

$$R_{opt} = \frac{15}{8} g_I^{-1} \tag{14}$$

We point out that the PCTF for the aberration-corrected case (Fig. 4b) has a shape which is far from ideal. The transfer function displays no zeros or oscillations and the resolution of the microscope is substantially increased compared to the uncorrected instrument. Thus, the central goals of the design of aberration-corrected optics are fulfilled. However, the transfer is very sensitively dependent on spatial frequency. Recalling that microscopy is essentially a two-Fourier transform process, for optimum contrast transfer, the amplitude should be as close as possible to the value 1 independent of the spatial frequency. In reality, however, the microscope acts as a highly nonlinear filter. As a result, the images are generated on the basis of a wave field that is significantly altered by this special form of contrast transfer. A number of contrast artefacts have been reported in the literature which can be traced back to the particular shape of the PCTF [43,81]. Also it was found that the width of the low-spatial-frequency gap which has to be tolerated in order to maximize g_I is too wide to allow effects of chemical bonding-induced charge redistribution in nitrogen-doped graphene to be imaged [82]. This is extended over many atomic distances, and therefore an adequate description involves low spatial frequencies. Since there is no direct way to reconstruct information largely lost due to a particular shape of the contrast transfer function, for work

in which the emphasis is on long-range features higher defocus values (compared to those given in Eq. (8)) have to be applied. These increase the quadratic term in Eq. (5) that dominates the PCTF for small values of spatial frequency. This, of course, will have consequences for the other properties of the PCTF and for delocalization, and it may be advisable to take a sequence of images at different focus values (focal series; see below). All these cases indicate that imaging is incomplete without performing a numerical "backward" calculation from images to structure.

4.3. Enhanced contrast under negative spherical aberration imaging conditions

In 2001, Jia [83] observed for the first time in images taken in the aberration-corrected electron microscope extraordinarily high contrast in barium titanate ($BaTiO_3$) and strontium titanate ($SrTiO_3$) with atomic positions of cations and of oxygen appearing bright on a dark background for certain settings of the excitation of the microscope's aberration corrector. On the basis of detailed image simulations, he was able to show that the direct cause of this high bright contrast was an overcompensation of spherical aberration of the objective lens, i.e. imaging at negative spherical aberration, in combination with a lens overfocus. This mode of CTEM was termed negative spherical aberration imaging (NCSI). Fig. 5 shows one of those early experimental images of $SrTiO_3$ taken along the crystallographic [011] direction. All atom positions are visible bright on a dark background including oxygen. For comparison Fig. 6 shows simulated images for C_S values of (a) +40 μm, and (b) −40 μm for different defocus values (horizontal axis) and sample thicknesses (vertical axis) at an electron energy of 200 keV[13]. Clearly oxygen cannot be seen under positive spherical-aberration imaging (PCSI) conditions, independent of the defocus value chosen. This means that such a setting does not supply us with full atomic details in spite of the fact that the optical resolution (of 0.12 nm in this particular case) is sufficient to resolve the oxygen-titanium atom separation of 0.138 nm. On the other hand, under NCSI conditions the atom positions are imaged bright on a dark background, and oxygen can clearly be seen between the two neighboring titanium atom positions. In [84,85] the NCSI technique was employed to image oxygen in the oxide superconductor $YBa_2Cu_3O_7$ for the first time and to measure the oxygen concentration in crystal lattice defects. The direct observability of oxygen atoms in oxide materials using aberration-corrected electron microscopy and the fact that it was also possible to measure the local concentration of oxygen by quantitative contrast evaluation (see below) was immediately hailed as a major success of the new type of electron microscopy [86–93].[14]

How can this operation mode at negative spherical aberration be understood? Within the framework of the WPO approximation inverting the sign of $C_{S,opt}$ and Z_{opt} changes the contrast from "positive" to "negative" phase contrast but does not yield any contrast enhancement [42,43]. This can be seen immediately when looking at the Fig. 6a for the case of very small sample thicknesses for which the WPO approximation can be considered adequate. In order to arrive at an understanding of the contrast enhancement, certain obviously oversimplifying assumptions made in the theory of "weak" objects have to be abandoned: (1) Calculating the phase angles and amplitudes for different reflections for $SrTiO_3$ we find that for realistic sample thicknesses the phase shifts between the incident (transmitted) wave and the scattered waves are always large. This means that the WPO approximation is inadequate and only a fully dynamical treatment of the electron scattering and imaging problem can provide an adequate description. (2) Furthermore, we have to discuss *amplitude contrast* which so far was entirely neglected.

We start by taking a look at the consequences of taking in Eq. (7) the quadratic term into account in the Taylor series expansion for the case of "not so weak" objects. In order to estimate the change in phase contrast intensity predicted by an expansion of the WPO treatment to the case of a "not so weak" object we write [94] for the wave function in the object plane (with $\psi_0 = 1$)

$$\psi_c(\boldsymbol{r}) = 1 + \pi i \lambda U(\boldsymbol{r}) t \tag{15}$$

with

$$U(\boldsymbol{r}) = \frac{2me}{h^2}\bar{V}(\boldsymbol{r}) \tag{16}$$

where $\bar{V}(\boldsymbol{r})$ denotes the projected crystal potential, t is the specimen thickness and e the elementary charge . This is altered by the application of the $\pm\pi/2$ phase plate[15] to the diffracted wave. Thus we obtain for the wave function in the image plane

$$\psi_i(\boldsymbol{r}) = 1 \mp \pi \lambda U(\boldsymbol{r}) t \tag{17}$$

[13] All images were calculated (solving the fully dynamic scattering problem inside the sample) with the electron beam parallel to a {011} zone axis using the MacTempas software package [68,74].

[14] At least since the discovery of high-temperature superconductivity in 1986, the possibility of observing oxygen has been considered a challenging topic in electron microscopy. However, experimental and theoretical investigations showed that even with 400 keV microscopes at the then (1987) state of the art, the resolution and contrast were insufficient [88,89,90]. Only in a single case, where a high-voltage electron microscope with a Scherzer resolution of nominally 1.25 Å at 1 MeV was used (1991), was it possible to image oxygen in ZrO_2 [91]. However, it turned out that oxygen atoms could not be seen in $YBa_2Cu_3O_7$ under the same conditions. That access to oxygen is possible using the focus variation technique based on computer processing of a series of images at 400 keV was demonstrated in 1999 in the case of $BaTiO_3$ [92] and in 2001 of α-Al_2O_3 [93].

[15] We use here figuratively the expression "phase plate" from Zernike's theory, although we generate here the corresponding phase shift of the diffracted wave to the transmitted wave by means of the wave aberration function of the objective lens. Positive sign is valid for positive phase contrast and negative sign is valid for negative phase contrast.

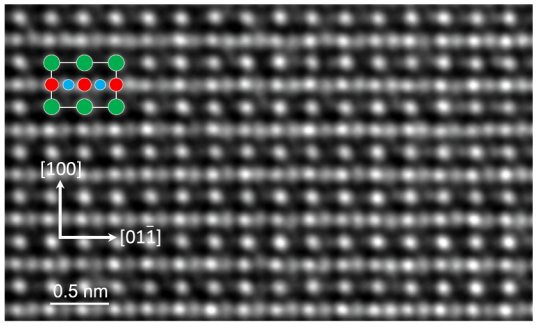

Fig. 5. Experimental image of a $SrTiO_3$ crystal along the [011] zone axis employing the NCSI technique. All three types of atomic sites are visible bright on a dark background. The inset schematically marks a unit cell: SrO: large green circles; Ti: medium size red circles; O: small blue circles. Philips CM200 with image corrector [13,14], operated at 200 keV; $C_S = -40$ µm, $Z = +8$ nm. (Reproduced from [84] with permission from the American Association for the Advancement of Science).

where the negative sign applies to positive phase contrast and the positive sign to negative phase contrast. The image intensity is the modulus squared of the wave function in the image plane (Eq. (3)). Maintaining terms up to second order we obtain

$$I(\boldsymbol{r}) = 1 \mp 2\pi\lambda U(\boldsymbol{r})t + [\pi\lambda U(\boldsymbol{r})t]^2 \tag{18}$$

The comparison of these two cases shows that for positive phase contrast the linear contribution and the quadratic contribution have *opposite sign*. As a consequence the local intensity modulation at an atom site becomes *weaker* upon increasing the strength of the object. On the other hand, the linear contribution and the quadratic contribution have *same sign* for negative phase contrast, and the local intensity modulation at an atom column site becomes *stronger*. In other words, setting up a negative value of residual spherical aberration combined with an overfocus enhances the atomic phase contrast compared to a setting with positive residual spherical aberration and underfocus. This contributes the first part of the contrast enhancement in NCSI. We note that for NCSI conditions the sign in the above equations Eqs. (8,9) and Eqs. (11,12,13) has to be inverted.

Now to amplitude contrast: If the exit-plane wave function has a locally varying amplitude structure consequentially amplitude contrast occurs. In the classical linear contrast treatments of weak objects (see e.g. [16]) only amplitude changes due to locally varying electron *absorption* are considered. This is not what we are dealing with here. Amplitude structure occurs for crystalline specimens as a result of (elastic) dynamical electron interaction with the periodic scattering potential inside the crystal. The result is an "oscillatory" motion of the electrons inside the crystal where the electrons, depending on the depth, are more or less localized on the atomic strings or in between. This phenomenon is called *electron diffraction channeling* [95]. In the linear theory, amplitude contrast is proportional to $\cos 2\pi\chi(\boldsymbol{g})$, the amplitude contrast transfer function (ACTF) [16] displayed schematically in Fig. 4b.

For more insight into amplitude contrast in crystalline specimens we neglect phase contrast for the moment, i.e. we carry out a contrast treatment for $C_S = 0$ and $Z = 0$. For defect-free ideal crystals we can perform a Bloch-wave calculation. This approach is taken in the classical treatment of electron diffraction channeling [16,95–97]. The oscillatory motion of the electrons as a result of electron diffraction channeling is schematically depicted in Fig. 7 for three different sample thicknesses. This can be understood as follows. At the specimen entrance surface the electrons are spatially uniformly distributed. While the wave field penetrates into the specimen the positively charged atom strings interact with the electrons attractively concentrating the electrons after some distance from the entrance surface on the atom positions. Subsequently the electrons fan out again yielding an electron current density distribution after a certain distance which (neglecting inelastic scattering) is similar to that at the surface.

In the Bloch-wave formalism it is straightforward to calculate the extinction distance,

$$\xi = \left(k^{(i)} - k^{(j)}\right)^{-1} \tag{19}$$

where $k^{(i)}$ and $k^{(j)}$ denote the eigenvalues of the two most excited Bloch states [16]. Solving the corresponding eigenvalue problem for 200 keV electrons we find $\xi_{SrO} \approx 14$ nm for a SrO atom column, $\xi_{Ti} \approx 38$ nm for a Ti atom column. Comparing these values with those of the intensity distribution obtained by image simulation displayed in Fig. 8 we find that the atom positions appear brightest at depths of odd multiples of half the extinction distance, i.e. at about 7 nm for SrO and at about 19 nm for Ti. For O the extinction distance is so large that for moderate sample thicknesses the intensity of oxygen atom positions in the images is always in the increasing-intensity range. This means that at $C_S = 0$ and $Z = 0$ the contrast is essentially determined by amplitude contrast, bright on a dark background, induced by electron diffraction channeling.

In summary, the strong atom contrast under NCSI conditions is due to additive contributions of both *amplitude* and *phase* contrast. The channeling-induced amplitude contrast is always bright on a lower-intensity background. The result are bright atom positions. If you combine this with the classical positive phase contrast (at positive residual values of C_S) , which by itself results in dark atoms on a light background, the outcome is in sum an overall *weakened* contrast at the atom positions. If, on the other hand, the amplitude contrast is combined with negative phase contrast (at negative residual values of C_S), which for itself also results in bright atom positions at moderate sample thicknesses, then in sum you get an increased bright contrast of the atoms on a dark background. The

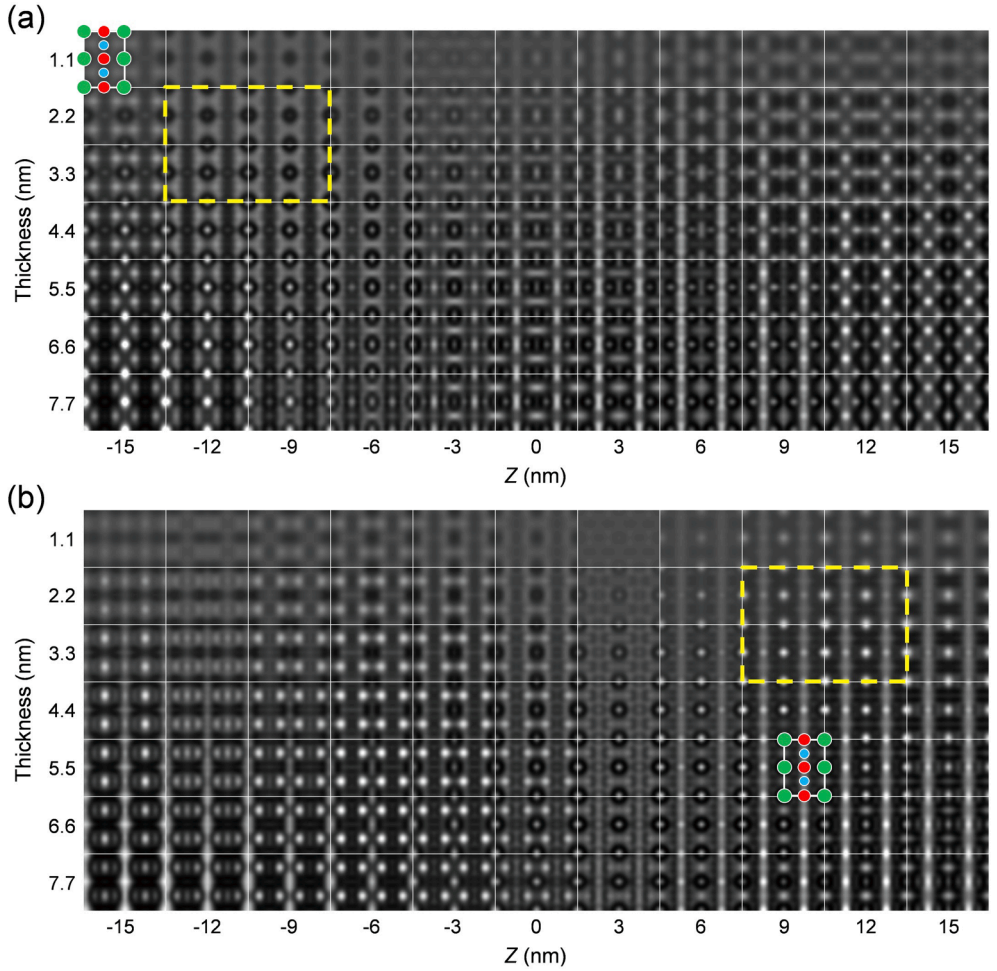

Fig. 6. Simulated images for $SrTiO_3$ at 200 keV in [011] projection. In (a) the unit cell is depicted in the upper left corner (SrO: large green circles; Ti: medium size red circles; O: small blue circles). The lattice parameter is $a = 3.9$ Å. The composite shows a unit, two lattice unit cells wide (white rectangles) for different defocus values Z and, from top to bottom, increasing sample thickness. (a) $C_S = +40$ µm. (b) $C_S = -40$ µm. The frame, dashed yellow line, marks an area of same sample thickness. Oxygen between the titanium atoms can clearly be seen in (b) but not in (a). Note that for comparison with Fig. 5 this figure has to be rotated by 90°. We note here in addition that the focal length of the objective lens is not a constant and that it can be continuously changed by the operator by varying the object lens current. The thickness of the specimen is not known a priori. The figure shows that this leads to all kinds of "images" which in general have visually not much to do with the real structure of the object. Only in special cases, which have to be determined by means of image simulation, the image provides an intensity distribution immediately similar to the structure of the object.

contrast is further enhanced by the fact that, on the one hand, the concentration of electrons at the atomic positions lowers the intensity between the atoms and, on the other hand, the bright negative phase contrast is stronger than the positive phase contrast in "not so weak", i.e. more realistic specimens[16]. Compare also Ref. [98].

4.4. More on NCSI: The dependence on sample thickness

We note that the type of imaging of materials science samples under negative C_S and overfocus conditions discussed here is a new technique that had never been considered or treated before the advent of aberration-corrected electron optics. Imaging in the NCSI mode today represents the basic operation mode of modern aberration-corrected CTEM. However, because of its novelty, it is not yet

[16] For an understanding of the NCSI mode, it is important not to confuse it with a suggestion by Scherzer in 1970 as part of a theoretical investigation of the optimal conditions for imaging atoms in future aberration-corrected electron microscopes [98]. Scherzer pointed out that in the context of the weak-phase object (!) approximation one must optimize the entire aberration function for the optimal approximation to the Zernike case and that it may then be appropriate, depending on the magnitude of a fixed C_5, to invert the sign of the variable C_1 and C_3 to compensate for a correspondingly high value of C_5. Amplitude contrast as it is treated here was not considered in [98].

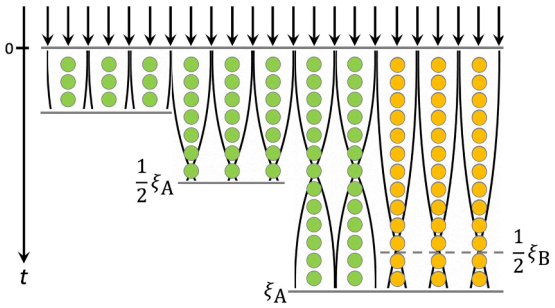

Fig. 7. Schematic illustrating the effect of electron diffraction channeling on the local electron current density distribution for three different sample thicknesses t. At the sample entrance surface ($t = 0$) the electron current density distribution is assumed to be laterally uniform (parallel arrows). The interaction with the positively charged atom cores concentrates the electrons with increasing depths towards the atom strings. This leads to enhanced current density at the atom positions with a maximum at a depth of odd multiples of $\xi/2$, where ξ is the effective extinction distance, at the expense of the current density in between the atoms. This induces an "amplitude structure" of the sample at the exit surface. At larger sample thicknesses the current density at the atom positions decreases again and ideally (neglecting inelastic scattering) becomes essentially uniform again at depth ξ. Note that the extinction distance is inversely proportional to the scattering potential and therefore depends on the atomic species forming the atom strings. The nuclear charge number of atom species "A" (green) is higher than that of atom species "B" (orange), and therefore $\xi_A < \xi_B$.

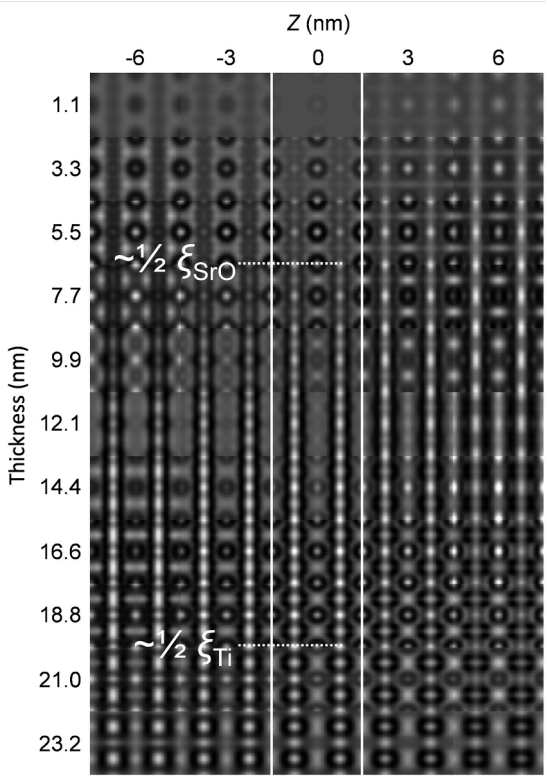

Fig. 8. Simulated images for $SrTiO_3$ at 200 keV. The composite shows a single unit cell in [011] projection for different defocus values Z and sample thicknesses. The calculation is carried out for $C_S = 0$. The central vertical stripe, $Z = 0$, depicts the case for pure diffraction channeling. The horizontal dotted lines show that the maximum intensity at the SrO-atom and Ti-atom positions occurs at a sample depth (thickness) of half the extinction distance ξ_{SrO} and ξ_{Ti}, respectively (compare with Fig. 7).

described in textbooks. Therefore, it seems appropriate to place the NCSI method in a broader context with respect to its dependence on specimen thickness and to show examples of it (in the next section). This will confirm what is already largely evident from Figs. 6 and 8, that the method is extraordinarily robust with respect to a change in the imaging parameters. From the smallest to the highest sample thicknesses occurring in practice, NCSI proves to be superior to PCSI.

We assume for simplicity a primary incident beam and a single scattered beam. And we discuss first the case *without* a Zernike phase

plate (see section 4.2). Then, with respect to the incident beam, the phase of the scattered beam at small sample thickness (just below the entrance surface) starts with π/2. But as the wave field advances the specimen's scattering potential induces an *additional* phase shift increasing with specimen depth. For a total phase of the scattered beam of π, maximum positive phase contrast is achieved (scattering centers dark on a bright background). For the phase of 3π/2 the contrast of the scattering centers changes from dark to bright and negative phase contrast is obtained (scattering centers bright on a dark background), since starting at this angle, up to 5π/2 the vectors of the primary beam and the scattered beam are additive. Optimum phase contrast occurs at a total phase of the scattered beam of πm with ($m = 1,3,5,\ldots$) for positive and ($m = 2,4,\ldots$) for negative phase contrast. The increase of the phase change per unit depth is proportional to the scattering potential. As a consequence, in order to obtain always maximum positive or negative phase contrast the remaining difference between the phase angle of the scattered beam at a particular sample thickness and of the nearest optimum angle has to be supplied by the equivalent of the Zernike phase plate. We note that this is, of course, not a special feature of NCSI and therefore also applies to PCSI. As soon as the potential-induced advancement in phase of the scattered beam is taken into account, optimum contrast in principle always requires an appertaining optimization of the aberration function.

The optimum conditions for bright-atom contrast have been studied in [43] in the framework of a simple independent-atom string model for describing the diffraction channeling effect [99]. In the following a brief sketch of this treatment is presented. The electron wave $\psi_e(\boldsymbol{r})$ at the exit plane of the specimen is written as the sum of a direct, unscattered wave ψ_0 and a scattered wave $\psi_s = \psi_e(\boldsymbol{r})$- ψ_0. Properly adjusting the aberration function of the objective lens a constant phase $-2\pi\chi_0$ is added to the phase of the scattered wave. This is equivalent to a suitable Zernike phase plate and allows us to achieve the closest maximum of positive or negative phase contrast. Then the wave function in the image plane $\psi_i(\boldsymbol{r})$ can be written as

$$\psi_i(\boldsymbol{r}) = \psi_0 + [\psi_e(\boldsymbol{r}) - \psi_0]\exp(-2\pi i\chi_0) \tag{20}$$

Considering in Eq. (5) only the term for defocus and for third-order spherical aberration optimum contrast is obtained for the following settings for the defocus

$$Z = \frac{8\chi_0}{\lambda g_I^2} \tag{21}$$

and the spherical aberration parameter

$$C_S = -\frac{40\chi_0}{3\lambda^3 g_I^4} \tag{22}$$

In the framework of the independent-atom string model the expression for the direct and the scattered wave, respectively, is

$$\psi_0 = \cos\tau + i\left(\frac{U_0}{k}\xi - 1\right)\sin\tau \tag{23}$$

$$\psi_s = i\frac{[U(\boldsymbol{r}) - U_0]\xi}{k}\sin\tau \tag{24}$$

with $\tau = \pi t\xi^{-1}$, and the wave vector k is defined as above. ξ is the two-beam extinction distance. The substitution $U(\boldsymbol{r}) = 2me/h^2\, V(\boldsymbol{r})$ contains the projected electrostatic potential V(r). U_0 denotes the mean inner potential. Defining the characteristic parameter

$$\zeta = \frac{U_0}{k}\xi - 1 \tag{25}$$

the image intensity distribution for coherent illumination becomes

$$I(\boldsymbol{r}) = |\psi_i|^2 = (cos\tau)^2 + \zeta^2(sin\tau)^2 - 2\frac{[U(\boldsymbol{r}) - U_0]\xi}{k}sin\tau$$

$$\times Im[(cos\tau - i\zeta sin\tau)exp(-2\pi i\chi_0)] + \left[\frac{[U(\boldsymbol{r}) - U_0]\xi}{k}\right]^2(sin\tau)^2 \tag{26}$$

The first term is the intensity of the direct wave providing uniform background intensity. The second term describes the linear interference between the direct and the scattered wave. The last term describes the intensity of the scattered wave. The maximum contrast at the atom positions occurs if the modulus of the expression in the second line adopts a maximum value and if its sign is opposite to that of sin τ. For the aberration interval of $-\frac{1}{2} < \chi_0 < +\frac{1}{2}$ both conditions are met for

$$\tan 2\pi\chi_0 = (\zeta\tan\tau)^{-1} \tag{27}$$

and

$$\tan\tau\sin 2\pi\chi_0 > 0 \tag{28}$$

For a given material the optimum contrast condition is then obtained employing the proper values for U_0 and ξ by calculating the value of the characteristic parameter c and solving Eq. (27) for χ_0 subject to fulfilling the condition Eq. (28) (see Fig. 9). Both electron

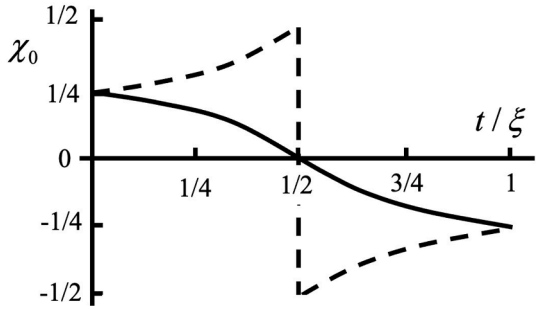

Fig. 9. Optimum value of the aberration function χ_0 (see text and Eqs. (27,28)) compensating the phase of the scattered wave in order to obtain maximum negative phase contrast (bright atom positions on a dark background) for different sample thicknesses t in units of the extinction distance ξ. Plotted are the two cases for the characteristic parameter ζ (Eq. (24)) i.e. $\zeta > 0$ solid line, and $\zeta < 0$ dashed line (Reproduced from [43] with permission of Elsevier).

diffraction channeling and the image intensity have a thickness period equal to ξ. The phase of the scattered wave with respect to the direct wave starts with $\pi/2$ (corresponding to $\lambda/4$). It remains positive in the first half of the extinction period and turns negative in the second half, approaching $-\pi/2$ at ξ. For $\zeta < 0$ the phase increases in the first half of the extinction period from $\pi/2$ to π; and in the second half from $-\pi$ to $-\pi/2$. For $\zeta > 0$ the phase decreases in the first half of the extinction period from $\pi/2$ to 0, and in the second half from 0 to $-\pi/2$. The conditions Eqs. (27,28) determine how the equivalent of the Zernike phase plate compensates the phase of the scattered wave favorably. For the first half of the extinction distance χ_0 is positive, for the second half it is negative. Hence the approximation of the Zernike phase plate by defocus and spherical aberration, Eqs. (21,22), yields, for negative phase contrast, an overfocus combined with a negative value for C_S for the first half of the extinction distance, and an underfocus combined with a positive C_S for the second half. Approaching a specimen thickness just smaller than half the extinction distance the favorable compensation is achieved for $\zeta < 0$ with a defocus

$$Z = \left(2\lambda g_1^2\right)^{-1} \tag{29}$$

and a value of the spherical aberration parameter of

$$C_S = -20\left(3\lambda^3 g_1^4\right)^{-1}. \tag{30}$$

For a specimen thickness just larger than half the extinction distance the favorable compensation is achieved with the same settings but with the respective signs inversed. For $\zeta > 0$, the favorable compensation at half the extinction distance is achieved with $Z = 0$ and $C_S = 0$.

We note that the theoretical treatments as well as the experiments show that the contrast conditions are rather robust with respect to a variation of defocus and specimen thickness. We further note that also the adjusted value of C_S can vary over a wide range. Even a deviation of 30 % of the calculated optimum value does not destroy the high-resolution contrast although it certainly changes the absolute contrast behavior. The robustness of the bright-atom contrast conditions with respect to variations of C_S, Z, and t can be explained in the two-level channeling model just described by the relatively weak phase-variation of the scattered wave and by the tolerance limits for the respective aberration settings [94,99]. Although the absolute values of the imaging parameters are important for quantitative contrast evaluation the NCSI mode *per se* does not make high demands with respect to the adjustment of particular values of these parameters. Finally, we would like to point out once again that the treatment of NCSI contrast for higher sample thicknesses presented here was only intended to provide a qualitative overview. In reality, we are dealing with many beams and corresponding extinction lengths, which in turn depend on the type of atoms in the potential string. These things are automatically taken care of in a full dynamical treatment of the scattering and imaging problem on the computer.

4.5. *Case study $SrTiO_3$*

In the following we compare by image simulations for the case of $SrTiO_3$ the NCSI mode with the PCSI mode with respect to the obtained contrast [100]. The images were calculated for an aberration corrected 300 keV instrument employing optical imaging parameters for an information limit of 0.08 nm [42,79,94]. In order to be able to make this comparison quantitatively on the basis of the state of the art, the following corrections were made, the details of which, in order to keep to the sequence of the presentation, can only be explained farther down. The calculated intensity values were corrected on the basis of the measured actual camera modulation transfer function (MTF; see below). In addition, the effect of an additional contrast damping due to e.g. mechanical vibrations of the microscope or electrical instabilities (image spread; see below) was taken into account by convolution of the intensity distribution by a Gaussian function characterized by an rms value of 30 pm. Furthermore, we will use here and in the following a definition of "contrast" that is a generalization of the classical term [46] and that is now generally accepted in modern quantitative electron microscopy. For this, following Hÿtch and Stobbs [101], the mean image intensity (over all pixels in a given image area) is calculated, and normalizing its value to 1, the so called *image contrast* is obtained as the standard deviation.

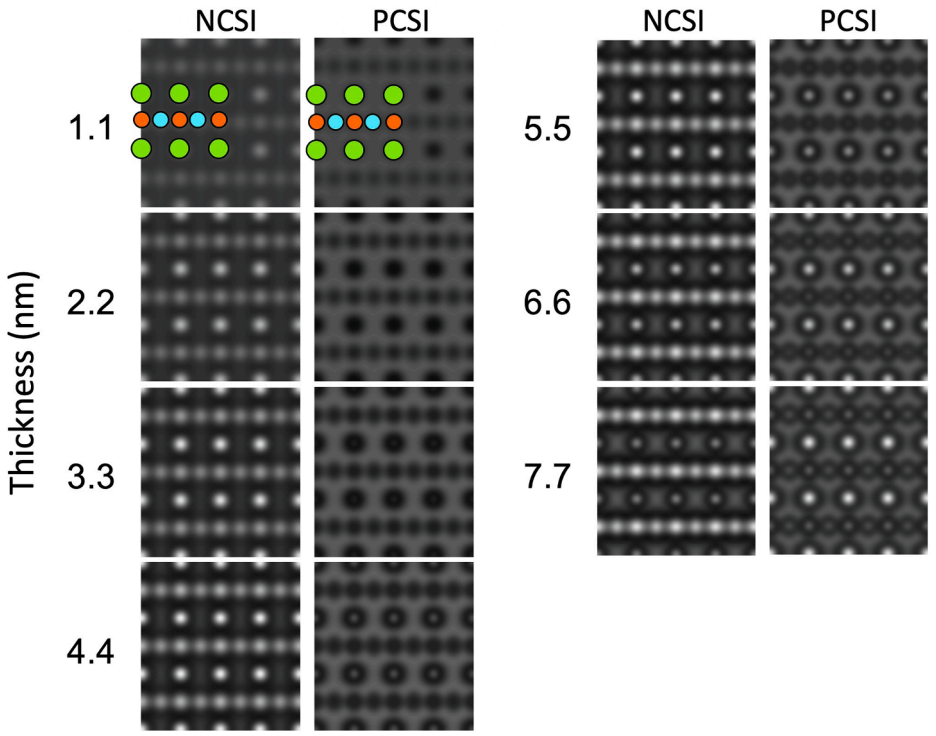

Fig. 10. Simulated thickness series of images for $SrTiO_3$ [011] calculated for the NCSI mode and the PCSI mode, respectively, at 300 keV. Inset: structure model. The NCSI mode (C_S = -15 μm; Z = +6 nm) leads to bright atom contrast on a dark background. This contrast is preserved up to the sample thickness t of 7.7 nm and beyond. The PCSI conditions (C_S = +15 μm; Z = −6 nm) result in dark atom contrast for relatively thin objects (t < 4.4 nm), while bright intensity peaks appear at the SrO atom positions for higher thicknesses. In the upper part of the figure the atom positions of $SrTiO_3$ are given schematically (SrO: green; Ti: red; O: blue). (Reproduced from [100] with permission of Springer Nature).

Fig. 10 shows a thickness series of images calculated for the two alternative imaging modes. The NCSI mode leads to bright atom contrast on a dark background. This contrast is preserved up to a sample thickness t of 7.7 nm and beyond. On the other hand the PCSI mode results in dark atom contrast for relatively thin objects (t < 4.4 nm), while bright peaks appear at the SrO atom positions for higher thicknesses. Fig. 11 displays the image contrast as a function of thickness. The contrast resulting from the two modes exhibits the same value up to an object thickness of 1 nm. In NCSI the contrast grows with increasing thickness up to about 5 nm reaching a saturation value of about 0.27. The contrast increase of the PCSI mode is much lower, and a plateau occurs already in the thickness region of 3 nm ≤ t ≤ 7 nm. There the NCSI contrast is on average by about a factor of 2 stronger than the PCSI contrast. We note that this comparison neglects the fact that under PCSI conditions and larger sample thicknesses the different atom species appear at

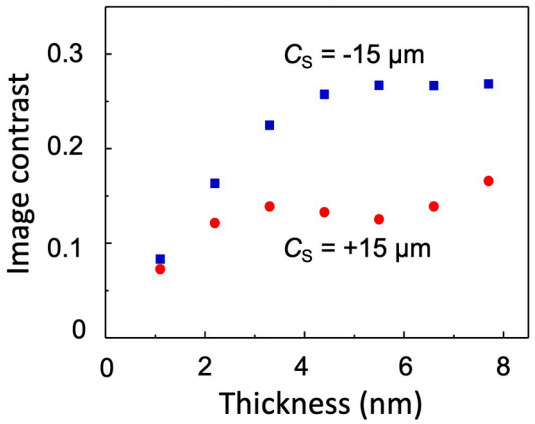

Fig. 11. The image contrast as a function of specimen thickness. In the case of NCSI (blue squares) the contrast is growing with increasing thickness up to about 5 nm, where it reaches a saturation value of about 0.27. The contrast increase of the PCSI mode (red circles) is much lower, and saturation occurs already in the thickness region between 3 and 7 nm. (Reproduced from [100] with permission of Springer Nature).

different contrast (bright on a dark background for SrO and complicated grey-scale contrast for Ti and O) which is not very convenient for quantitative studies.

The obtainable signal-to-noise ratio depends directly on the image intensity recorded at an atom column position and this determines the precision (see below) of position and occupancy measurements. The intensity values for the three types of columns, SrO, Ti, and O are plotted in Fig. 12 for a sample thickness of 3.3 nm. At this thickness, the image taken under PCSI conditions has essentially reached its plateau contrast level while the already much superior contrast level in the NCSI case increases further at larger thickness. For a quantitative comparison, the ratio of the column-based signal strength between the two imaging modes is defined by the ratio of the respective intensity extrema at the atom positions, given by $(I_{max} - 1)_{NCSI} / (1-I_{min})_{PCSI}$. The calculated results are 3.6 for SrO, 2.4 for Ti, and 2.1 for O, respectively. These ratios of the extremal values between the NCSI and the PCSI modes are for all individual column types even larger than the corresponding ratio of the overall image contrast of 1.6. This reflects the much stronger "focused" shape of the atomic images in the NCSI mode.

Fig. 13 shows the dependence of the image intensity on the atomic nuclear charge number N_Z accumulated per individual atomic column along the viewing direction. It is noted that along the <110> direction a unit cell period of $SrTiO_3$ includes one strontium plus one oxygen atom in the SrO column, one Ti atom in the Ti column, and two oxygen atoms in the oxygen column. The atomic charge number accumulated over a single unit cell period ΣN_Z are thus 46, 22, and 16, respectively. For the NCSI mode, the image intensity of all atom positions follows essentially a linear dependence on the total atomic charge number accumulated up to a thickness of at least 3.3 nm. Beyond this thickness the linear relation is still valid for the lighter Ti and O columns, whereas the linearity is lost for the SrO columns due to their shorter extinction length. In the case of the PCSI mode, the linearity between atom-position intensity and the accumulated atomic charge number is already lost for all column types at a thickness of 3.3 nm. Most importantly, the linear dependence of the intensity on the accumulated atomic charge number exhibits also a higher slope in the NCSI mode compared to the PCSI mode.

5. Inversion of the imaging process

5.1. General

An image taken under high-resolution conditions may exhibit an intensity distribution looking like an 'image' of the arrangement of the atoms in the crystal. But what this image is really worth, qualitatively and even more so quantitatively, can only be decided on the basis of a quantitative image simulation. This means that in order to exploit the full potential of aberration-corrected electron microscopy the numerical inversion of the imaging process is mandatory. Admittedly, CTEM will not always be performed under conditions where ultra-precise measurements are concerned. However, as the simulated images of Fig. 6 show, the images of one and the same atomic structure can look very different depending on the thickness of the sample and the defocus value chosen. Therefore, it is recommended to calculate, for the purpose of orientation, the expected images in advance for a reasonable range of imaging conditions

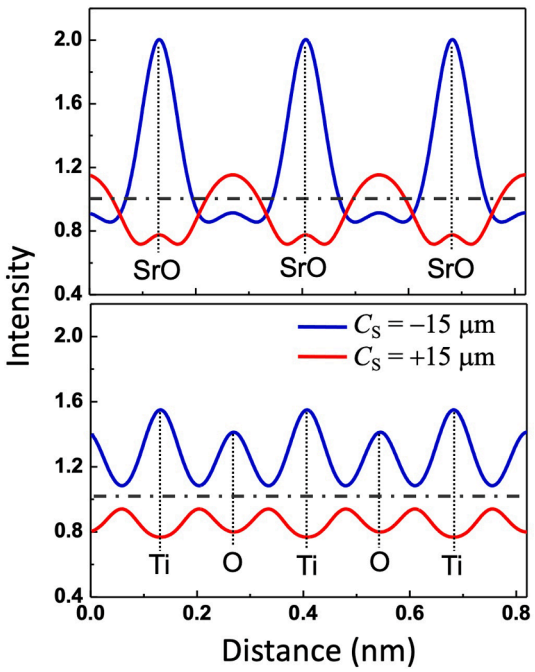

Fig. 12. Plot of the intensity values for SrO, Ti, and O atom positions for a sample thickness of 3.3 nm. Blue line: NCSI. Red line: PCSI. The mean intensity 1 is denoted by a dash-dotted line. (Reproduced from [100] with permission of Springer Nature).

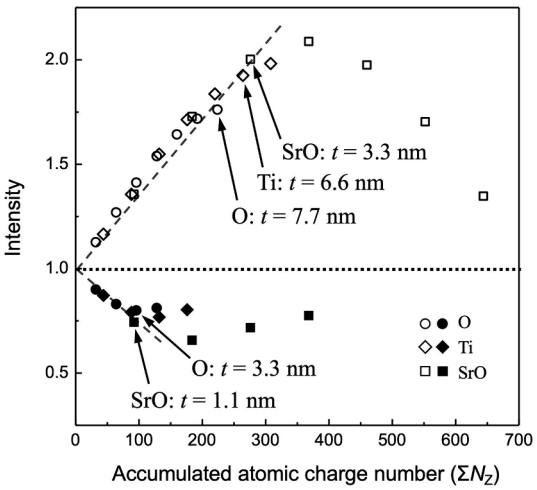

Fig. 13. Dependence of the image intensity on the atomic nuclear charge number N_Z accumulated per individual atomic column along the viewing direction. NCSI: Open symbols; PCSI: solid symbols. Along the [011] direction a unit cell period of $SrTiO_3$ includes one strontium plus one oxygen atom in the SrO column, one titanium atom in the Ti column, and two oxygen atoms in the oxygen column. The atomic nuclear charge number accumulated over a single unit cell period is thus 46 (SrO), 22 (Ti), and 16 (O), respectively. $\sum N_Z$ denotes the total atomic nuclear charge number along an atomic column of length t. (Reproduced from [100] with permission of Springer Nature).

before starting the actual investigation in the electron microscope.

The inversion of the imaging process – from the measured intensity distribution in the image back to the atom distribution in the specimen – is carried out in two steps. The *first step* is the reconstruction of the electron exit-plane wave function (ψ_e). As we will see in the following, it is possible today to achieve agreement of the calculated with the experimental images at absolute values of the image contrast. In this case a precise result can be obtained on the basis of only a single experimental image. Among other things, this is helpful when dealing with radiation-sensitive materials that cannot tolerate longer image acquisition times. On the other hand, we have seen that Lentzen's optimization of the contrast transfer function, which aims for the highest possible value of g_1, achieves this value at the expense of a degraded transfer at low values of g. Therefore, if the goal is to improve contrast transfer at low spatial frequencies, it may make sense to go to higher defocus values, even if this comes at the expense of the transfer at higher spatial frequencies. Indeed, in order to image a long-range contrast modulation, the operator will automatically set an appropriate defocus value. Therefore, for quantitative studies where one is interested in information about both the highest and the lowest spatial frequencies into the image, the classical *focus-variation technique* remains the method of choice [102–107]. A series of (typically about 20) images is acquired in which the focus of the lens is varied in steps (typically about 2 nm) around a central value. These images form the set of primary experimental data. These must be corrected for the nonlinear spatial-frequency transfer characteristics of the camera used to acquire the images (see below). The corrected data set then forms the input for the numerical reconstruction of the exit-plane wave function using one of the software codes that employ maximum likelihood methods. We recall that the focus variation technique dates from the time when aberration-corrected electron optics did not exist and image information was necessarily limited by gaps in the contrast transfer function. It takes advantage of the fact that varying the lens focus results in a shift in the contrast transfer function and the associated transfer gaps. Joint processing of the information from the images obtained for the different defocus settings allows direct access to the amplitude and phase of the underlying electron wavefunction without significant transmission gaps, similar to what is done in the different forms of electron holography, and the microscope aberrations at the time of image acquisition can be determined this way (see e.g. [41,108,109]). For early work on lattice defects combining aberration corrected CTEM with the focus-variation technique we refer to [110–112].

The reconstructed electron exit-plane wave function does in general not supply us with a direct representation of the set of atomic coordinates. Neither a mapping of the real nor of the imaginary part of ψ_e gives us unambiguously the correct atomic sites. As described in the previous sections, depending on the sample thickness, the contrast may vary dramatically and in a complex fashion which cannot be understood intuitively. Furthermore strictly speaking the ψ_e obtained is the wave function of the "real" case. This means that the amplitude and phase distributions depend on the actual specimen thickness, and a tilted specimen yields as a result a "tilted" wave function. Of course the set of wanted atomic coordinates must be universal and therefore independent of imaging circumstances. This means that the backward calculation has to be continued by performing the *second step*. The *second step*, from ψ_e to the atomic structure, requires the construction of an atomic model (first guess) on the basis of which the Schrödinger equation is solved and the associated exit-plane wave function is calculated. In a comparison between the calculated and the experimental wave function, corrections to the model are determined and the Schrödinger equation is solved again. In this iterative process the model is improved step by step. We would like to point out that this procedure concerns all details that are to be measured; this means the chemical nature of the atoms that make up the structure of the sample as well as the adjustment of the atomic positions. For example, if the goal is to measure the structure of an extended dislocation core to within a few picometers, then this means varying the position of possibly several tens of atomic positions with picometer precision. Since neither the sample thickness nor the beam tilt is in general known with

sufficient accuracy, these have to be treated as free parameters in the iterative fit of the model in order to reach an optimum match between calculated and experimental exit-plane wave function. Only after a self-consistent set of atomic coordinates, occupancies and imaging parameters is obtained we may consider the problem solved.

5.2. The imaging parameters

It is obvious that to reconstruct the exit-plane wave function, the optical parameters that appear in the aberration function must enter the calculation with the value they had at the time the image was acquired. It is not guaranteed that these values correspond to those measured at the beginning of the session using the Zemlin tableau technique. Therefore, to get an impression of the stability of the values, it is recommended to measure these aberrations not only before but also after the image acquisition. Since this generally requires shifting the sample position to an amorphous region or even replacing the sample with an amorphous test sample, it is possible that the result will be ambiguous because a measurement error cannot be distinguished from a real change in the imaging parameters being measured. The only way out of this dilemma is to consider the imaging itself as a quantum physical experiment by which the aberrations can be measured as long as we have a structure whose precise atomic coordinates are known (see below). If such a reference structure is not part of the specimen, this means that we have to carry out a full and self-consistent run of the whole image-process inversion in which the exit-plane wave function is calculated with the residual aberrations taken as free parameters.

Another problem is the limited accuracy of aligning the direction of the incident electron beam with the chosen low-index direction of the crystal. On the one hand, in a mechanical goniometer, the precision of tilting a sample about two mutually perpendicular axes is far too inaccurate for the alignment of atomic columns, not least because of the insufficient backlash properties. On the other hand, the change in intensity distribution in both the diffraction pattern and the atomic image is far too inaccurate an indicator with respect to setting an optimal sample orientation. Therefore, with the current state of the art, residual sample tilt angles in the order of about 5 to 10 mrad can hardly be avoided. That the poor adjustability of sample orientation is a problem for microscopy in atomic dimensions can be readily illustrated by the fact that in a (011) oriented $SrTiO_3$ sample, which has a thickness of 10 lattice unit cells, 5.5 nm, at a tilt of 5 mrad, the lowest Ti atom with respect to the uppermost, has a lateral displacement of 28 pm. This is indeed significant considering that we can today measure lateral atomic displacements down to about 1 pm with CTEM. Moreover, in the image the shifts of the contrast maxima inside a crystal unit cell containing different atom species cannot simply be related to each other by means of a purely geometrical factor representing the effect of the tilting angle. This is a result of the nuclear-charge dependence of electron diffraction channeling and of the correspondingly different shift of atomic maxima on specimen tilt. An illustrative example is the case of Fig. 5. At first glance, the content of this image appears to be an almost perfect image of the $SrTiO_3$ crystal with atomic resolution. However, careful inspection of this image (e.g. by regarding it at glancing angle parallel to [100]) shows that the Ti-atom positions are shifted by about 35 pm to the left, parallel to $[0\bar{1}1]$, with respect to the vertical line (parallel to [100]) connecting the SrO positions. In reality the SrO- and the Ti-atom positions should be collinear. Also the O-atom positions are shifted to the left with respect to the midpoint of the two adjacent Ti-atom positions. As shown by image simulations this discrepancy is due to a sample tilt of about 7 mrad. If not properly taken into account in the numerical calculations these different tilting-induced shifts of the contrast maxima will lead to erroneous results.

As the simulated images, Figs. 6, 8, 10, demonstrate, the contrast in the atomic image depends very sensitively on sample thickness. However, except in special cases, this is not known a priori. In fact, in atomic dimensions, the only way to determine the thickness of a sample is to perform a quantum physical scattering experiment. In the case of electron microscopy, this is the imaging process itself, which includes quantitative interpretation using computer simulation. Therefore, when solving the Schrödinger equation in the context of image calculation, the sample thickness parameter must always be taken as a variable. On the other hand, it is in this way possible to measure the sample thickness to an atomic monolayer, i.e. with single-atom precision.

An imaging parameter that is rarely mentioned is the *electron dose rate* used to obtain an image or the total dose to which a specimen is exposed in a given investigation. Damage to the specimen caused by electron irradiation has always been an issue. Two types of processes are in general considered. First, there is the damage caused by electron–electron interaction. It is a type of radiolysis that also plays a role in other types of irradiation. Electron-electron interaction is described by the relativistic Bethe-Bloch theory, and its cross section is inversely proportional to $\beta^2 = v_e^2/c^2$ (where v_e is the electron velocity, and c is the velocity of light), i.e. it decreases with increasing electron energy [16,113]. The opposite is the case for the second effect, atom displacement damage. Its cross section increases with increasing electron energy from a critical displacement threshold-energy value on. This was exploited in the sixties and seventies for studies on atomic defects and radiation damage in metals in high-voltage electron microscopes operated at voltages of typically 500 to 1200 kV (e.g. [114–116]). On the other hand, the observation of atom displacement damage in graphene and other carbon-based structures at electron energies higher than 80 keV was the reason for the construction of low-voltage electron microscopes operating at electron energies down to 15 keV [26–29]. A recent review on electron-beam damage is given by Egerton [117].

There are two reasons to have a careful look at electron-radiation effects in atomic-resolution electron microscopy. The first reason concerns the so-called Rose criterion [118] which states that for a given signal-to-noise ratio and for a given value of contrast, the minimum dose to resolve an object distance d increases with decreasing d as $1/d^2$ [16,18,117,119]. Experimental data are compiled in [120]. Accordingly imaging a gold atom at 300 keV with the very low signal/noise ratio of 2 requires a minimum dose of about 2300 e $Å^{-2}$. The corresponding dose for a carbon atom at 80 keV is 20,000 e $Å^{-2}$. Usually, significantly higher signal-to-noise ratios are required (typically up to 5), which, because they enter quadratically, can easily lead to total doses that are in practice higher by more than an order of magnitude. Typical dose rates employed in atomic resolution imaging at 300 keV are between $5x10^4$ e $Å^{-2}$ s^{-1} [120] and $1.3x10^5$ e$Å^{-2}$ s^{-1} [121]. These are by more than two orders of magnitude higher than the dose rates employed in the

aforementioned dedicated radiation-damage studies. In fact, modern electron microscopes are equipped with field-emission electron sources whose special design provides an extraordinarily high brightness and, on this basis, electron beam current densities which are, even for routine applications, orders of magnitude higher than the highest values available in earlier generations of microscopes. The effect of these high beam-current densities on the structure of the samples has been pointed out early on, and it was shown experimentally that, in addition to the generation of atomic defects at electron energies above the atomic displacement threshold, jumps of atomic defects or of weakly bound atoms (for example on surfaces) are possible by low-energy (sub-threshold) transfers from the electrons. This phenomenon was termed *radiation-induced diffusion* [122]. Electron-beam induced atom motion and bond modification were observed in an investigation of rhodium catalysts and of graphene in the TEAM instrument operated at 80 kV [123]. Experimental evidence for radiation-induced jumps of weakly bound bismuth atoms was obtained in a study of bismuth zinc niobate pyrochlore at 300 keV [124]. Another effect that has been intensively discussed recently is the possibility that the low-energy momentum transfers from the fast electrons occurring at very high rates may result in atomic vibrations that affect the atomically resolved images [123,125]. However, in a dedicated study quantitatively investigating the contrast of atomic images of MgO, Ge, and Au samples as a function of dose rate, no effect of electron dose rate on contrast was found at 300 keV upon variation of the dose rate between $1x10^3$ e $Å^{-2}\,s^{-1}$ and $1.3x10^5$ e $Å^{-2}\,s^{-1}$ [121]. A novel way to reduce electron beam damage was recently investigated in a study of the radiation sensitive compound $MgCl_2$ at 200 keV. Instead of the usual continuous irradiation, a pulsed electron beam (2 ps pulses at 165 ps or 14 ps at 152 ps intervals) was used. The result was a reduction in radiation damage of up to two orders of magnitude for the same total electron dose [126].

5.3. Resolution

Referring to the Rayleigh definition of resolution, this quantity determines the smallest distance that two atomic intensity maxima can have, overlapping in such a way that this distance can just be measured [46,127].[17]

In electron microscopy it is not possible to produce a single figure defining resolution under practical conditions. For CTEM with parallel-beam illumination a number of different approaches to characterize the resolving power have been discussed in the literature [63,76,79,80]. It is now generally accepted that a proven method to characterize resolution is by means of the PCTF for the linear interferences between the transmitted beam and the diffracted beams whose amplitude is increasingly damped with increasing spatial frequency due to instrumental factors. The information limit g_I where the amplitude of the PCTF drops to $1/e^2 = 0.135$ is then taken as the fundamental benchmark parameter characterizing the performance of the instrument. The following instrument-related effects induce a damping of the spatial frequency spectrum [128–131]:

(1) *Partial spatial coherence* (imaging by a *convergent* rather than an ideally parallel electron beam) is taken into account by multiplication of the coherent contrast transfer function $sin2\pi\chi(g)$ by the envelope

$$E_s = exp\Big[-(\pi q_o \lambda)^2 \big(C_S \lambda^2 g^2 + Z\big)^2 g^2 \Big], \tag{31}$$

where q_0 is the $1/e$ width of a Gaussian distribution of components of the incident beam wave vector $k = k_0 + q$ (q – small additional component perpendicular to k_0). The semi-convergence angle $\Theta_0 = \lambda q_0$ is about 0.2 mrad for a microscope equipped with a field emission electron gun.

(2) The effect of *partial temporal coherence* is considered by the envelope

$$E_t = exp\left(-\frac{1}{4}\pi^2 \boldsymbol{\Delta}^2 \lambda^2 g^4 \right) \tag{32}$$

with

$$\boldsymbol{\Delta} = C_C \left[\left(\frac{\Delta E}{E}\right)^2 + \left(\frac{\Delta V}{V}\right)^2 + \left(\frac{2\Delta J}{J}\right)^2 \right]^{\frac{1}{2}} \tag{33}$$

where $\boldsymbol{\Delta}$ denotes the $1/e$ width of a Gaussian distribution of the constituents, relative spread of the electron energy E (source), of the acceleration voltage V, and of the lens current J contributing to the partial temporal incoherence via the objective lens' chromatic aberration with coefficient C_C.

The neglect of non-linear interference terms made by discussing imaging based on a PCTF is a rough approximation that is only justified for the purpose of a general orientation or for weakly scattering objects. A serious treatment of the general problem requires the computation of the Fourier transform of the image intensity, $I(\boldsymbol{g})$, by means of the transmission cross coefficient [132].

[17] Although the Rayleigh definition of resolving power assumes incoherent illumination, this definition is often used for coherent illumination as well. For the latter, the Abbe definition actually applies, differing in the prefactor of the expression relating resolving power at a given numerical aperture to the wavelength of the radiation [46]. It is a common property of the Rayleigh and Abbe definitions that there must be a clear intensity minimum (a dip of about 27% of the intensity of the two maxima) between the two contrast maxima. Unfortunately, the Sparrow definition of resolution is also not infrequently used in the recent literature. This definition leads to smaller nominal minimum distances and thus, superficially regarded, higher resolution values. This is because, according to its definition, the Sparrow value of the distance between the two intensity maxima is reached when these maxima are so close that the intensity minimum just disappears [127].

(3) There are a number of effects that displace the image stochastically by a small amount, and these displaced images are summed up incoherently during the exposure time. The resulting damping of the image contrast is referred to as *image spread*. Typical causes of image spread are mechanical vibrations of the microscope, e.g. due to insufficient isolation from ambient sound or ground vibrations. Mechanical instabilities of the specimen holder are particularly critical with the side-entry object goniometers used today. In addition, there are electrical instabilities, and there are interactions of the electron beam with external electromagnetic fields.

In addition to the sources of image spread already mentioned, an important contribution to image spread results from thermal magnetic field noise, also called Johnson noise. Thermal magnetic field noise originates from the superposition of the magnetic fields of the nanocurrents induced by the individual moving quasi-free electrons in metals. It was previously assumed that these random nanofields annihilate each other in time and space. However, in 2013 Uhleman et al. [61,62] demonstrated by means of model experiments that this is not the case. In fact, the relaxation time of these nanofield fluctuations is substantially longer than the typical time of flight of an imaging electron moving at close distance to vacuum-liner tubes or other magnetic or non-magnetic metallic parts in the microscope[18]. As a result each electron "sees" a different configuration of a quasi-frozen nanofield distribution displacing the image stochastically.

The distribution $f(\boldsymbol{r})$ of the small displacements $\boldsymbol{r}$ caused by the image-spread effect in the two-dimensional image plane is assumed to be given by a Gaussian function with the rms parameter σ, thus

$$f(\boldsymbol{r}) = \frac{1}{2\pi\sigma^2} exp\left(-\frac{\boldsymbol{r}^2}{2\sigma^2} \right) \tag{34}$$

The associated Fourier-space damping envelope due to image spread is then given by

$$E_{\mathrm{is}} = \exp\left[-2(\pi\sigma g)^2 \right] \tag{35}$$

where σ can be termed *parameter of the effective image spread* [59]. This damps linear and non-linear contributions at the same image spatial frequency by an equal amount. This is an essential qualitative difference compared to the previously discussed partial temporal coherence effects, which in general cause quite a different damping of linear and non-linear contributions. The information limit d_{I} caused by the image spread *alone* can then be readily deduced from the condition $E_{\mathrm{is}} = 1/e^2$, which yields the catchy relationship $d_{\mathrm{I}} = g_{\mathrm{I}}^{-1} = \pi\sigma$. The smallest resolvable distance is thus approximately three times larger than the rms image spread.

At this point it is important to point out that the calculations of quantum-physical and optical image simulation, which are unavoidable if one intends to perform quantitative microscopy in quantum physical dimensions, have their limits where stochastic processes such as mechanical vibrations or electrical instabilities, which are unavoidable in real technical constructions, play a role. If one is interested in a description of the experimental intensity distributions in the image that is as precise as possible, then the calculated values must be adapted to this reality by means of an appropriate damping parameter. In practice this is done by a Gaussian blur of the image. Examples will be given below in the application part, Section 6. Since the image spread depends on the instrument and the operating conditions, there is basically no universal value for σ. It must be determined in the course of the self-consistent treatment of the problem.

(4) Another factor, which in principle can also be described formally via an envelope of the PCTF, is the change of the spatial frequency spectrum in the image plane by the *modulation transfer function* of the camera with which the image is recorded. Already in the first years after quantitative image calculations in the computer had become possible, Hÿtch and Stobbs [101] pointed out that, according to the state of the art at that time, the image contrast in the simulated images was, compared to the experimental values, by about a factor of 3 or more too high. This so-called *Stobbs-factor problem* was the subject of discussion for more than a decade [133], and it posed a serious problem on the way to quantitative CTEM. In 2009 it was shown by Thust [134] that the major part of the Stobbs factor has its origin in the nonlinear spatial-frequency transfer characteristics of the camera employed for recording the images[19]. In very general terms, the output signal of the camera $\widehat{I}(x,y)$ can be written as a convolution of the intensity distribution before the electrons enter the camera $I(x,y)$ with the point spread function $P(x,y)$ of the camera. The point spread function includes all influences within the camera, e.g. the effects of the scintillator, of the discrete pixels and of blooming effects in the chip. In Fourier space

$$\widehat{J}(u,v) = J(u,v) \cdot MTF(u,v) \tag{36}$$

where $\widehat{J}(uv) = \mathscr{F}(\widehat{I}(x,y))$, $J(u,v) = \mathscr{F}(I(x,y))$ and $MTF(u,v) = \mathscr{F}(P(x,y))$ is the modulation-transfer function. A one-dimensional section of the MTF measured for the Gatan UltraScan 1000 2k × 2k CCD camera and the Gatan OneView 4k × 4k CMOS camera by the knife-edge method [134–137] is displayed in Fig. 14. The MTF deviates dramatically from the ideal value of 1 already at small

[18] We repeat for the sake of clarity: That an electron flying freely and in vacuum through a thin metal tube could be affected by the nanofields of the high density elementary currents of the quasi-free metal electrons moving randomly in all directions inside the wall of that tube has never been considered before. This means that electrons used for imaging, flying through this metal tube one after another, influenced by the respective nanofields of the electrons in the wall material, arrive in the image plane at slightly shifted positions with respect to each other, so that the atomic contrast figure is broadened, resulting in a deterioration of the resolution. At 300 keV the time for an electron to cover a distance of 1 cm is 43 picoseconds while the lifetime of a nanofield fluctuation is typically between 0.1 and 100 nanoseconds [62].

[19] Photographic film as a recording medium [e.g. 16,17] is no longer in use today. In this review, we will therefore only discuss the recording characteristics of CCD and CMOS cameras.

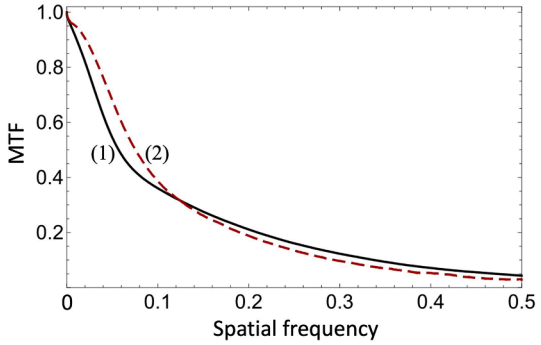

Fig. 14. One-dimensional section of the Modulation Transfer Function (MTF) vs. spatial frequency of (1) the Gatan UltraScan® 1000 2 k × 2 k CCD camera and (2) the Gatan OneView® 4k × 4k CMOS camera measured by means of the knife-edge method [134–137]. In order to eliminate a respective orientation dependence the effect of the pixelation of the camera chip is eliminated. The abscissa gives the spatial frequency in units of 1/pixel. The value of 0.5 corresponds to the Nyquist frequency. The pixel size is 14 μm and 15 μm, respectively. Please note that the value of the MTF should ideally be 1, independent of the value of the spatial frequency. These experimental camera characteristics demonstrate that the frequency spectrum is strongly modified by the camera. For quantitative investigations, the MTF must therefore be measured in order to be able to use an appropriately corrected frequency spectrum in the context of the image calculation.

fractions of the Nyquist frequency, and its value decreases further with increasing spatial frequency. The specific shape of the MTF leads to a particularly strong damping of high spatial-frequency information in the image acquisition process and, if not properly taken into account, to a strong discrepancy between the magnitude of the simulated and the experimental image contrast. At this point it seems appropriate to consider the orders of magnitude. While the modulation-transfer function of the camera can cause a huge contrast decrease up to a factor of three, the contrast-reducing effect of the image spread discussed above is in general substantially smaller and in the order of only 10 %.

The question now arises how the resolution limit of a microscope can be determined experimentally. A widely used method is Young's fringe technique [138]. This test is based on the power spectrum derived from the Fourier transform of an image taken from an amorphous object which, with reference to the angle, is assumed to be isotropically scattering. To distinguish the signal content from the detection noise, two separate images of the same object area are superimposed with a slight lateral displacement, either directly during the experiment by a double exposure, or a posteriori using digital methods on the computer. This results in a fringe pattern in the diffractogram which helps to discern between the transferred signal and the background noise. Although this method has been used for many decades to characterize the resolving power, only in recent years, in the context of measurements on advanced aberration-corrected electron microscopes, it became clear that this approach is flawed for a variety of reasons and that it gives erroneous values, especially at low electron energies [79]. One of the most important reasons for this is the fact that the expression for the image intensity (proportional to $|\psi|^2$; cf. Eq. (3)) due to the formation of the absolute square, has linear and nonlinear contributions, where the latter in the extreme case can have twice the value of the maximum spatial frequency present in the object. A more accurate and quantitative determination of the limitation of resolution due to partial temporal coherence, which is the main limiting effect for transmission electron microscopes equipped with an image spherical-aberration corrector, is achieved by means of the illumination-tilt technique

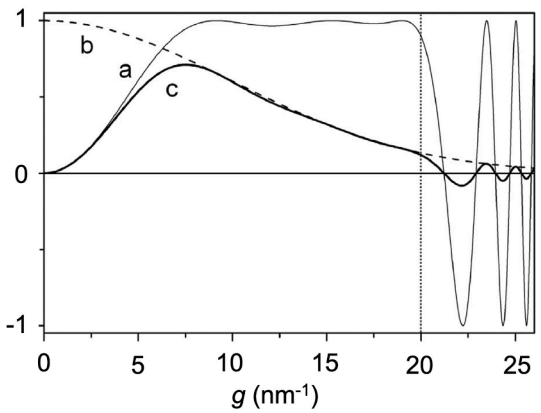

Fig. 15. Calculated phase contrast transfer function vs. spatial frequency g at an electron energy of 200 keV. (a) Coherent contrast transfer function. (b) Image spread envelope function (see Eq. (35)). (c) Resulting effective transfer function. Calculation for: $Z = 3.8$ nm, $C_S = -6.1$ μm, $C_5 = 2.1$ mm, $\sigma = 16$ pm. The spatial frequency corresponding to the information limit is 20 nm^{-1}. Data for the Jülich PICO (FEI Titan® G3 50 – 300) instrument with corrector for spherical and chromatic aberration. (Reproduced from [63] with permission of Elsevier).

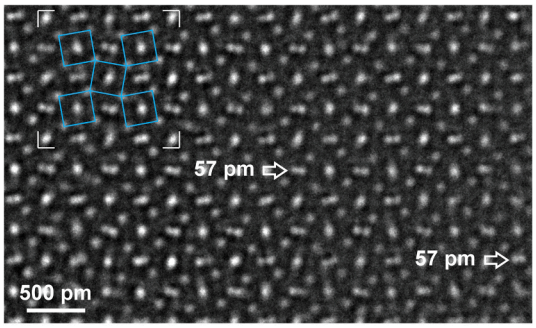

Fig. 16. Ce-doped $YAlO_3$ imaged along the crystallographic [001] direction. NCSI conditions in the Jülich PICO instrument at 200 keV. The schematic in the upper left corner depicts the projection of 2×2 orthorhombic unit cells. Projected oxygen octahedra (oxygen atoms at the corners) are indicated by blue lines. Close Y-Y atom pairs (nominal lateral atom separation 57 pm) occur in two different orientations. Two cases of this 57 pm atom separation are indicated. Other pairs show larger separations up to about 80 pm. These cases are explained to be the result of structural relaxations in the thin sample (about 1.7 nm thick). (Reproduced from [63] with permission of Elsevier).

[79].

In order to allow a comparison of the practical performance of different instruments, resolution has inevitably to be defined universally and independent of sample parameters. In reality, however, the latter may be decisive for the direct perception of resolution in practical work. The concept of *object resolution* has been introduced for cases where, e.g. due to the width of the atomic scattering potential, two atomic features cannot be separated, not because of optical reasons, but as a result of the wide and therefore overlapping contrast figures. Therefore, the actual resolving power of the instrument cannot be recognized in experimental images of such close atom arrangements [76]. Today, where information limits in the range of 50 pm are characterizing high-resolution electron microscopy in aberration-corrected instruments, the problem of an insufficient atomic-signal separation in the image due to particular object parameters applies in almost any material case. The way out of this dilemma is image simulation and the quantitative comparison of experimental image intensities with calculated values on the *same absolute* scale. In this case the real atomic separation in the sample can be determined irrespective of whether this is directly visible in the images or not.

In instruments offering both spherical and the chromatic aberration correction, like the Berkeley TEAM [58–60] and the Jülich PICO (FEI Titan G3 50-300) [63] instruments, the two major resolution limitations of previous instrument generations due to partial spatial and partial temporal coherence are significantly reduced. The ultimate spatial resolution of the microscope is then limited by the image spread. A practical case is depicted in Fig. 15. With $\sigma = 16$ pm an information limit of 20 nm^{-1} at 200 keV is obtained. This corresponds to the results of an experimental diffractogram (Fourier transform) of an image of gold nanoparticles on an amorphous carbon support showing information transfer down to 50 pm [63]. A test sample that demonstrates this resolving power in practice is [010] oriented yttrium orthoaluminate ($YAlO_3$). It contains a close Y-Y-atom pair with 57 pm lateral separation. As shown in Fig. 16 this is well resolved, marking the current experimentally demonstrated record resolution in 200 keV CTEM.

5.4. Precision

For practical application it is important to distinguish resolution from *precision*. As we have seen, the definition of resolution concerns atomic contrasts that partially overlap (Fig. 17a). Precision, on the other hand, describes the accuracy with which we can measure the lateral distance between two atomic positions in the object that are far enough apart that their contrast maxima do not overlap in the image (Fig. 17b). This case occurs largely as a normal case in materials science, for example, when we want to measure the displacement of one atom relative to another in order to determine atomic displacements within a dislocation core, or to measure local electric polarization. Precision is mainly limited by the signal-to-noise ratio, which determines the accuracy with which the position of an atomic intensity maximum can be measured [139,140,111]. The precision of the best instruments in CTEM is of the order of a few picometers, i.e. by more than an order of magnitude better than the resolution. This means that, for example, displacements of atoms of only a few picometers can be measured within a unit cell or at interfaces, although the resolution of the respective microscope is "only" 50 pm or worse. This high-precision "picometer microscopy" is a key advantage of aberration-corrected electron microscopy for applications in materials science, where measuring the distance between a particular atom and a more distant reference atom position is an important starting point for calculating local physical properties[20].

[20] To visualize the length of a picometer, it may be helpful to recall that the Bohr radius of the hydrogen atom is 53 pm. This means that the precision of modern aberration-corrected electron microscopy is about one hundredth of the diameter of the hydrogen atom.

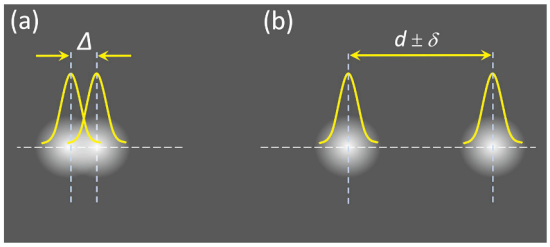

Fig. 17. Schematic illustrating the difference between (a) optical resolution (according to Rayleigh) and (b) precision. The definition of resolution Δ concerns atomic contrast figures that partially overlap [46]. Precision, on the other hand, describes the accuracy ($\pm\delta$) with which one can measure the lateral distance d between two atomic positions in the object that are far enough apart that their contrast maxima do not overlap in the image. The width of the intensity maxima depends on the optical conditions and in particular on the signal-to-noise ratio in the image. In general the parameter of precision is by more than an order of magnitude better than the optical resolution. This forms the basis of "picometer electron microscopy" in materials science.

6. Application examples

6.1. Overview

The possibility to perform investigations and high-precision measurements in atomic dimensions on a broad scale using aberration-corrected optics has led to a great variety of applications in materials science. It is beyond the scope of this review to cover them in their entirety. The examples of the application of CTEM discussed below have been selected so that each of them highlights an important aspect of such work and can thus contribute to an assessment of the method. We also note here that this section serves two purposes. On the one hand, we want to show by concrete examples how the application of the technique is implemented in practice with the aim of obtaining truly quantitative results. This requires a corresponding level of detail with respect to the procedures. On the other hand, this section should also be a guide with reference to the literature, from which the reader can see for what kind of research topics and with what results aberration-corrected CTEM has been used so far. In this case, in order to keep the scope of this review work within limits, we will keep the relevant sections as short as possible. Nevertheless, what seems inevitable for a review that has a technique as its subject, we will try to outline briefly for each case the material science problem for the non-specialists.

The first systematic atomic resolution studies using aberration-corrected transmission electron microscopy were carried out in $BaTiO_3$, $SrTiO_3$ and $YBa_2Cu_3O_7$ by Jia et al. [84,85]. Further studies concerned the reconstructed 90° tilt grain boundary in $YBa_2Cu_3O_7$ [111], of the atomic structure of dislocation cores in $SrTiO_3$, and the structure of the $Si/SrTiO_3$ interface [141]. The effect of a single dislocation in the $SrTiO_3$ substrate on the atomic structure of epitaxial $Pb(Zr_{0.2}Ti_{0.8})O_3$ and the local ferroelectric polarization was investigated in [142].

6.2. Quantitative investigations on oxygen occupancy

As briefly mentioned above, the feasibility of atomically imaging and quantitatively measuring oxygen can be considered one of the first successes of the application of aberration correction in materials science [86,87]. The following two examples illustrate the types of contributions that atomic electron microscopy of oxygen has been able to make to solving physical/chemical problems that were of interest at the time. The first example [84] concerns the high-temperature oxide superconductor $YBa_2Cu_3O_7$ (so called "1-2-3" compound). Its unit cell consists of three perovskite-type subcells (Fig. 18). As depicted in (c) two of them are Ba-centered and the central one is Y-centered. The hole-type superconductivity is parallel to the CuO_2 planes on both sides of the Y atoms. A common feature of all 1-2-3 superconducting compounds is that in order to arrive at the proper electron structure in the CuO_2 planes these have to be "doped" by withdrawing electrons [143]. In this the Cu–O chains in the Ba-centered subcells are playing an important part. It is crucial that the oxygen in these chains is ordered. This means that the center edge positions are occupied by oxygen along the crystallographic ***b***-direction, but the corresponding sites along the ***a***-axis are left vacant. The first electron microscopic proof of this was provided in the present study. Fig. 18a shows a 90° tilt boundary (black horizontal arrow) where the viewing direction is for the upper crystallite parallel to [100] and for the lower one parallel to [001]. The sample was produced by the high oxygen pressure sputtering technique [144] whose low deposition rate leads to highly perfect crystal lattices. Comparison with the structure model (insets) indicates that all atomic positions of the cations Ba (cyan), Y (yellow), and Cu (red) and of the oxygen are imaged. In the upper part of the image, clearly alternating copper and oxygen positions can be distinguished along the horizontal [010] Cu–O chains (red arrow). In (b) the same crystal is now imaged along the [010] direction, i.e. it is tilted with respect to (a) by 90° around the vertical axis. Now the [010] Cu–O chains are seen end-on. The oxygen positions in between the Cu-atom positions in the Cu–O–chain planes (red arrow) are empty. This provides direct evidence of oxygen ordering in the Cu–O–chain planes. In Figs. 18a,b also a so called "1-2-4" fault (marked by double arrowheads) occurs. In (b), the enhanced bright contrast of the [010] Cu–O chains (seen end-on) in the fault plane indicates a particularly high degree of oxygen occupancy and ordering there. A detailed study of the 90° grain boundary in $YBa_2Cu_3O_7$, in which the displacements of the atoms were also measured with picometer precision, was carried out by Houben et al. [111].

The second example concerns quantitative measurements of the *occupancy* of oxygen sites in the $\Sigma3\{111\}$ twin boundary in $BaTiO_3$

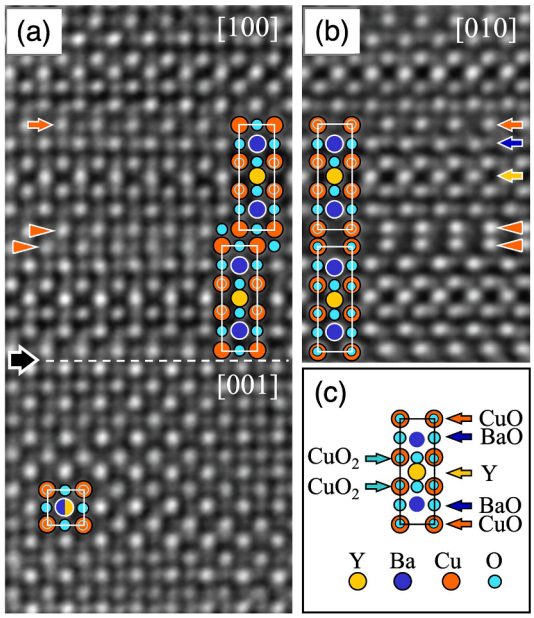

Fig. 18. (a) 90° tilt boundary (large black arrow) between a [100] and a [001] oriented crystallite in a thin film of $YBa_2Cu_3O_7$. NCSI at 200 keV. Comparison with the structure model (insets) indicates that all atomic positions of the cations Ba (blue), Y (yellow), and Cu (red) and of oxygen (cyan) are imaged (bright on a dark background). Alternating copper and oxygen positions can be distinguished along the horizontal [010] Cu-O chains (small red arrow from left). (b) The same crystallite now imaged along the [010] direction. Now the [010] Cu-O chains are seen end-on. The oxygen positions in between the Cu-atom positions in the Cu-O–chain planes (red arrow from right) are empty. This provides direct evidence of oxygen ordering in the Cu-O–chain planes. (c) Scheme of the atomic arrangement. In (a) and (b) also a "1-2-4" fault can be seen (marked by double arrowheads). (Reproduced from [84] with permission from the American Association for the Advancement of Science).

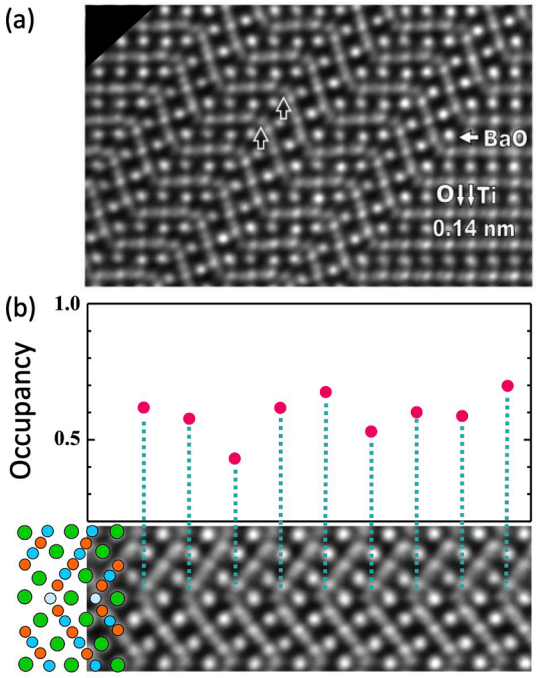

Fig. 19. (a) Parallel Σ3{111} twins in [011] oriented $BaTiO_3$. NCSI at 200 keV. Two of the boundary oxygen-atom positions are indicated by black arrows. (b) Results of quantitative contrast evaluation. The average oxygen occupancy of the boundary plane is found to be 0.68. This means that 32 % of the oxygen sites are left vacant. (Reproduced from [85] with permission from the American Association for the Advancement of Science).

(BTO) [85]. The occupancy ω is an adequate measure for the chemical composition of a particular column, where the occupancy $0 \leq \omega_A \leq 1$ of the atom species "A" adopts the value 1 if all respective atomic sites of the column are occupied by "A" atoms. The occupancy determines the scattering potential interacting with the electron wave field, and, as a consequence, the intensity distribution of electron microscopic images depends on the chemical occupation of the atom columns. This can be exploited to measure the chemical composition of a sample at atomic resolution. It is known that oxygen is relatively mobile in perovskites, especially at the high temperatures at which thin films are produced by laser ablation or sputtering. This leads to a reduction of internal mechanical stresses by oxygen-atom diffusion on the one hand and to a change in the concentration of oxygen in crystal lattice defects compared to the bulk on the other hand. An example is the $\Sigma3\{111\}$ twin boundary in BTO for which it has long been discussed that the oxygen content in the boundary is understoichiometric. Early electron energy loss spectroscopy (EELS) measurements were interpreted as an indication of this [145], but due to the low spatial resolution they were not specific enough, and (before the advent of aberration corrected optics) there was no way to image and to measure the oxygen content in the boundary. This was achieved for the first time by CTEM employing the NCSI technique in [85]. Fig. 19a shows parallel $\Sigma3\{111\}$ twins in [011] oriented BTO. Two of the boundary oxygen-atom positions are indicated by arrows. Fig. 19b shows results of quantitative contrast evaluation and image simulation. The oxygen occupancy of the boundary plane is found to be 0.68. This means that 32 % of the oxygen sites are left vacant. This has consequences for the effective Ti-atom valency changing from Ti^{4+} to Ti^{3+}. In the twin boundary, the original TiO_6 octahedra change from corner- to face-sharing, forming a Ti_2O_9 group unit. This group is a genuine element of the BTO system because it is also the basic structural element of the hexagonal high-temperature phase. A study performed by X-ray scattering on BTO in which by alloying tetravalent Ti^{4+} was substituted by trivalent Fe^{3+}, the hexagonal phase was obtained with oxygen vacancies whose concentration increased with Fe-content up to a vacancy concentration of 30 % after which the compound became unstable [146]. This indicates that the vacancy concentration found in the CTEM study corresponds to a chemically determined limit.

An et al. [147,148] applied NCSI to the atomic resolution study of a symmetric tilt twin boundary ($\Sigma13(510)/[001]$) in Y-stabilized ZrO_2. A substantial understoichiometry of oxygen was measured in the boundary plane providing an explanation for the massive grain boundary ionic transport blocking effect of grain boundaries observed in this material (e.g. [149]). As a result of the advancement of electron microscopy instrumentation technology hybrid instruments, in which the advanced optics allow the instrument to be operated in both CTEM and STEM modes, are now available in increasing numbers. These offer image as well as beam aberration correctors. This allows to perform quantitative picometer electron microscopy in CTEM mode, which can then be combined with EELS in STEM mode in the same sample area. An example is the investigation of the structural ordering in hematite nanowhiskers synthesized via thermal oxidation of iron-based substrates by Lai and Kurata [150]. By taking advantage of the high sensitivity of measuring oxygen by NCSI, the authors were able to demonstrate that the known superstructure in Fe_2O_3 nanowhiskers is due to oxygen vacancy ordering. The reason for the formation of vacancies is not an undersupply of oxygen during growth. Rather, they are incorporated in order to accommodate tensile stress. This stress is related to the fact that an Fe_3O_4 layer first forms on the Fe substrate, on which upon further oxidation the Fe_2O_3 layer grows, from which the nanowhiskers grow out. The topoaxial relation between the two forms of oxide is such that the [001] axis of Fe_2O_3 is parallel to Fe_3O_4 [111] and the two phases join at the close-packed oxygen planes. Since the oxygen-atom separation in these planes is by 2 % larger in Fe_3O_4 compared to that separation in Fe_2O_3 the former creates tensile stress in the latter. This is reduced by introduction of ordered oxygen-vacancy planes. This result is corroborated by EELS of the Fe_2O_3 nanowhisker exhibiting an energy shift of the onset of the Fe - $L_{2,3}$ edge compared to a bulk Fe_2O_3 reference sample. This is a chemical shift originating from the reduction of the iron as a result of O-vacancy formation. Additional examples of the combination of CTEM with STEM EELS are discussed in Section 7.

6.3. Dislocations

Dislocations, as crystal lattice defects that carry, e.g., crystal plasticity, accommodate crystalline misfit, and mediate phase transformations, are a classic area of solid-state physics [151,152]. The same applies to the use of electron microscopy as a tool for quantitative characterization of these defects, e.g., to determine the Burgers vector using Bragg contrast experiments [16,17]. Relatively high resolution, in the nanometer range, e.g., to image the partial dislocations in split dislocations has been achieved (in the pre-aberration-correction era) using the weak-beam technique [153,154]. In a few cases the lattice-fringe technique was also used, for which the above limitations apply, i.e., although the images look like "atomic" they do not exhibit atomic resolution in reality.

The physical and chemical properties of dislocations are decisively determined by the structure of their core. This could only be studied after the introduction of aberration-corrected atomic-resolution electron microscopy. A particular challenge is that the lattice symmetry in the core is disturbed, that high degrees of elastic distortion are present there, and that, in compounds, in general the stoichiometry and also the electronic structure are locally modified. Oxides pose a particular problem, with work published in recent years demonstrating that it is crucial that oxygen can also be imaged and measured quantitatively. The first quantitative studies of dislocation cores by aberration corrected electron microscopy are due to Tillmann et al. [110] who studied partial dislocations in GaAs as well as Lomer edge-type interface dislocations in an $In_{0.3}Ga_{0.7}As/GaAs$ (100) interface. Jia et al. [112,155] studied the core of the edge and the screw dislocation with $a(100)$ Burgers vector in $SrTiO_3$. Fig. 20a shows the result of a focal-series reconstruction on the basis of NCSI micrographs along [011] for the edge dislocation. The Burgers vector can be directly determined by performing a Burgers circuit in this image. (b) depicts the model of the dislocation, and (c) shows the result of the compositional analysis (occupancy of the individual atomic columns). With respect to Ti, the nucleus is measured to be deficient with respect to both Sr and O. Oxygen deficiency at crystal lattice defects is relatively common in oxides, and it is generally accepted that local stress fields can be reduced in this way. It is possible that charge neutrality is then subsequently restored by changing the Ti atomic valence and Sr concentration. This work also demonstrated the difficulties of such studies. The measurements show that the film thickness at the dislocation core location

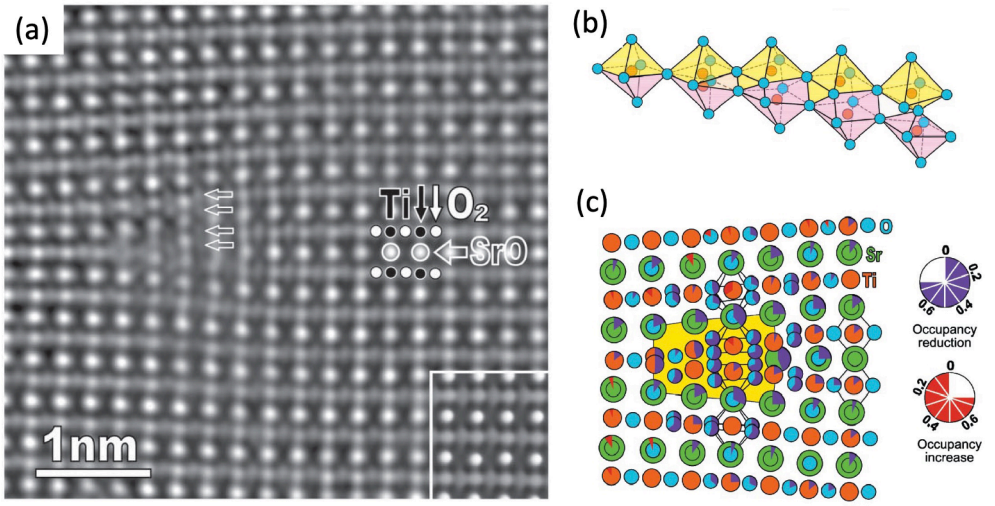

Fig. 20. (a) The core of an edge dislocation of Burgers vector a[100] in $SrTiO_3$ imaged along the [011] direction. (b) Structure model. (c) Rendering of the changes of occupancy per atomic column as determined from the atom-column intensity in the image by means of contrast calculation. (Reproduced from [112], Copyright (2005) by the American Physical Society).

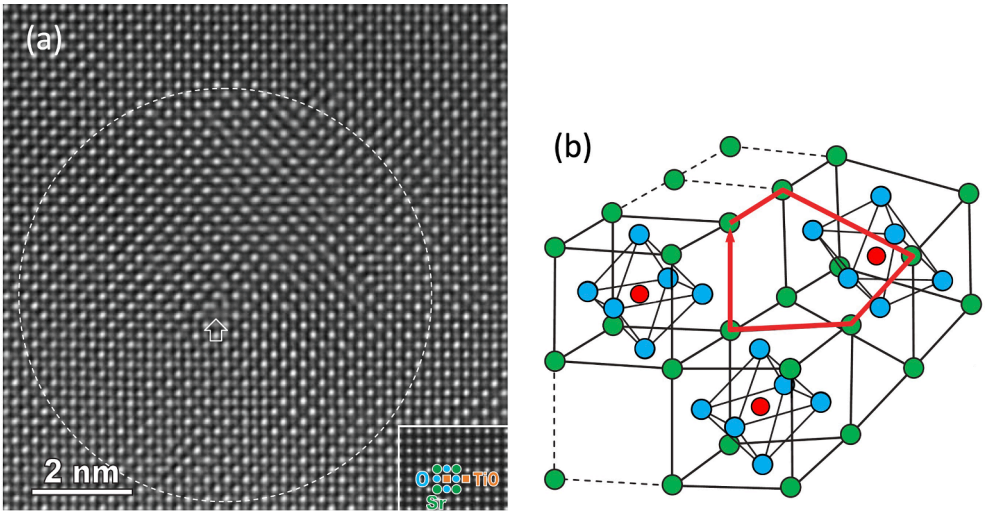

Fig. 21. (a) The core of a screw dislocation of Burgers vector a[001] in $SrTiO_3$ imaged along the [010] direction. (b) Model of the dislocation core, indicating the strong distortions of the Ti-O_6 octahedra. Sr-green; Ti-red; O-blue. (Reproduced from [155] with permission of Taylor&Francis).

is lower than in the surrounding area. This can be attributed to preferential thinning during the preparation of the transparent sample for electron microscopy. Similar observations were reported in [110]. Also in the case of the screw dislocation (Fig. 21), oxygen deficiency, as well as the presence of Sr vacancies, was observed in the dislocation core. A detailed analysis of the atomically resolved strain field revealed a general long-range tilting of the lattice. It fits the atomic column tilts expected from *Eshelby twist*. This means that the measured strain field corresponds to what is obtained when the dislocation is elastically relaxed under the influence of the image forces in the very thin sample (in this case, 3.4 nm thick) [156]. The case of electron microscopy of an (a/2) [111] screw dislocation in molybdenum has been studied in more detail earlier by Sigle using molecular-dynamics simulations [157]. This not only confirmed the results of the theoretical treatment of the modification of the strain field of dislocations in a thin plate of [156]. It also showed that the threefold splitting of the screw dislocation typical for bcc metals [158] further complicates the strain field considerably. These studies demonstrate the importance of validating electron microscopy results with reference to the fact that, because of the need to use thin foils, the sample dimension is a parameter of the Gibbs free energy of the system.

Heuer et al. [159] studied the core structure of dislocations in plastically deformed sapphire (α-Al_2O_3) employing NCSI. The structure of the dislocation core had previously been the subject of years of discussion, and it had been concluded from an electron microscopy study employing STEM [160] that the dislocation core was electrically charged, which would have significant consequences for the basal slip of the dislocations. In the present study the ability of the NCSI technique to discriminate oxygen columns

from aluminum columns and, beyond that, to *measure* the occupancy of the individual atomic columns by means of quantitative image simulation, permitted to derive from the experimental observations a detailed atomic model of the dislocation core. The result was that the partial dislocations are Al-terminated, with electrical neutrality being achieved because half of the Al columns are missing. These partials also undergo core spreading, which results in random occupancy of both tetrahedrally and octahedrally coordinated sites, though Al in tetrahedral coordination never occurs in a perfect crystal.

Zhang et al. [161] reported on an investigation of the slip process of dislocations in the $C14$ Cr_2Nb Laves phase. The structure of the dislocation core could be solved on the atomic level by means of NCSI employing the focal-series reconstruction technique. First-principles calculations revealed that the observed core structure is generated in a novel undulating slip mechanism, where the moving dislocations jump between different slip planes. The authors found that the dislocation cores exhibit a complex strain field, which they investigated by an atom-by-atom lattice distortion analysis. This, besides the possible effect of thin-foil image forces, may indicate a more complex dissociation of dislocations in the material than could be treated in their density-functional theory calculations.

6.4. Ferroelectric domains and domain walls

The nature of domains and domain walls in ferroelectrics has been studied theoretically and experimentally for a long time. A detailed overview, also under the aspect of application in data storage devices based on thin films, is given by Catalan et al. [162]. Since oxygen could not be imaged directly in classical electron microscopy without aberration correction, atomic-level studies in ferroelectric oxides had to wait until the arrival of aberration-corrected electron microscopy. The first study by electron microscopy of ferroelectrics, ferroelectric domains, and domain walls at atomic resolution was carried out by Jia et al. [163]. Since the NCSI technique can be used to directly image and measure all atoms of a ferroelectric material, including oxygen, the polarization state can be directly determined at the level of individual lattice unit cells.

The perovskitic compound $Pb(Zr_{0.2}Ti_{0.8})O_3$ (PZT) is a widely used technical ferroelectric, e.g., for fabricating high-performance piezoelectric actuators or in the form of thin films in ferroelectric random access memories. Domain walls, in which the state of polarization changes from one direction to another occur as a remnant of thin-film production either resulting from non-equilibrium dynamic intermediate conditions or from the need to reduce depolarization fields. The atomic structure of 180° inversion domain walls in PZT was investigated in [163]. Fig. 22 displays a NCSI electron micrograph. The schematic drawing in Fig. 23 serves to facilitate understanding of this figure and the following ones. Ti and Zr are normally disordered on the central B sites of the perovskite unit cell, which is cubic in the paraelectric state above the Curie temperature. Close inspection of the image shows that there are two polarization domains. As demonstrated by the magnification in the left-hand inset oxygen sites are shifted towards the upper horizontal PbO atom row, and they are no longer collinear with the Ti/Zr atom row. As a result, inside a given unit cell, the positive and the negative charge centers (which coincide in the paraelectric state) are shifted with respect to each other, the material is polarized. The polarization vector $\boldsymbol{p}$ points downward. In the inset at the lower right the shifts are in the opposite direction and, as a consequence, the polarization vector is inverted. In between we have a 180° inversion domain wall (dotted line). The oblique parts of the wall are made up of transversal segments and very short longitudinal segments. They are essentially uncharged since the electric fields characterized by the polarization vectors of the adjoining boundary segments cancel each other in pairs. In the horizontal domain-wall segments, on the other hand, the polarization vectors are, across the wall, meeting head-to-head. As a result the electric fields do not cancel and the boundary is charged. As shown in Fig. 24a the transversal walls are only little more than a single projected unit cell thick. Although the third dimension along the line of sight is not accessible, thus a possible chiral contribution to the structure of the domain wall cannot be ruled out, the structure fits the results of theoretical studies [164]. In ferroelectrics, spontaneous electrostriction, the coupling between ferroelectric polarization and lattice strain, causes a significant amount of energy to be expended in rotating the polarization out of the directions of the lattice allowed by the symmetry. The result is that the 180° domain walls are of the Ising type [164], that is, the vectors of polarization lie in the plane of the domain wall and the modulus (cf. Fig. 24b) decreases as the wall is approached and passes through the value 0. Fig. 25a shows for a longitudinal domain wall the results of the measurements of the atomic shifts of the O and Zr/Ti atoms out of their symmetry positions. This wall is rather extended, about 10 lattice constants. From these measurements it can be inferred that this kind of domain wall reduces the field energy by increasing its width substantially over that of the charge-neutral transversal wall. Fig. 25b shows the value of the macroscopic spontaneous polarization P_S calculated from the measured atomic shifts employing calculated values for the effective charges of the ions [165].

As in ferromagnetic layered systems, there are a variety of topological configurations of the arrangement or the interaction of polarization domain walls in ferroelectrics. Following the results of theoretical work [166,167] Jia et al. [168] investigated the interfaces between an extended PZT layer containing 180° domain walls and a substrate layer and a capping layer, respectively, of STO. Fig. 26a shows a false-color representation of an approximately perpendicular 180° inversion domain wall (yellow dotted line). It extends from the capping layer (just above the upper edge of the image) to the substrate layer (just below the lower edge of the image). The arrows show the direction of the displacement vector of the Ti/Zr atoms with respect to the center of the oxygen octahedra. The modulus shows the length of the displacement (scale bottom left). This image therefore represents a map of ferroelectric polarization. It shows a flux-closure domain (bounded by the blue dotted line) across which, via continuous dipole rotation, the flux rotates from the right to the left domain by twice 90°. Such flux-closure structures, which are expected to minimize the energy of the stray field, as in the analogous case of closure domains in ferromagnetics, had been predicted theoretically but never were found experimentally before. Fig. 26b shows the strength of the ferroelectric polarization via the displacement parameter δ_O. It can be seen that at the bottom, just above the substrate layer (except for the last atomic layer, directly at the interface), the polarization largely retains its bulk value. This suggests that the presence of the flux-closure region at the lower STO-PZT interface reduces the *depolarization field* accordingly. On the

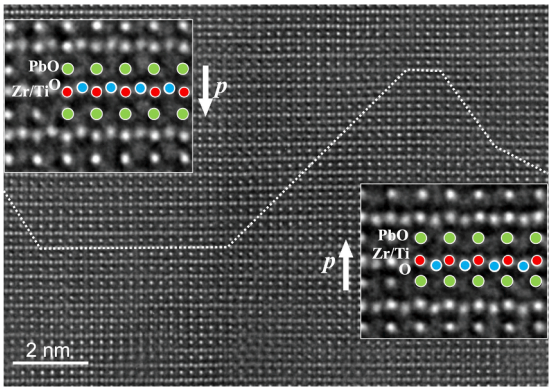

Fig. 22. $Pb(Zr_{0.2}Ti_{0.8})O_3$ (PZT) imaged along the [110] direction. Compare with Fig. 23. The magnification (inset) on the left-hand side shows that oxygen (blue symbols) is shifted upward towards the respective PbO atom row (green symbols). Therefore the oxygen-atom row is horizontally no longer co-linear with the Ti/Zr atom row (red symbols). This indicates that the material is ferroelectrically polarized. The polarization vector ***p*** is pointing downward. The inset on the right-hand side shows opposite atomic shifts. The direction of the polarization vector there is upward. The 180° inversion domain wall is shown as dotted line. (Reproduced from [163] with permission of Springer Nature).

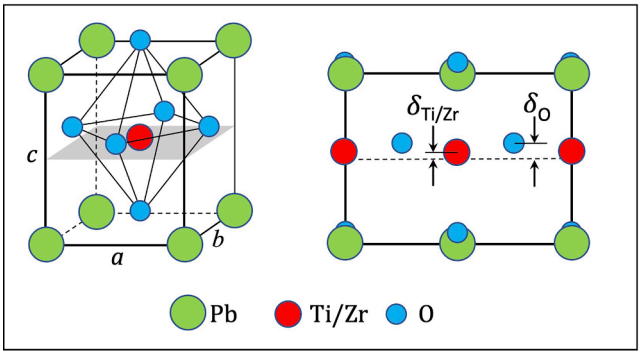

Fig. 23. Schematic of the $Pb(Zr_{0.2}Ti_{0.8})O_3$ (PZT) structure. Left: perspective view of the unit cell in the ferroelectric state (*a, b* and *c* denote the unit cell dimension along the corresponding crystallographic axes, ***a, b*** and ***c***, respectively). The gray-shaded plane indicates the position of the center of the unit cell at c/2 to visualize that the O atoms are displaced upward. Right: [110] projection. The unit cell is tetragonally distorted along the ***c*** axis. The oxygen-atom octahedron is shifted upward parallel to ***c*** by δ_O. The titanium/zirconium atom positions are shifted by $\delta_{Ti/Zr}$. The polarization vector is antiparallel to ***c***.

other hand, the depolarization field at the upper interface is so strong that the polarization decays. The decay starts about six unit cells away from the interface, ultimately reaching a value of zero.

Although, as described above, the ferroelectric domain walls are generally of the Ising type, there are rare cases where a Néel type wall is energetically more favorable. In this case the vector of polarization maintains a finite value and it rotates in the plane perpendicular to the wall. Again, this was predicted by theory, but evidence for it was only recently found by Wei et al. [169] employing NCSI for an investigation of Zr-rich PTO where nanometer-scale monoclinic order coexists with tetragonal order. Wei et al. [170] took a theoretical study based on a Landau theory of phase transformations as the starting point for an investigation in $PbZrO_3$ carried out by means of NCSI, in which they were able to demonstrate that translational antiphase boundaries in this non-ferroelectric compound are ferroelectric.

6.5. *Structure and chemical composition of thin-film heterostructures*

The report [171] of a high-mobility electron gas at the heterointerface between the two nominally insulating perovskites $LaAlO_3$ (LAO) and $SrTiO_3$ (STO) stimulated intensive research efforts concerning the physical origin of this phenomenon. We focus our selection of LAO/STO system-related electron microscopy works on those that have used CTEM for structural studies. The first paper uses this structurally very complex case to demonstrate the fineness of the structural details that can be determined with quantitative NCSI. The second example shows how the high chemical detection sensitivity can be used to measure the real stoichiometric details of a heterointerface at atomic resolution.

Jia et al. [172] investigated the atomically resolved structure of an LAO layer 2.5 nm (6 unit-cell parameters) thick between two STO layers. The layer system was prepared at 800 °C using the high oxygen pressure sputtering technique [144]. A cross-section of the

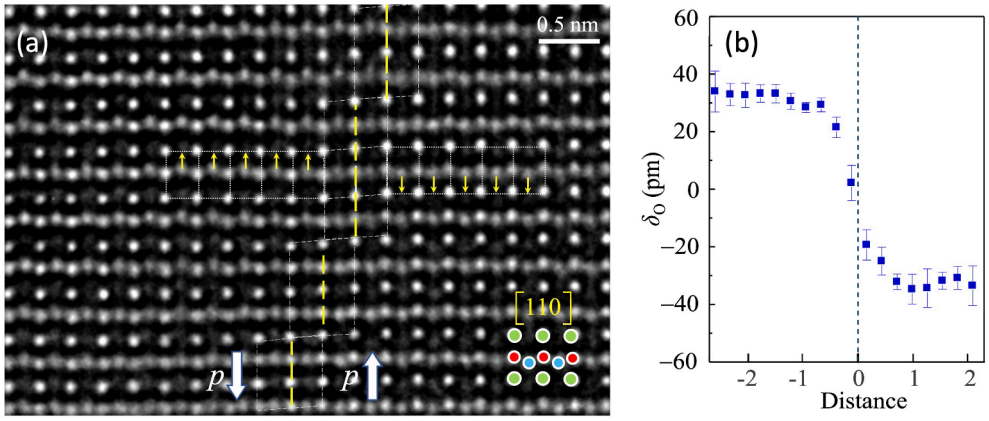

Fig. 24. (a) A 180° inversion domain-wall segment of mixed type in PZT imaged edge-on along the [110] direction. The vertical yellow dashed line marks the central plane of the wall. The arrows ***p*** indicate the opposite polarization directions across the wall. The white dotted lines trace projected half unit cells on either side of the domain wall. As indicated by the shift of the oxygen atoms (small yellow arrows), 'up' on the left and 'down' on the right-hand side of the central plane, and as indicated by the measurements of the shift δ_O of the oxygen atoms in (b) the width of the wall is a single projected unit cell (lower right corner in (a)) wide. (Reproduced from [163] with permission of Springer Nature).

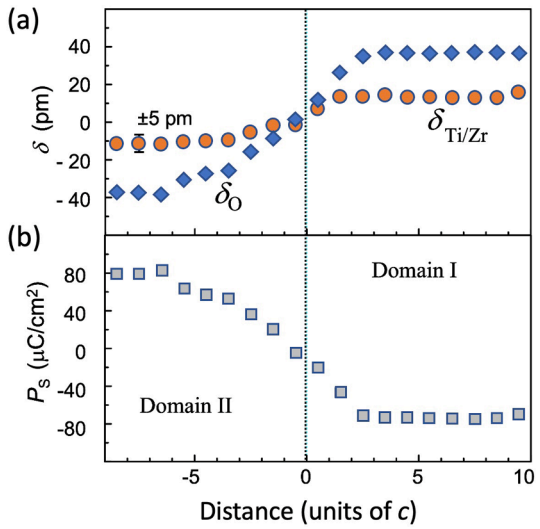

Fig. 25. (a) Atom shifts in the longitudinal inversion domain wall measured on the atomic sites. The parameter $\delta_{Ti/Zr}$ (red symbols) denotes the upward shift of the Ti/Zr atom positions towards PbO as a function of distance (in units of the *c* lattice parameter) from the domain wall center (at $c = 0$). δ_O denotes the corresponding O-atom shift. The Gaussian regression analysis indicates a precision of better than 5 pm (for a 95 % confidence level). The domain wall width amounting to 10 unit cell distances is much wider than that of the transversal wall sections. (b) The macroscopic spontaneous polarization P_S calculated on the basis of the measurements of the individual atomic shifts. (Reproduced from [163] with permission of Springer Nature).

heterostructure, imaged along the crystallographic [110] direction is shown in Fig. 27a. As indicated in (b) STO has cubic perovskite structure ($a = 0.3905$ nm). LAO has rhombohedral structure (with respect to STO the lattice mismatch is − 2.9 %). This structure forms during cooling from a high-temperature cubic structure by rotation of the oxygen octahedra around the <111> axis. In the [110] projection (c) this can be recognized by an alternating up and down shift, respectively, of the oxygen atoms which can be directly recognized in the center of (a). LAO is generally described in terms of a pseudocubic structure with a lattice parameter of $a_p = 0.3792$ nm. In the following pseudocubic indices will be used as indicated by the subscript "p." Looking at the layering of the atoms along the crystallographic *c*-axis, in STO each layer is neutral by itself, while in LAO the layers are alternately positively or negatively charged. Thus, the unraveling of the atomic structure of the STO/LAO interface poses a challenging problem because it is expected that the effects of symmetry breaking due to the rotation of the oxygen atom octahedra and the elastic misfit of the lattices together with the polar nature of the lattice planes in LAO will overlap in a complex manner when the two structures meet. Fig. 28 shows the results of the measurements of the atomic positions in the images. (a) shows the values of the *c* and the c_p lattice parameter parallel to [001], and $[001]_p$, respectively. We see that there is a continuous transition at the two interfaces. (b) shows the value of the parameter of the

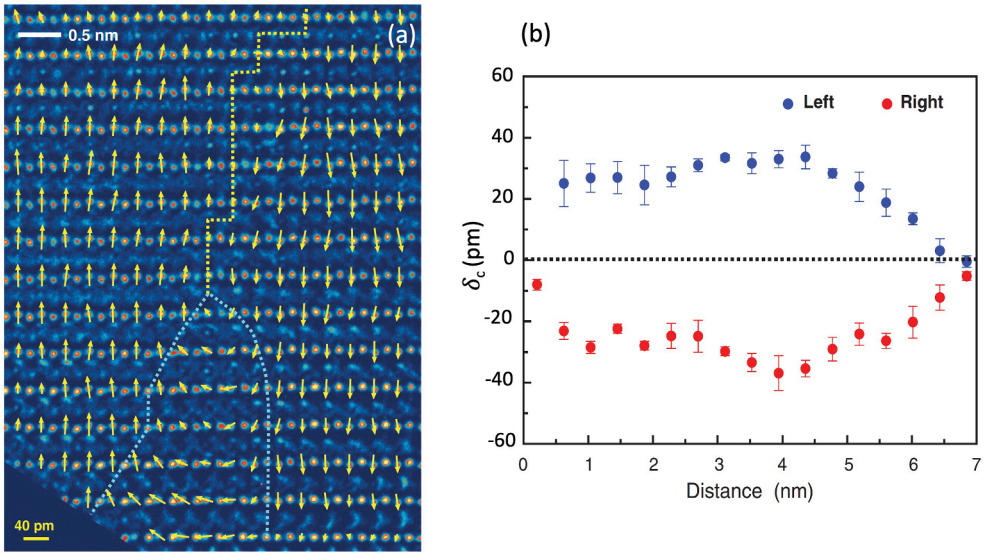

Fig. 26. (a) False-color representation of an approximately perpendicular 180° inversion domain wall (yellow dotted line) in PZT. Viewing direction [110]. The wall extends from the capping layer (STO, just above the upper edge of the image) to the substrate layer (STO, just below the lower edge of the image). The arrows show the direction of the displacement vector of the Zr/Ti atoms with respect to the center of the oxygen octahedra. The modulus indicates the length of the displacement. The scale, bottom left, of 40 pm corresponds to a macroscopic polarization of 108 μCcm^{-1}. This map of ferroelectric polarization shows a flux-closure domain (bounded by the blue dotted line) across which, via continuous dipole rotation, the flux rotates from the right to the left domain by twice 90°. (b) depicts the shift parameter δ_c, that is the displacement of the Ti/Zr atoms with respect to the center of the oxygen octahedra (in the paraelectric state this would be the position of the Ti/Zr atoms, cf. Fig. 23) along the vertical [001] direction as a function of distance from the lower interface. The blue symbols denote the upward displacements in the left domain; the red symbols indicate the downward displacements in the right domain. At the lower interface, due to the low depolarization field, the values change from the bulk value to a value close to zero within the distance of a single unit cell. At the upper interface, due to strong depolarization, the shift parameter starts to decrease already six unit cells away from the interface, reaching a value of zero there. (Reproduced from [168] with permission from the American Association for the Advancement of Science).

vertical displacement of the oxygen atoms (out of the respective horizontal Al and Ti atom row) δ_O. As expected, in LAO, due to the rotation of the oxygen octahedra, the direction of the displacement is alternately upward (red symbols) and downward (blue symbols). Surprisingly, this sequence of upward/downward shifting of oxygen atom positions is also observed on the STO side of the interfaces. This means that the presence of LAO enforces an oxygen-octahedron rotation also in the STO, over some lattice constants away from the interface. (c) displays the measured values δ_c of the shifts of the *centers* of the oxygen octahedra out of the Al plane in LAO (center) and out of the Ti plane in the STO layers. No shift is, as expected, observed in LAO. On the other hand, an upward shift of 3.5 pm is observed in the lower and a downward shift by about 5 pm in the upper STO layer, i.e., always toward the LAO layer, over a distance of about 5 lattice parameters. This indicates polarization-dipole formation with the polarization vector pointing away from the LAO layer. The observations led to an atomistic model of the STO/LAO interface in which the mechanical and electronic contributions to the interfacial energy are suitably accounted for, and which describes the observations very well within the framework of the image calculations. The model is rather robust with respect to a possible mixing or interdiffusion of the constituents during layer deposition. An extreme case of such an unstoichiometry of the interface is treated in the following paragraph, which at the same time demonstrates that quantitative CTEM is also a highly sensitive measurement method with respect to local, atomically resolved chemical composition.

That quantitative CTEM on the basis of NCSI is capable of determining the concentration of the constituent elements at atomic resolution with high accuracy is made possible by the fact that we can today calculate the atomically resolved intensity distribution in the image at absolute contrast level. In the following, it will be shown how such a quantitative investigation is carried out in practice [173]. It is the measurement of a nominally single unit cell thick layer of $LaAlO_3$ sandwiched between a $SrTiO_3$ substrate and a $SrTiO_3$ capping layer. The heterostructure was epitaxially grown by laser ablation deposition at 700 °C.

Fig. 29a displays the experimental image of the cross-sectional preparation of the heterostructure. The nominal position of the LaO atom layer is indicated by a horizontal arrow. All atom positions appear bright on a dark background. For quantification the image was recorded as a primary data file, $\widehat{I}(x,y)$, where $\widehat{I}$ denotes the intensity value per pixel at the position x, y. The image calculation and the iterative matching of the calculated to the experimental data is then carried out in two major steps. Step 1 comprises the determination of the instrumental image acquisition conditions and the sample parameters. This is the prerequisite for step 2, the actual measurement of the atomic positions and the atomically resolved chemical composition. Since we are dealing with a heterostructure in the present case, where we know the structure of the substrate and the capping layers, we can use the STO regions further away from the interface as a template for calibration. This means that in these regions in the iterative computer-based fit of the calculated to the experimental intensity data only the optical parameters C_1, C_S, A_1, A_2, B_2, and A_3, and the sample parameters thickness and tilting angle (including

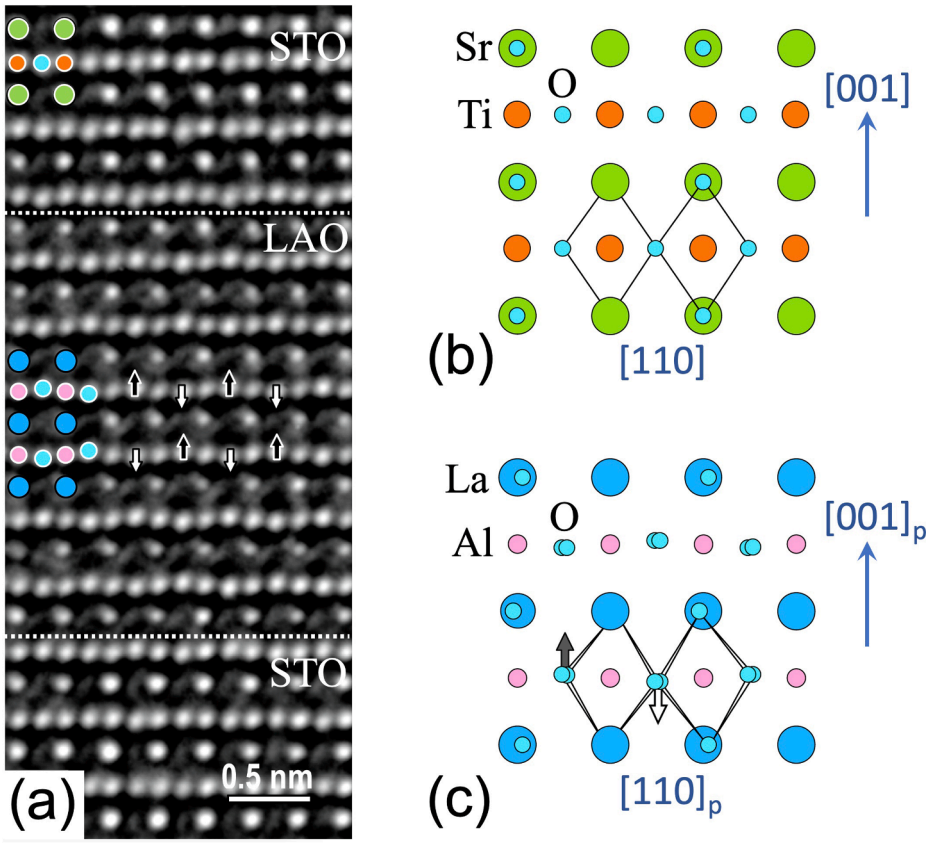

Fig. 27. (a) Image under NCSI conditions of an epitaxial STO/LAO/STO heterostructure. In LAO the projected shift of the oxygen atoms out of the respective Al-atom rows as a result of oxygen octahedron rotation is clearly visible (arrows). (b) Schematic of STO in [110] projection, (c) schematic of rhombohedral LAO in pseudocubic $[110]_p$ projection with oxygen-octahedron rotation-induced shifts indicated. (Reproduced from [172], Copyright (2009) by the American Physical Society).

the orientation of the tilt axis) are taken as free parameters. Iterative solution of the Schrödinger equation yields the exit plane wave function ψ_e. This specimen-related part is then followed by the optical part. In the calculation of the wave function in the image plane ψ_i the contrast transfer has to be considered.

Since in this investigation the goal was to achieve a fit of the calculated to the measured intensity distribution at absolute values of image contrast the possibility of losing electrons in the imaging process was investigated in [173]. In fact the fraction of the electron current entering the sample at the top that contributes to the image formation at the bottom has never been systematically investigated. There are a number of possible causes for losses, e.g. by surface backscattering at the entrance surface or by elastic and inelastic scattering into high angles outside the effective aperture of the beam path. In fact, it is not easy to determine this effective aperture or to answer the question whether this affects the spectrum of object frequencies from which the spectrum of the image frequencies are derived. To date this question can only be answered experimentally. For this the electron beam is focused to a diameter (a few tens of nanometers) ensuring that the total electron current is registered by the camera. Then (without moving the sample laterally) the total current registered by the camera is measured once when the beam is in the vacuum range outside the sample and once when the beam is on the sample penetrating it. It is found that in the latter case the current is always reduced. In the present case it was found to be about 10 % lower. Since there are no systematic studies of this phenomenon so far, a feasible way to consider these losses phenomenologically in the image simulations is to assume a complex scattering potential whose imaginary part V'' makes up a certain percentage of the real part V', i.e. following the classical ansatz of Hashimoto et al. [174], $V_g = V_g' + iV_g''$. Detailed investigations showed that the losses are well described by $V_g'' = \zeta V_g'$ with $\zeta = 0.085$. Before a quantitative comparison between the calculated and the experimental intensity distribution, at absolute values of image contrast, can be carried out two corrections have to be implemented to the image spatial frequencies signal. The first concerns the modulation transfer function of the camera (see above). The second concerns a Gaussian blurring operation to account for image spread (see above). This must also be determined in the computer fit (in the present case of the images of the known calibration structure STO). The result was a rms value of $\sigma = 20$ pm. For step 2 the optical as well as the specimen parameters derived in step 1 are adopted and left constant during the iteration. The only fitting parameters are now the atom positions and the occupation numbers of the atom columns in the interface area. The calculated intensity distribution resulting from the quantitative computer fit is displayed in Fig. 29b at the same absolute value of image contrast. A quantitative

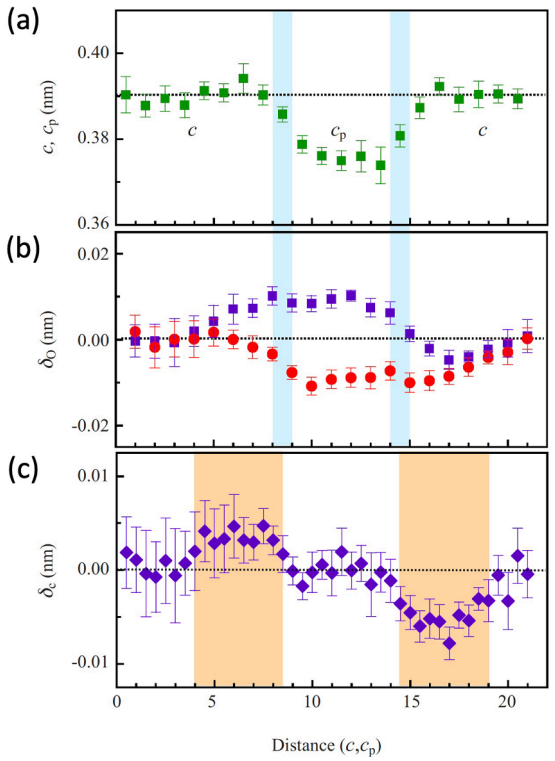

Fig. 28. (a) *c*-lattice parameter in STO and c_p-lattice parameter in LAO as function of distance (in units of *c* and c_p, respectively; the subscript "p" refers to the pseudocubic lattice) from a reference plane in the lower STO layer. The vertical shaded lines mark the interfaces. (b) The value of the shift parameter δ_O of the oxygen atoms as a function of distance from the reference plane. Squares denote upward shifts and circles denote downward shifts. (c) The value of the shift parameter δ_c of the center of the oxygen octahedra with respect to the appertaining cations. The error bars indicate a 95% statistical confidence level of a Gaussian regression analysis. (Reproduced from [172], Copyright (2009) by the American Physical Society).

comparison of experimental und calculated intensity values is given in Fig. 30. The excellent reproduction of the experimental data by image simulation is obvious.

The results for the atom positions are displayed in Fig. 31a. While the relative positions of the cations strontium and titanium, on the one hand, and lanthanum and aluminum, on the other hand, are essentially unchanged compared to a simple geometrical (unrelaxed) model, a shift of the oxygen atoms into the direction of the central (nominal) LaO plane by 5 pm occurs. This is in direct agreement with the corresponding result of the measurement of the LAO/STO heterostructure described above. The results for the atomically resolved chemical composition are depicted in Fig. 31b. A mixed occupancy of the perovskite A-sites by La and Sr atoms is evident and the width of the disturbed regions is about 4 atomic distances in the capping layer and 2 in the substrate layer, respectively. In the nominal LaO plane, only 55 % of the A-sites are occupied by La atoms and the remaining 45 % by Sr atoms. In the perovskite BO_2 atomic plane directly above the LaO plane, which is nominally expected to be an AlO_2 plane, only 35 % of the lattice sites are occupied by Al atoms, and the rest of the sites are occupied by Ti atoms. In the plane below the LaO plane, which (prior to LAO deposition) was the TiO_2 terminating plane of the STO substrate, 30 % of the Ti atoms are replaced by Al atoms. The measurements also indicate an oxygen understoichiometry in the interface of about 10 %. This and the previous investigation show the high precision with which CTEM of heterostructures can be carried out with respect to the measurement of the real atomic positions and their occupation with different atomic species. Not only can the results of the epitaxy be validated in this way, the measurement results can also provide an excellent starting point for *ab-initio* calculations.

As we have shown in the present and the previous section, the rotation and deformation of the B-O_6 octahedra as well as changes in the stoichiometry near the interface in perovskite heterostructures are variables that critically affect the Gibbs free energy of the system. This problem was addressed by Jia et al. [175] and also in a commentary article on it by Muralt [176]. Kinyanjui et al. [177] investigated by X-ray diffraction, STEM and NCSI CTEM the structure of epitaxial $LaNiO_3/LaAlO_3$ superlattices grown on a compressive-strain inducing $LaSrAlO_4$ (001) substrate. They found that the $(Ni/Al)O_6$ octahedron rotation angle perpendicular to the superlattice plane is enhanced, and the one parallel to the plane is reduced with respect to the corresponding bulk values. Qi et al. [178,179] studied thick $LaNiO_3/LaGaO_3$ superlattices on STO (001) by NCSI and found a reduced rotation of the NiO_3 and the GaO_3 octahedra as a result of the interaction with the STO substrate layer at the lower end of the heterostructure while at the upper end the rotations relax to the bulk values in $LaNiO_3$ and $LaGaO_3$, respectively.

The growth of strained epitaxial superlattices has its limit where the misfit between the substrate and the superlattice and in the

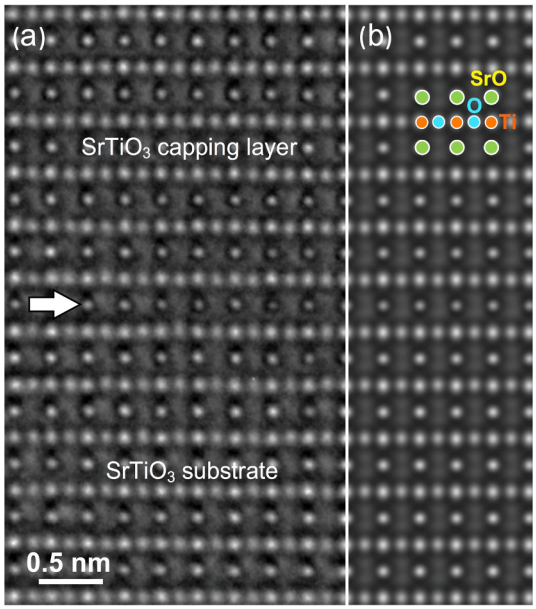

Fig. 29. (a) Experimental image of a nominally single unit cell thick layer of LAO embedded in STO recorded at 300 keV along the [011] direction (FEI Titan® 80-300; GATAN 2 k × 2 k UltraScan® 1000). The horizontal arrow denotes the nominal position of the LaO plane. (b) Simulated image with the best match to the experimental image. Both images are displayed at the same absolute value of image contrast. (Reproduced from [173] with permission from Cambridge University Press).

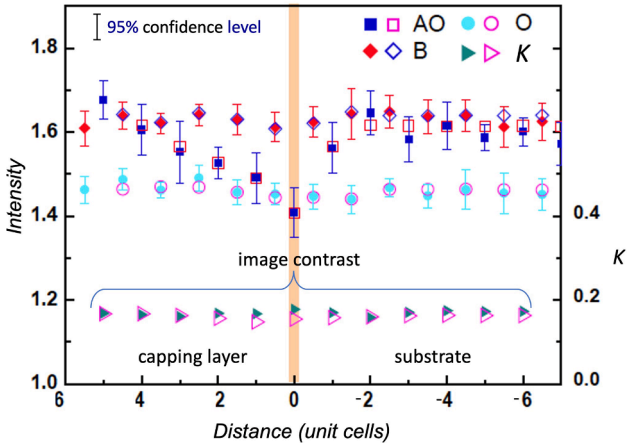

Fig. 30. Comparison of the data derived directly from the experimental image (solid symbols with error bars) with the corresponding values derived from the best fitting simulated image (open symbols) for the peak intensity at atomic positions (A: Sr, La; B: Ti, Al; O: O) together with the absolute value of the image contrast (denoted in the figure by *K*) as a function of distance from the LaO plane (expressed in number of unit cells). The position of the nominally single LaO atomic plane is marked by a vertical thick line. This figure, together with the previous one, demonstrates how quantitative state-of-the-art image calculations can be. The agreement between experimentally measured intensities and the calculated ones is excellent. This provides the basis of the quantitative evaluation in terms of shifts and occupancies in the following figure. (Reproduced from [173] with permission from Cambridge University Press).

individual layers inside the heterostructure, respectively, is too large. Then misfit dislocations form during the epitaxial growth. Qi et al. [180] studied the growth of compressive-strained $PrNiO_3$ (PNO)/$PrAlO_3$ (PAO) superlattices consisting of 8 repetitions of a 4 unit cells of PNO and 4 unit cells of PAO bilayer grown on a $LaSrAlO_4$ substrate. By means of atomic-resolution NCSI and quantitative image simulation (including the position of the oxygen atoms), they were able to solve the complex microstructure resulting from the effect of the orthorhombic, rhombohedral and tetragonal lattice structures and the large misfit. Due to the high level of biaxial compressive strain a novel defect structure was formed consisting of Shockley partial dislocations, stacking faults and areas of Ruddlesden-Popper faults.

Epitaxial thin films of ferroelectric oxides, such as $Pb(Zr,Ti)O_3$ and $BaTiO_3$ and, more recently, HfO_2 [181] have attracted

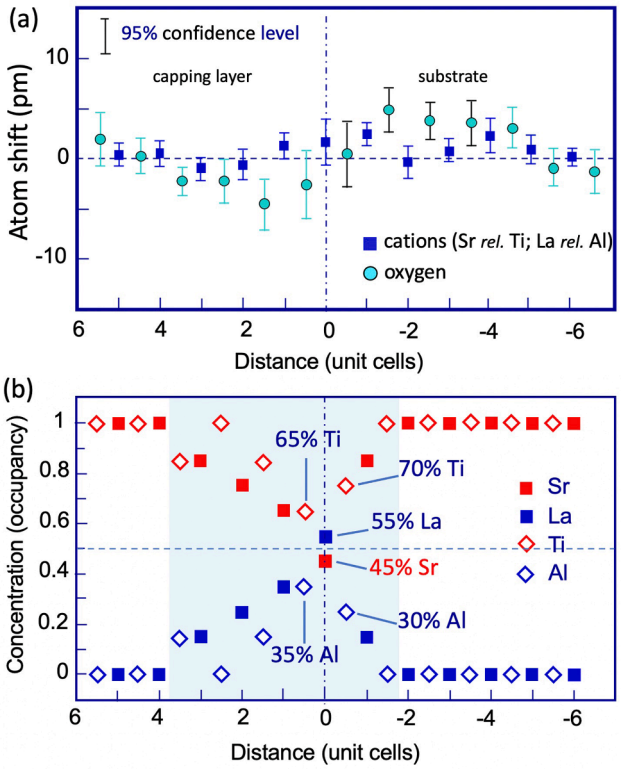

Fig. 31. (a) Shift of the relative positions of the cations Sr,Ti and La,Al and of O compared to a simple geometrical (unrelaxed) model. While the cation positions remain unchanged a shift of the O atoms into the direction of the central (nominal) LaO plane of 5 pm occurs. This indicates an interface dipole formation. (b) Results for the atomically resolved chemical composition (occupancy). A mixed occupancy of the perovskite A-sites by La and Sr atoms is evident and the width of the disturbed regions is about 4 atomic distances in the capping layer and 2 in the substrate layer, respectively. (Reproduced from [173] with permission from Cambridge University Press).

considerable attention with respect to potential applications in nanoelectronic high-density non-volatile memory devices. The magnitude and stability of the switchable ferroelectric polarization are the central figures of merit for such devices. How the polarization scales with reduced thickness, particularly when the film thickness becomes smaller than typically 200 nm, is an intensely debated topic. This so-called "size effect" represents one of the most intriguing phenomena in the area of thin-film ferroelectrics [182]. In an early paper on the polarization behavior of an 8 nm thick layer of $Pb(Zr_{0.2}Ti_{0.8})O_3$ on $SrRuO_3$ (SRO) employing classical uncorrected CTEM Jia et al. [175] reported on a substantial reduction of the maximum value of the polarization as deduced from the change of the lattice parameter (in the uncorrected instrument the oxygen atoms could not be seen). This problem was revisited by Mi et al. [183] who, using aberration-corrected electron microscopy, determined the polarization on the atomic level by measuring the displacement δ_O of the oxygen atoms with respect to the position of the Ti/Zr atom rows. The results are depicted in Fig. 32. The data at the top (a) refer to the measurement of the (out of plane) *c*-lattice parameter as a measure for the polarization-induced tetragonality. (b) shows the modulus if the shift vector $\delta_{Ti/Zr\text{-}O}$, and (c) depicts the values of the macroscopic spontaneous polarization derived from the oxygen-atom vs. Ti/Zr-O atom shifts [175,184]. Over a distance of about three unit cells at the interface the value of the polarization is reduced. This reduction was interpreted as to result from a depolarization field present since SRO obviously could not supply enough free charge for complete screening.

Lu et al. carried out a detailed investigation employing NCSI, HAADF STEM, ELNES and electron holography on the $Al_2O_3/SrTiO_3$ interface [185]. The results provide evidence for the presence of a two-dimensional electron gas in the interface between the two compounds. This is associated with a partial reduction of the Ti oxidation state in the $SrTiO_3$ layer from Ti^{4+} to Ti^{3+} within a distance of 1 to 2 unit cells at the interface, to which oxygen vacancies also contribute.

6.6. Crystal lattices at surfaces and in nanoparticles

There are a number of studies that show that quantitative CTEM can be used to study and measure displacements of atoms in metals and compounds near the surfaces. In one group of studies of this type, a cross-sectional preparation is made so that, with the imaging direction perpendicular to the surface of interest, one can see the near-surface atomic arrangement "from the side". Since a sample sufficiently thin for electron transmission also has two surfaces along the direction of view, it is necessary to check in each individual case to what extent the measurement results are influenced by the specific sample geometry and the associated atom relaxations. A

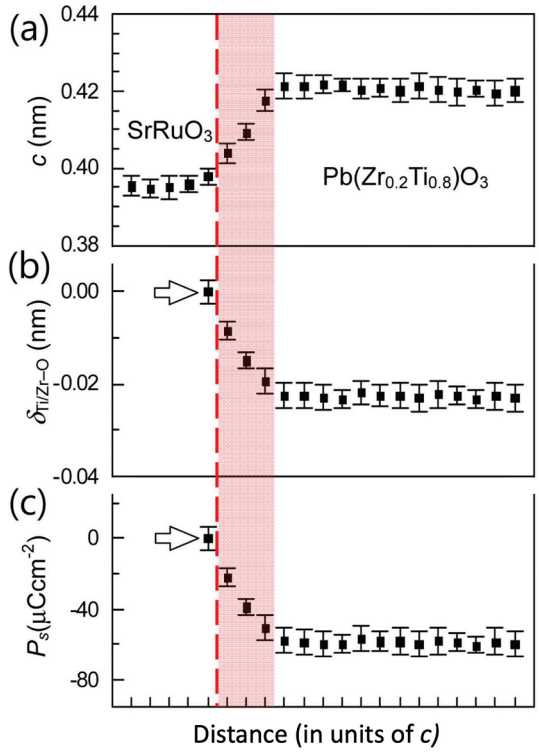

Fig. 32. The interface between $SrRuO_3$ (SRO) and $PbZr_{0.2}Ti_{0.8}O_3$ (PZT). (a) The variation of the out-of-plane lattice parameter *c* across the PZT/SRO interface. (b) The measured value of the shift parameter $\delta_{Ti/Zr-O}$ of the displacement of the O-atoms relative to the neighboring Ti/Zr-atoms in PZT. (c) The calculated value of P_S of the polarization. The interface is indicated by a vertical red line. The shaded region shows the deviation with respect to the bulk value in PZT. (Reproduced from [183] with permission of John Wiley and Sons).

related field is the investigation of nanoparticles. In this case, no special preparation is necessary due to the smallness of the particles to be studied. And if catalytically active particles are studied, atomic electron microscopy can be used to directly image the special surface structure with which the catalytic effect is associated. From a methodological point of view, it is important to point out that the study of atomic structures at edges in classical uncorrected electron microscopes has been particularly hampered by *contrast delocalization*. Not only do the atomic images overlap in the bulk, as described above, so that quantitative measurements are not possible, but - due to the same phenomenon - beyond the sample edge (in the vacuum area) pseudo images of atoms are created, which have no reality. This limitation is absent in the aberration-corrected electron microscope, making it possible for the first time to perform truly atomic-resolution studies at edges and of nanoparticles [186–188].

Pohl et al. [189] studied FePt, CuAu and Au icosahedral nanoparticles prepared by inert gas condensation and thermally equilibrated through in-flight optical annealing. High-precision atom-separation measurements as a function of the distance from the particle surface by aberration-corrected CTEM revealed that the crystal lattice is significantly expanded near the surface. These experimental findings were corroborated by molecular statics simulations that show that this near-surface strain originates from both intrinsic strain due to the atomic stacking in the icosahedral structure and a partial segregation of the larger of the two alloy constituents to the particle surface. From a methodological point of view, it is important to note that the authors derived the model structures needed for the contrast simulation to interpret the images from *ab-initio* and molecular statics simulations. Based on the relaxed atomic order in the cluster, the simulated images were then calculated and fitted to the observed contrast. This is shown in Fig. 33, along with measurements of the distances between the individual layered surface atomic positions of the {111} icosahedral surfaces. The excellent agreement between the calculated and experimental images is demonstrated in Fig. 34, where the bending of the atomic rows at the edge of an FePt nanocluster can be seen very clearly.

Bieniek et al. [190] studied the near-surface oxidation-induced lattice relaxation and compositional changes of FeNi nano-particles. The particles were synthesized in vacuum and deposited on Cu-grids covered with a transparent C-film. Using a sophisticated transfer system, the grids could be transferred into the microscope without exposing the particles to ambient air. This allowed to perform aberration-corrected CTEM at atomic resolution in unoxidized and in oxidized particles (exposed to air before insertion into the microscope), respectively. Independent of the oxidation, the surface-near metal lattice was found to be expanded by up to 3 %. Molecular dynamics simulations in combination with electron microscopic contrast simulations were conducted to investigate the effect of an Fe enrichment at the particle surface. The results show that a surface-near over-stoichiometric enrichment of Fe indeed causes a lattice dilation that counteracts a compression of the lattice at the particle surface as obtained for homogeneously alloyed particles. This was confirmed by EELS profiles obtained in STEM mode indicating an enrichment of Fe at the particle surfaces. In

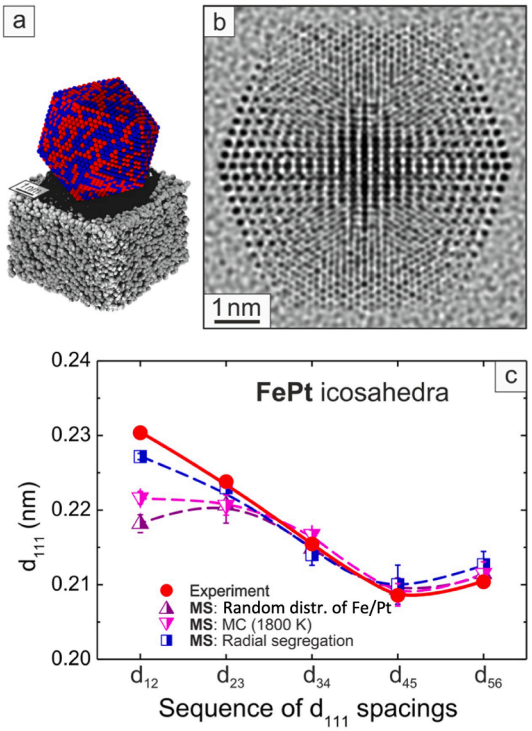

Fig. 33. A FePt icosahedral nanoparticle: (a) Atomistic model of a disordered FePt icosahedron of 8217 atoms (Fe red, Pt blue) on a 10 nm thick amorphous carbon support. (b) Calculated image as obtained by means of contrast simulation of the model particle in (a) after structural relaxation by means of molecular-static (MS) simulations. PCSI contrast: atoms dark on a bright background. (c) {111} lattice spacings, d_{111}, as function of the distance from the particle surface (in units of interlayer spacings). Example: "d_{12}" denotes the distance between the outermost layer denoted by subscript "1" and the first layer underneath in the direction of the center of the particle denoted by "2". "d_{23}" denotes the distance between the second and the third layer in the direction of the center. Red symbols indicate the measured experimental data. It is evident that the {111} lattice-plane separation is maximum at the surface, and it decreases towards the center of the icosahedron. Purple triangles indicate results of the MS simulation of a FePt icosahedron with random atom distribution. Magenta triangles indicate results of Monte Carlo (MC) simulation of a disordered $Fe_{46}Pt_{54}$ particle at 1800 K and subsequent MS relaxation. Blue: MS simulation of a FePt icosahedron with radial segregation of Pt toward the particle surface providing a good fit to the experimental measurements. (Reproduced from [189] with permission of American Chemical Society).

oxidized particles $NiFe_2O_4$ shells are formed (Fig. 35). The large lattice mismatch between the metallic core and the oxide causes the formation of step dislocations in the interface. The results provide evidence that Fe enrichment already occurs during nanoparticle fabrication by sputtering in an Ar atmosphere.

Using aberration-corrected CTEM Yu et al. [191] investigated the (111) surface and surface-near regions of Co_3O_4, a complex oxide with spinel structure (56 atoms per unit cell), at atomic resolution. This work is of fundamental importance not least because it demonstrates that in the combination of picometer-scale aberration-corrected electron microscopy with *ab-initio* calculations, electron microscopy measurements can significantly limit from the outset the number of structural models that have to be considered for the numerical calculations. Because of the structural complexity of the spinel structure, there is more than one possible surface termination depending on the surface orientation. In the [111] direction the stacking sequence of the atomic planes is such that there are 6 types of possible (111) surface terminations, and different models for the actual surface structure have been suggested in the literature. Fig. 36a shows an NCSI image along the $[1\bar{1}0]$ direction. This provides us with a view of the atomic arrangement in cross section in the (111) surface and in the atomic layers immediately below. Fig. 36b shows a model of the structure as calculated using a DFT first-principles calculation. The result is that Co^{2+} occupies the tetrahedral sites at the surface and Co^{3+} occupies the octahedral sites immediately below the first layer of oxygen atoms. Thus, the sequence $Co^{2+}-O_4-Co_3^{3+}-O_4-Co^{2+}-Co^{3+}$ is obtained for the six outer layers from the outside to the inside. The atomic relaxation at the surface is striking: the projected distance of the Co atoms in the outermost layer from the oxygen atoms immediately below is 84 pm in $[1\bar{1}0]$ projection compared to 110 pm in the bulk, and the plane distance from the first to the second atomic layer is 34 pm, half that in the bulk, 69 pm. A critical issue with spinel surfaces is the fact that these surfaces without considering charge relaxation are polar. Calculating the charge redistribution from Bader's theory taking into account the experimentally measured structural rearrangement at the surface, the authors found a depletion region of electronic charge, especially in the outer three atom layers $Co^{2+}-O_4-Co_3^{3+}-$. This charge redistribution is equivalent to an increased positive charge at the surface as required for the polarity compensation.

Following the same scheme just described He at al. [192,193] studied single-crystalline nanoislands grown *in situ* (stimulated by electron beam irradiation) on ZnO nanowires and nanobelts using aberration-corrected transmission electron microscopy combined

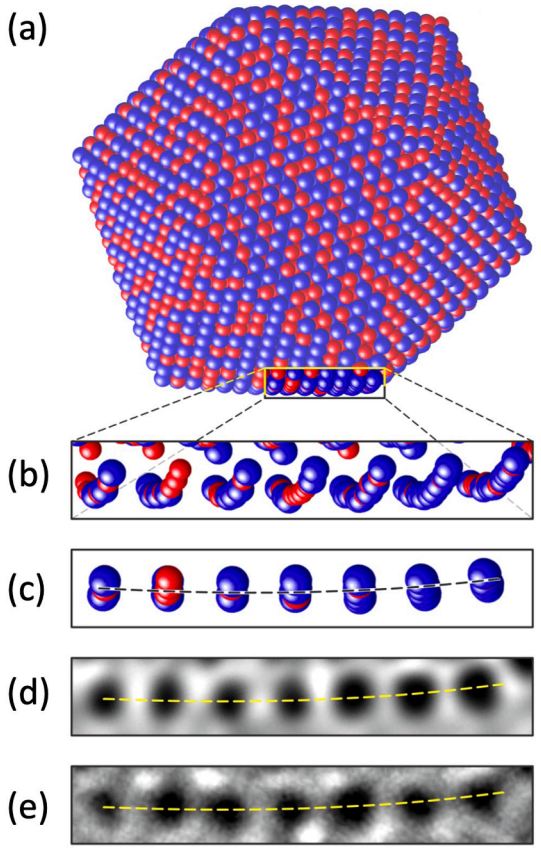

Fig. 34. Illustration of the bending of near-surface atomic layers of the icosahedral particle. (a) Atomistic structure of a disordered FePt icosahedron of 8217 atoms after structural relaxation through MS simulations (Fe red, Pt blue). For a better perspective view, the particle is slightly tilted away from one of its three-fold symmetry axes. (b) Enlarged view at a section of an atomic surface layer, as indicated. (c) View at the identical section as in (b), but now tilted to an exact 3-fold symmetry axes orientation. (d) Magnified section of a simulated image on the basis of the MS-relaxed model particle. The imaged section is identical to the section displayed in (c). (e) Corresponding experimental image. The yellow line serves as a guide for the eye. (Reproduced from [189] with permission of American Chemical Society).

with *ab initio* calculations. The displacements of both Zn and O atoms in the fresh $(10\bar{1}0)$ facets and the under-surface distributions of contractions and rotations of $Zn-O$ bonds could be measured at picometer-precision in excellent agreement with the theoretically predicted relaxation of ZnO $(10\bar{1}0)$ free surfaces. Lu et al. [194] carried out the first microscopic study of the as-grown {101} surfaces of SnO_2 nanobelts (Fig. 37). These structures are under consideration as a material for solid state gas sensors, and it had been concluded from earlier work that the {101}surfaces play an important role for this. Fig. 38 shows direct experimental evidence for an Sn-termination and a with respect to oxygen reduced surface. The same result was obtained in a study on the SnO_2 (100) and (101) surfaces using NCSI and DFT calculations [195]. In fact earlier first-principles calculations [196] have shown that the reduced (101) surface of SnO_2 is the energetically most stable surface under conditions of low oxygen chemical potential. Indeed an important parameter for the structure and stability of the surface of an oxide crystal is the chemical potential of oxygen. We mention here as another example the RuO_2 (110) surface, for which, employing DFT the Gibbs free energy was calculated to determine the lowest-energy structure in thermodynamic equilibrium with an oxygen environment [197]. The result was that at low oxygen chemical potentials, i.e. low pressures and/or high temperatures, the surface is bulk terminated while at higher values the surface is enriched in oxygen. The authors pointed out that structural studies are generally done *ex situ* (and usually in vacuum) and transferring the results to other environmental conditions can be problematic.

We would like to point out here an additional thermodynamic aspect, which concerns investigations by means of electron microscopy. And this concerns the fact that a sample exposed to the energetic electron beam is, strictly speaking, a driven thermodynamically open system whose steady states can deviate considerably from those in thermodynamic equilibrium [198–200]. In addition, the irradiation can provide atomic mobility, for example at ambient temperature, via the formation of atomic vacancies and interstitials, which would only be present purely thermally at much higher temperatures. And, of course, in high vacuum the chemical potential of oxygen is very low. Liu et al. [201] used NCSI and DFT calculations, in an investigation of the structure of the Co_3O_4 (001) surface, for which subsurface cation vacancy (SCV) reconstruction had been predicted in analogy to the finding in Fe_3O_4 [202]. They investigated the behavior of the cross-section preparation of the surface under the 300 keV electron beam and found high stability.

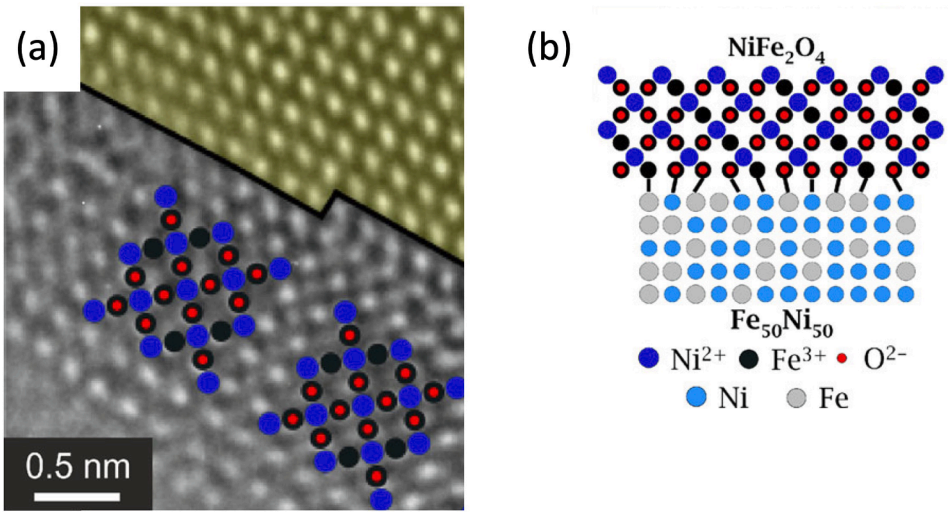

Fig. 35. The effect of oxidation on the surface-near lattice relaxation in a $Fe_{50}Ni_{50}$ nanoparticle. (a) Atomic resolution image taken along [100] of the interface (black line) between the FeNi core (shaded yellow) and the oxide shell below (shaded grey). The atomic positions are indicated. PCSI; atoms dark on a bright background. (b) Schematic of the structure of the interface: The mismatch of about 16 % requires the insertion of an additional Fe/Ni atomic plane at every sixth or seventh Fe^{3+} atomic column of the oxide. (Reproduced from [190] with permission of Springer Nature).

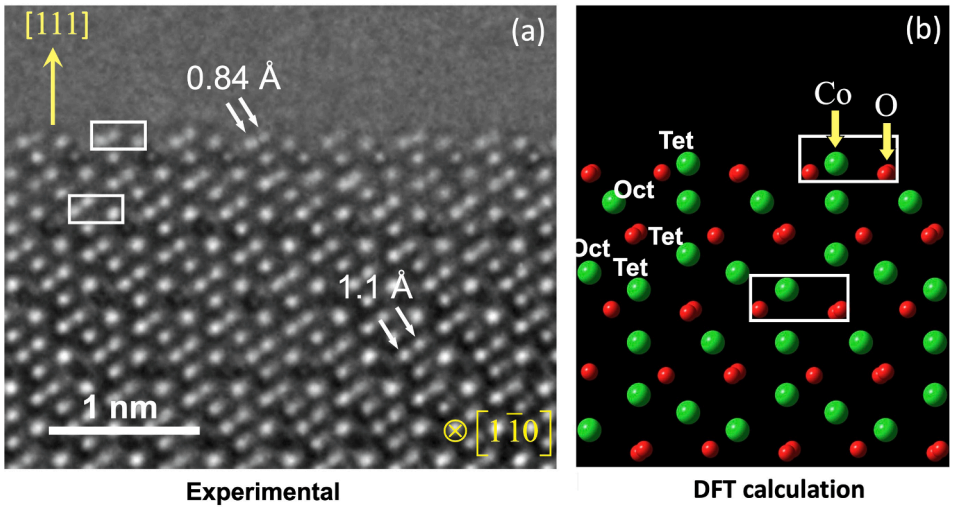

Fig. 36. (a) An experimental NCSI micrograph of the (111) surface of Co_3O_4 spinel in a cross sectional preparation. The viewing direction is [1$\bar{1}$0]; the sample thickness is 7.5 nm. The projected distance of the Co atom positions in the outermost layer from the oxygen sites immediately below is 84 pm compared to 110 pm in the bulk, and the plane distance from the first to the second atomic layer is 34 pm, half that in the bulk, 69 pm. (b) Atomic model of the (111) surface of Co_3O_4 relaxed on the basis of DFT calculations. The green and red balls represent Co and O atoms, respectively, with tetrahedral (Tet) and octahedral (Oct) Co sites labeled. (Reproduced from [191], Copyright (2010) by the American Physical Society).

From this they concluded that the surface under the microscope conditions is determined solely by the equilibrium between the specimen bulk and surface. Quantitative NCSI showed that the Co_3O_4 (001) surface is bulk terminated. This was confirmed by the DFT calculations at low oxygen chemical potential. Moreover, the difference with respect to Fe_3O_4 could be attributed to a surprisingly much lower formation energy for atomic defects in Fe_3O_4. In studies of the surface structure of $MgAl_2O_4$ (111) [203] and Cr_2O_3 (11$\bar{2}$0) [204], it was observed that surface steps of the height of a unit cell move back and forth under the 300 keV electron beam. That is, the whole surface layer dissolves and also re-forms, always with the same surface structure, from which it can again be concluded that this structure is stable under the investigation conditions, characterized by a low chemical potential of oxygen. Further below (Section 7) we will find a case where the surface structure reversibly formed under the electron beam depended sensitively on whether vacuum or, alternatively, an oxygen atmosphere was set in an environmental electron microscope.

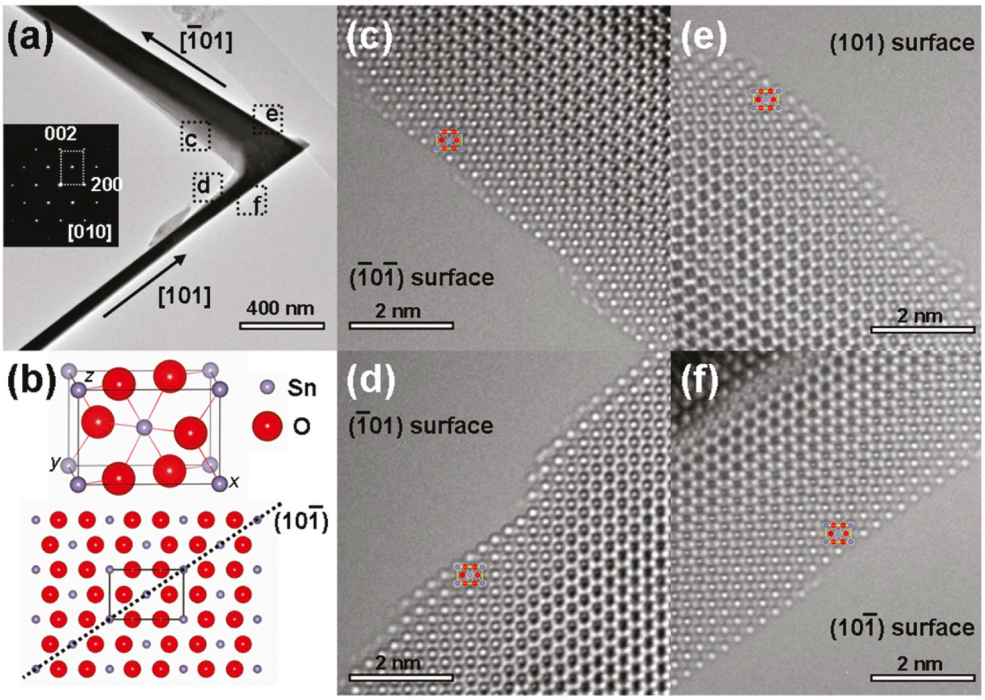

Fig. 37. NCSI of a SnO_2 nanobelt. (a) Low-magnification overview along [010] indicating the zigzag shape. Inset: Diffraction pattern along [010] zone axis. (b) Schematic of the rutile structure of SnO_2 and projection along [010], displaying the $(10\bar{1})$ plane seen in cross section. (c-f) Images acquired of the four {101} side surfaces labeled with c, d, e, and f, respectively, in (a). The surfaces are in projection all terminated by a bright Sn atom contrast. The lower-intensity dots correspond to oxygen atoms. See Fig. 38. Reproduced from [194] with permission of American Chemical Society).

Summarizing it is obvious that a sample under electron irradiation is in the general case an open, energetically driven system, the theoretical treatment of which, except for a few special cases, has not been attempted so far. On the other hand, the work on surface-near or cluster atomic structures demonstrates the fruitful interplay between aberration-corrected CTEM in the picometer range with *ab-initio* calculations serving the same size range.

6.7. The three-dimensional shape of a nanocrystal

How high is the resolution of atomic observations along the third dimension, the z-direction (along the viewing direction) in CTEM? This question was investigated in [205,206] on MgO nanocrystals. In particular, this investigation was concerned with the question of the extent to which it is possible to measure the exact arrangement of the atoms on the top and bottom of the crystal separately on the basis of a *single* image. This means that not only the number of atoms in a given atomic column is to be measured, but it is to be determined whether an atom is at the top or bottom of the column. This is feasible by taking advantage of the fact that in CTEM, due to coherent electron scattering, the atomic contrast within a thickness of the order of magnitude of the first extinction length depends sensitively on the local sample thickness. This actually allows to distinguish the two cases where an atom is added to an atomic column at the top or at the bottom side of the sample. MgO was first studied by Lu et al. [207] using the NCSI technique and DFT calculations. According to the classification of Tasker [208], the (100) surface is an ideal nonpolar type 1 surface with charge-neutral sub-surface atomic planes. The distance between the two outermost lattice planes is only 2.5 % smaller than the corresponding value in the bulk. In addition, the standard method of producing thin electron-transparent samples using the Ar-ion milling technique yields an atomically flat surface that is free of amorphous cover layers. This qualifies MgO nanoparticles as a quasi-ideal model system.

An experimental image of the MgO nanocrystal acquired along the [001]crystallographic direction is shown in Fig. 39 [205]. Since in the present case, in contrast to the case of the STO/LAO/STO heterostructure treated above in Section 6.5, the calibration of the measurement cannot be carried out employing a suitable template, the optical and the specimen-related parameters have to be determined in a different way. Again, as above, the set of primary measured data is given by $\widehat{\boldsymbol{I}}(x,y)$. On this basis, over a certain image area, the intensities were averaged, and these averaged areas were taken as reference for the iterative fit of the calculated to the experimental data in order to obtain the set of imaging parameters. For this a crystal was assumed with perfectly flat top and bottom surfaces. This calibration (step 1) was carried out as described before. The instrumental loss in total electron current was measured to be 1.3 % and considered in the calculation by $\zeta = 0.025$. For the effective image spread $\sigma = 16$ pm was found to give an optimum fit. Fig. 40a shows the experimental image (framed region in Fig. 39) and for comparison, in Fig. 40b, the quantitatively best-fitting simulated image (displayed on the same intensity scale). The individual intensity maxima are indexed according to their horizontal

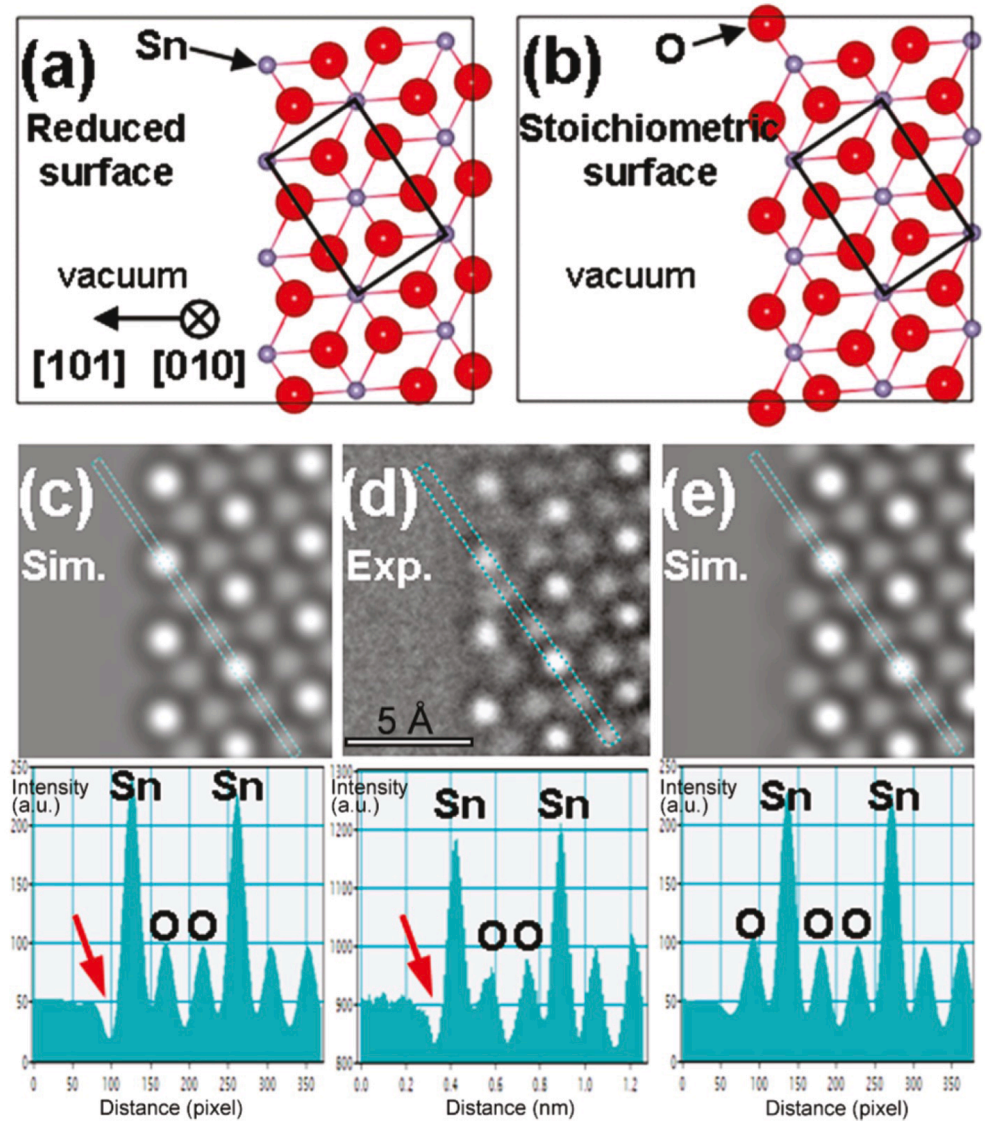

Fig. 38. Structure models for the SnO_2 (101) surface projected along [010]. (a) the so called *reduced* and (b) the *stoichiometric* surface structure. Sn – small blue symbols, O – large red symbols. (c,e) Corresponding simulated images. (d) An experimental image in NCSI mode (an enlarged part of Fig. 37f). The lower parts of (c-e) depict intensity line profiles along the [100] direction corresponding to the dotted lines indicated in the images. The red arrows indicate the intensity reduction due to electron diffraction channeling (compare Fig. 7). Reproduced from [194] with permission of American Chemical Society).

position i and the vertical position j. For these a quantitative comparison of experimental (full circles) and simulated (open squares) peak intensities, normalized with respect to the mean intensity of the image, is depicted in Fig. 40c. The agreement between simulation and experiment is excellent. The residual difference between the experimental and calculated peak intensities is characterized by a rms value of 0.0053, which is mainly due to electron counting noise of the measurement.

The crucial point of whether the adding of an atom on the top surface can be distinguished from the adding of an atom at the bottom surface as well as the possibility to detect vertical atomic-column shifts (leaving the number of atoms in the respective column unchanged) was investigated by image simulation [205]. Examples of this are shown in Fig. 41, demonstrating the change in contrast caused by the addition of individual atoms on the top or bottom of the sample and the effect of a column shift. The reference atomic column R comprises 8 atoms in (a,b) and 9 atoms in (c,d). In the line scan diagrams $\Delta I(x)$ denotes the difference in the intensity of the contrast of the atomic column at location x with respect to the intensity of the contrast at the location of the reference column R. The dashed horizontal lines denote the estimated error for extracting peak intensity values from the experimental image. It is evident that $\Delta I(x)$ provides a specific fingerprint for the different types of process.

The results regarding the atomic occupation of the terminating atomic layers on the top and bottom of the sample are shown in

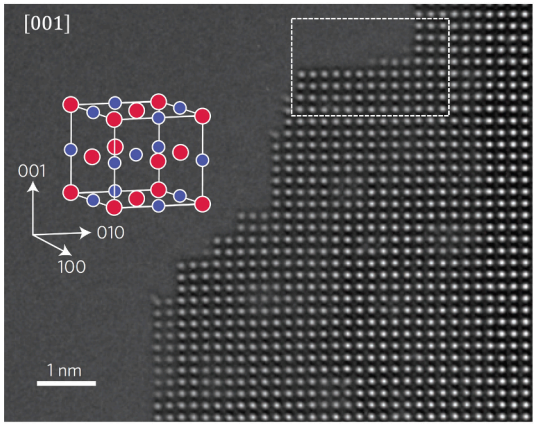

Fig. 39. Image of an MgO nanocrystal acquired along the [001] crystallographic direction under NCSI conditions. A perspective view of the MgO unit cell is shown in the inset on the left side (Mg: red, O: blue). In the image MgO atomic columns seen end on appear as bright dots on a dark background. Different intensities at atomic positions can be interpreted in terms of different length and relative height of the respective atomic columns along the viewing direction. The area with a dashed frame concerns the details in Figs. 40,42. (Reproduced from [205] with permission of Springer Nature).

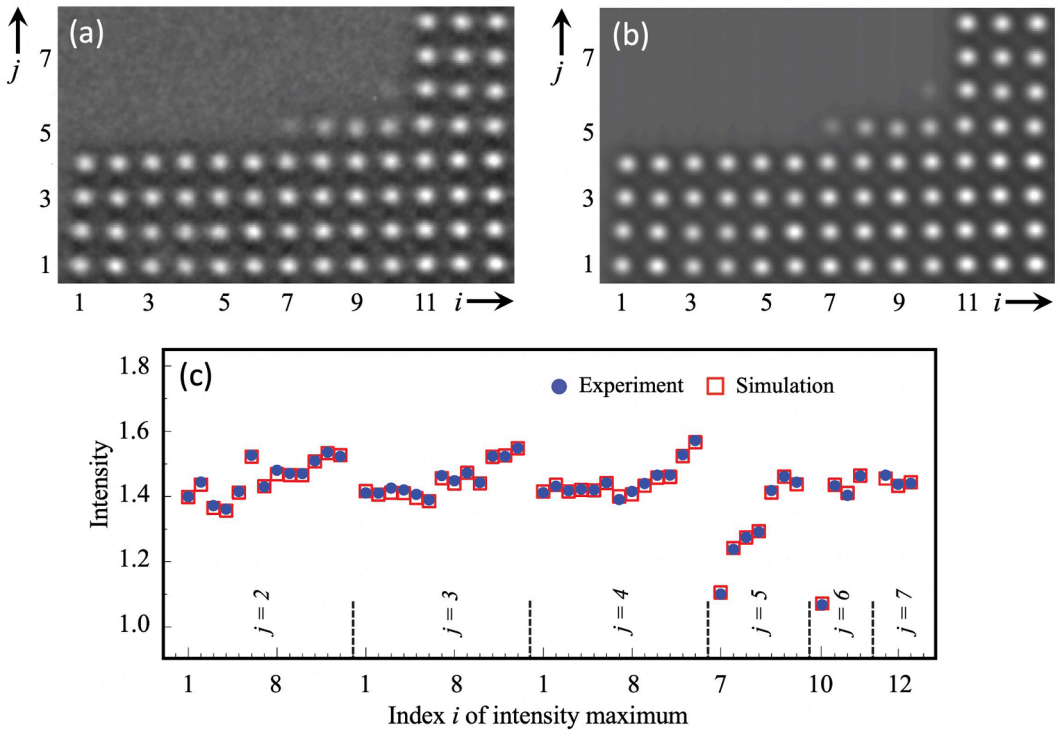

Fig. 40. (a) Experimental image showing the framed region in Fig. 39. (b) Best-fitting simulated image shown on the same intensity scale. The individual intensity maxima are indexed according to their horizontal position *i* and the vertical position *j*. (c) The quantitative comparison of experimental (full circles) and simulated (open squares) peak intensities, normalized with respect to the mean intensity of the image, indicates an excellent fit. (Reproduced from [205] with permission of Springer Nature)

Fig. 42. The color coding indicates four types of atomic locations. Mg: red; O: blue. Brown color designates those Mg sites which are occupied by an atom having formally half the atomic nuclear charge number of magnesium. Accordingly, the green color denotes those oxygen atom positions which are occupied by an atom having formally half the nuclear charge number of oxygen. A possible explanation for these fractional atomic numbers is migration of the surface atoms during the exposure time of the image. On the one hand, these surface atoms are less strongly bound, and, on the other hand, as described in section 5.2 surface diffusion can be enhanced by the impact of electrons on the atoms [122,123]. In the case of the Mg atoms ($N_Z = 12$), it is likely that this observation provides

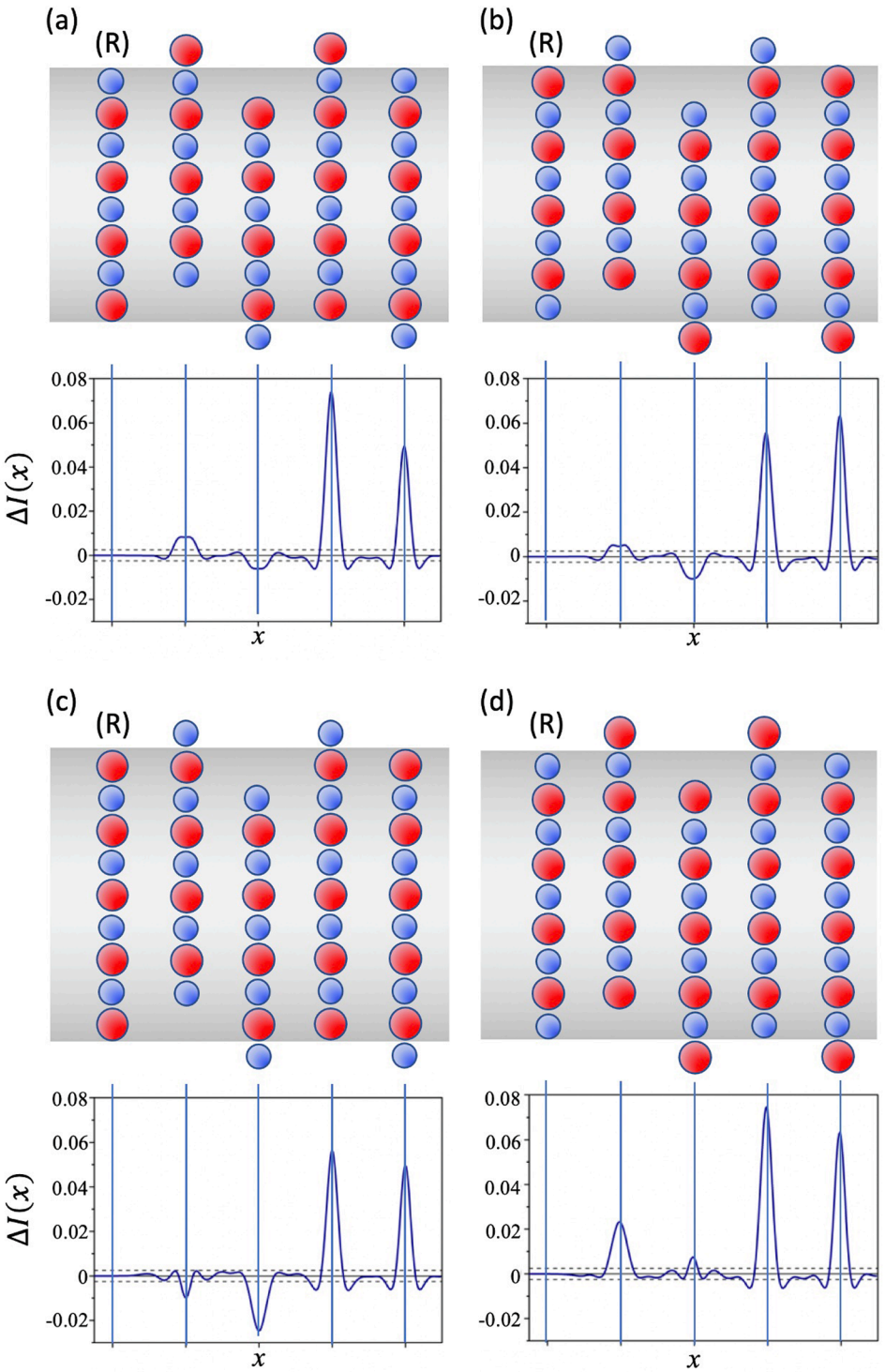

Fig. 41. An example from the study by simulation of the change in contrast caused by the addition of individual atoms on the top or bottom of the sample and the effect of a vertical atom column shift. R denotes the reference atomic column, which comprises 8 atoms in (a) and (b) and 9 atoms in (c) and (d). Mg: red; O: blue. $\Delta I(x)$ denotes the difference in the intensity of the contrast of the atomic column at location $\times$ with respect to the intensity of the contrast at the location of the reference column. The horizontal band indicated by dashed lines marks the experimental noise level. The simulation study shows that, due to the favorable signal-to-noise level, the intensity can be taken as a fingerprint for the individual local atom configuration. This allows not only to count the atoms, but also to determine their vertical position with respect to the upper and lower sample surface. (Reproduced from [205] with permission of Springer Nature)

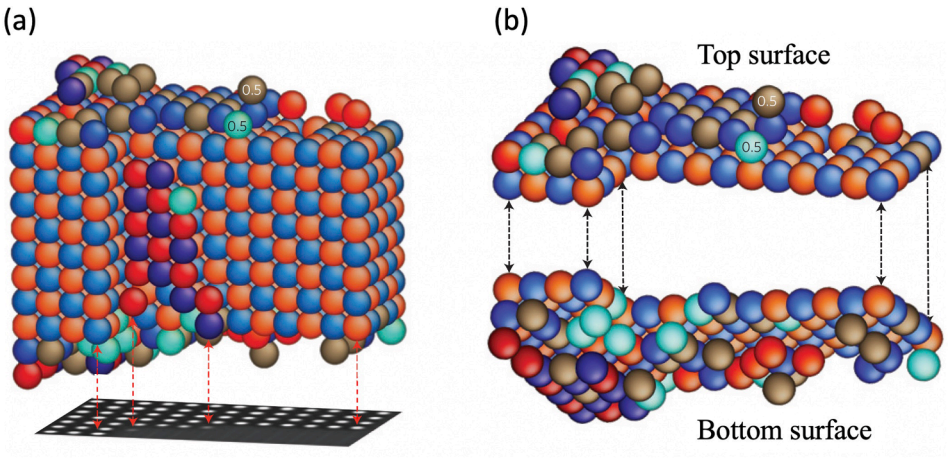

Fig. 42. (a) Atomically reconstructed shape of the part of the MgO nanocrystal framed in Fig. 39. (b) Pseudo perspective views of the terminating atomic layers at the top and bottom surface. The color coding indicates four types of atomic positions. Mg: red; O: blue. Brown color designates those Mg sites which are occupied by an atom having nominally half the atomic nuclear charge number of magnesium. The green color indicates those O-atom positions which are occupied by an atom having nominally half the nuclear charge number of oxygen (see text). (Reproduced from [205] with permission of Springer Nature).

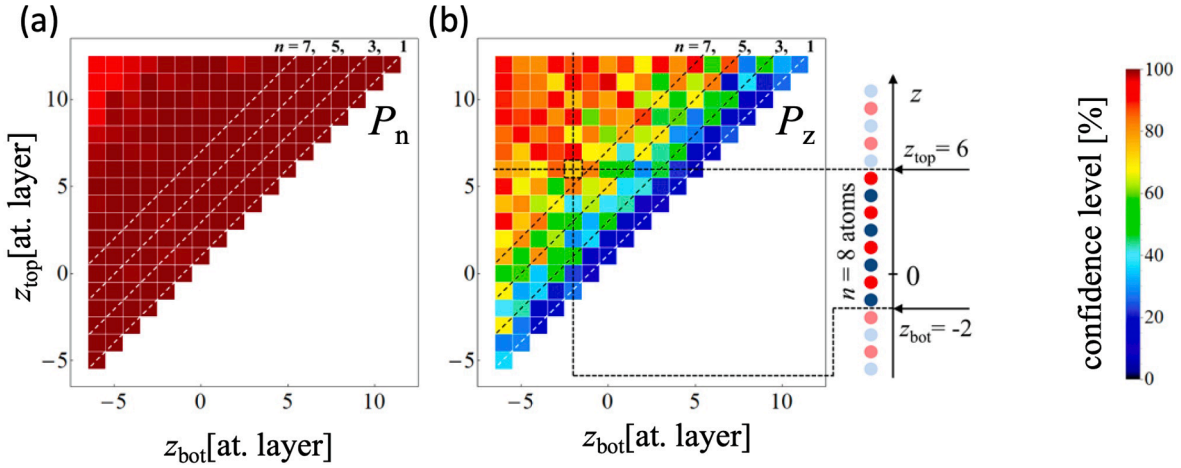

Fig. 43. Confidence levels for the atomic column configurations derived from an experimental image. (a) The confidences P_n for counting correctly the number n of atoms in each column with single-atom precision. (b) Confidences P_z for determining correctly the column z-position with atomic plane precision. One pixel in the graphs corresponds to an atomic column configuration that is defined by the two variables z_{top} and z_{bot}. These variables are the z-positions terminating the column above the top atom and below the bottom atom, as illustrated in (b) on the right-hand side. Column configurations with n = 1, 3, 5 and 7 atoms are marked by dashed diagonal lines. Moving along such diagonal lines corresponds to a rigid shift of columns with a constant number of atoms $n = z_{top} - z_{bot}$ with respect to the common reference plane at $z = 0$. The color indicates the success rates obtained. These were determined by Monte Carlo simulations on the basis of the experimentally observed noise level. The overall result is that the number of atoms in a column can be determined in general with very high confidence. The determination of the vertical column z-position is also reliable with high confidence for columns that contain 5 or more atoms. For very short columns that consist of one to four atoms, the success rate drops below 50 %. This, e.g., is the case in Fig. 40 for atom positions [i,j]= [7,5] and [10,6], respectively, for which the confidence level is 40 %. (Reproduced from [205] with permission of Springer Nature)

evidence for carbon ($N_Z = 6$) contamination on the surface. Such contamination is well documented in the literature [209], and *ab-initio* calculations show that carbon substitutes magnesium at the surface [205]. From a methodological point of view, it is important that the accuracy of the statements about the nature of the surface atoms and of the atomically resolved shape as a function of the sample thickness and the signal-to-noise ratio was in this work also investigated in detail using Monte Carlo simulations (Fig. 43). It is not surprising that it is constitutive that with sample thicknesses of only a few atoms and low signal-to-noise ratios single-atom measurements in the atomic range are only possible with correspondingly low confidence levels .

6.8. Atoms in cages and the experimental determination of precision

We have described above (Section 5.4) how important it is to distinguish between "resolution" and "precision" for practical work in atomic dimensions. The question now is, how precision can be specified quantitatively. This quantity corresponds to the error of the measurement with respect to the position determination, and it is reasonable to define this error by the standard deviation from the mean value of all measurements. In the previous section, we have seen that the problem of quantifying precision can be approached by means of image simulations, in which noise can also be included in an appropriate way. On the other hand, a practical measure of precision can be obtained experimentally. This is practiced in the two following cases, which concern measurements of the position of atomic contrast maxima, which are bound to a certain location on the average, but can deviate a little from it in the individual case.

In both cases, an additional element comes into play, and this is the fact that the atomic contrast rarely comes from a single atom, but generally from a whole column of atoms aligned along the viewing direction. If the atoms in a column can move horizontally, that is, perpendicular to the viewing direction, then this column will yield an intensity maximum in the sum of the scattering events, which is laterally displaced. This means that even if in the projection the laterally shifted atoms in a column are optically not separable, one can at least make the statement that such a shift is taking place.

Jia et al. [124] used NCSI to study the atomic structure of $(Bi_{1.5}Zn_{0.5})(Nb_{1.5}Zn_{0.5})O_7$ (abbreviated as BZNO). This compound is a typical representative of the pyrochlore class, whose interesting physicochemical and technical properties have been the subject of extensive investigation for some time. However, never before had pyrochlore been studied using atomic resolution electron microscopy. Fig. 44a shows a view along a crystallographic [112] direction. A special type of disorder can be seen, namely, along the $[11\bar{1}]$ direction, every other atomic row in the horizontal direction is irregularly "wavy" (compare the well ordered atom row above the white dashed line with the disordered atom row above the yellow dashed line). This image gives direct evidence that part of the atoms of the compound shows so-called "displacive disorder". The space group of BZNO is $Fd\bar{3}m$ (No. 227) and there are eight formular units per cell. BZNO can be written as $A_2B_2O_7$ consisting of two interpenetrating lattices, an A_2O tetrahedral and a B_2O_6 octahedral network. The *A* atoms are in the 16*d*, the *B* atoms in the 16*c* *Wyckoff* positions. The structural model derived from the X-ray powder diffraction data assumes that the atoms do not occupy the ideal pyrochlore lattice sites. Rather the *A* atoms should take one of 6 possible sites forming a regular hexagon put up by a shift of 39 pm along the six < 112 > directions with the ideal 16*d* position as center. In other

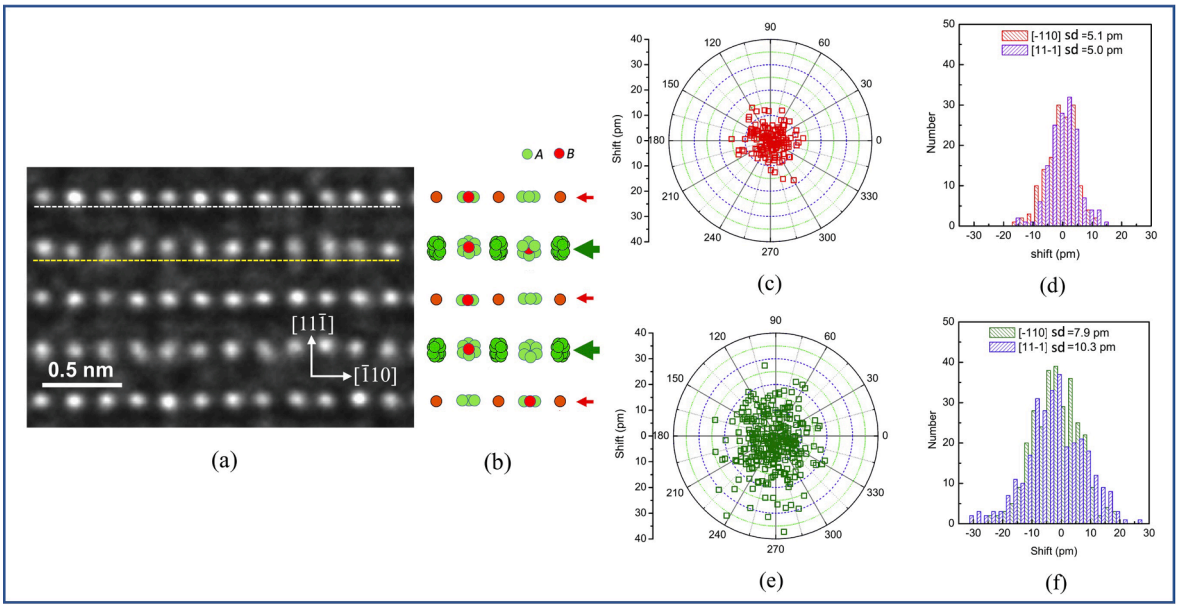

Fig. 44. Micrograph of the pyrochlore compound $(Bi_{1.5}Zn_{0.5})(Nb_{1.5}Zn_{0.5})O_7$ (BZNO) also written as $A_2B_2O_7$ employing NCSI along the crystallographic [112] direction. (a) Along the vertical direction $[11\bar{1}]$ two different types of horizontal rows of atomic intensity maxima extending along $[\bar{1}10]$ can be distinguished; almost regular ones (e.g. atoms above the white dashed horizontal line) and irregular ones (e.g. atoms above the yellow dashed horizontal line). (b) Corresponding cation positions of the structural model (oxygen atoms omitted for clarity). *A* atoms green, *B* atoms red symbols. As indicated in (b) the atomic contrast in the horizontal rows denoted with a large green arrow consists of two overlapping, optically not resolved contrast maxima appertaining to a central *B* atom and a shifted *A* atom (all possible *A*-atom positions are shown schematically, only one of these possible sits is occupied). The resulting contrast maximum is shifted towards one of the six possible sites of a hexagon. In (e) the results of the position measurements with respect to the average ideal lattice are shown. A rather broad distribution is obtained characterized by a standard deviation ("sd") from the mean of 7.9 pm and 10.3 pm (f). The position measurements (c,d) on the atoms in the regular atom rows (small red arrows) serve to experimentally determine the measurement error. These sites, according to the structure model are stable (*A* atoms not shifted). Taking the standard deviation (d) as a measure for the precision we find a value of 5 pm. This means that, as a result of this low measurement error, the measurements on the shift of the contrast maxima in the irregular rows (large arrow) displayed in (e,f) are statistically significant. (Reproduced from [124] with permission of Elsevier).

words, the *A* atoms should be bound within a "cage" consisting of the six possible hexagon sites. For reasons of space and valence, only one of the six places can be occupied at a time. Achieving evidence for this model at the atomic level using electron microscopy is a special challenge because along the line of sight the distance of the *A* atoms from the nearest *B* atom is only 39 pm, which is below the Rayleigh resolution of today's electron microscopes. Jia et al. nevertheless succeeded in detecting the off-center displacements of the *A* atoms. They took advantage of the fact that when *A* and *B* atoms are close to each other in the projection, the sum maximum of the intensity is shifted in the direction $< 112 >$ with respect to the central *B* atom. Fig. 44b shows the atomic model in the [112] projection direction of part (a). The atomic row above the yellow dashed line corresponds to the atomic row along the thick green arrows. Since the (green) *A* atoms and the (red) *B* atoms cannot be separated due to the limited resolving power, each of the bright atomic contrasts in the image actually consists of two atomic maxima. In fact, the image shows that the atomic contrasts are shifted in a sort of a random way. Part (e) depicts now the values of the off-center shift vector in the rows with the large green horizontal arrows with respect to the average lattice derived from the quantitative image simulation. The atomic contrast maxima observed are distributed over an annular region of about 25 pm in diameter centered at the projected 16*d Wyckoff* positions. The standard deviation of the histogram in (f) is 7.9 and 10.3 pm in the two crystallographic directions indicated in (a). Of course, in order to have a statistically significant result, the measured values must be larger than the measurement error. The authors used the measurement of the atomic positions in the atomic rows with the small red horizontal arrows above and below the atomically shifted rows to experimentally determine this error. These atomic positions, according to the model, should show no displacement in [112] projection. Fig. 44c shows the measurements of the direction and the modulus of the shift vectors with respect to the average reference lattice. Taking the standard deviation in the appertaining histogram in (d) the measurement error is determined to be 5 pm. This indicates that the results depicted in (e,f) are statistically significant. That the modulus of the shift vector comes out somewhat smaller than the predicted value in the model derived from the scattering experiments is not surprising. The position of a given contrast maximum is the sum of the (optically not separated) single maxima of *B* and *A*, and therefore this value must always come out smaller than the shift of the *A* atoms. We also note that, which is investigated and described in more detail in the mentioned paper, the contrast figure is the sum of the sequential scattering of the electrons of a whole atom column. As a result, depending on how within this column the *A* atoms are distributed to the different hexagonal sites, very different shift vectors can be obtained in the sum.

The second example demonstrating the high precision of measurements made using NCSI near the resolution limit of aberration-corrected electron microscopy is a study by Ge et al. [210] of the position of Ce rattler atoms within the icosahedral cages of Ce(Fe,Co)$_4$Sb$_{12}$ skutterudites. In this case, too, it is indispensable to determine the measurement error or the precision of the measurements experimentally in order to be sure that the measurement result is statistically significant. Skutterudites represent an interesting class of materials that are candidates for use in thermoelectric converters (e.g. [211]). They exhibit a cubic structure (space group: $Im\bar{3}$, No. 204). In particular in (Fe,Co)$_4$Sb$_{12}$ the Fe,Co atoms are in the 8*c*, and the Sb atoms in the 24 *g Wyckoff* positions. In the expression for the thermo-electric figure of merit for the skutterudites, thermal conductivity occurs in the denominator, and there is considerable interest in further reducing the thermal conductivity of the compounds through suitable structural modification. One way to do this is to accommodate additional atoms in the central interstitial sites of the icosahedral atomic arrangements of the basic structure. The idea is that, with suitable valence and a correspondingly small atomic size, these additional atoms can move relatively freely ("rattle") within the cage of surrounding icosahedral atoms, so that they act as scattering centers for the phonons and thus reduce the thermal conductivity. This has also been successfully implemented. However, it turned out that the effect of the so-called "filler" atoms was much stronger than the earlier theories had predicted. One of the possibilities how this could be explained is that the filler atoms do not sit exactly in the center of the icosahedron, but show displacive disorder (similar to what was discussed above for BZNO) [212,213]. This is, however, difficult to prove by scattering experiments, because these are integral methods which average over the different possible displacement configurations of the filler atoms. In contrast, the CTEM images obtained using NCSI (Fig. 45a) show both the skutterudite atoms and the individual Ce filler atoms. Not only can the displacement of the central filler atoms be seen directly, it can also be measured using the quantitative electron microscopy methods (red arrows). Fig. 45b shows schematically a section of the skutterudite lattice in a projection along the [001] direction. A lattice unit cell is indicated. The blue symbols denote the two Ce atom positions, Ce-1 and Ce-2, whose displacement from the central position (defined as the center of the line connecting the two vertical Sb atoms (denoted by "1" and "2" in Fig. 45a,b) is given in (f)-(h). The result is unambiguous evidence that the filler atoms are located off-center, with a mean displacement vector of length 18.6 pm and a projected preferred direction along the x-direction (parallel to [100]). The authors measured the positions of the neighboring Sb atoms (identified as "1" to "4" in Fig. 45b) to determine the measurement error in this way (Fig. 45 c). Taking the standard deviation in Fig. 45 d,e, the measurement error is 4.5 pm.

7. Experiments carried out *in situ* at atomic resolution

The fact that samples change during their examination in the electron microscope is an observation that goes back to the early days of electron microscopy. Examples are changes due to vacuum conditions (evaporation of sample components or a reaction at the sample surface with residual gases), the change of the sample structure and composition due to radiation damage or simply as a result of heating of the sample due to high electron beam current densities. While these are mostly effects that hinder investigations, a branch of electron microscopy developed in the sixties and seventies that specifically exploits the possibilities of electron microscopy to study dynamic processes at high optical magnification *in situ*[21] (Refs. [214,215]). This first period of *in-situ* experiments was related to high-

[21] In fact, v. Ardenne [214] and Ruska [215] already reported on gas reaction experiments in situ (employing differential pumping) in the electron microscope as early as 1942.

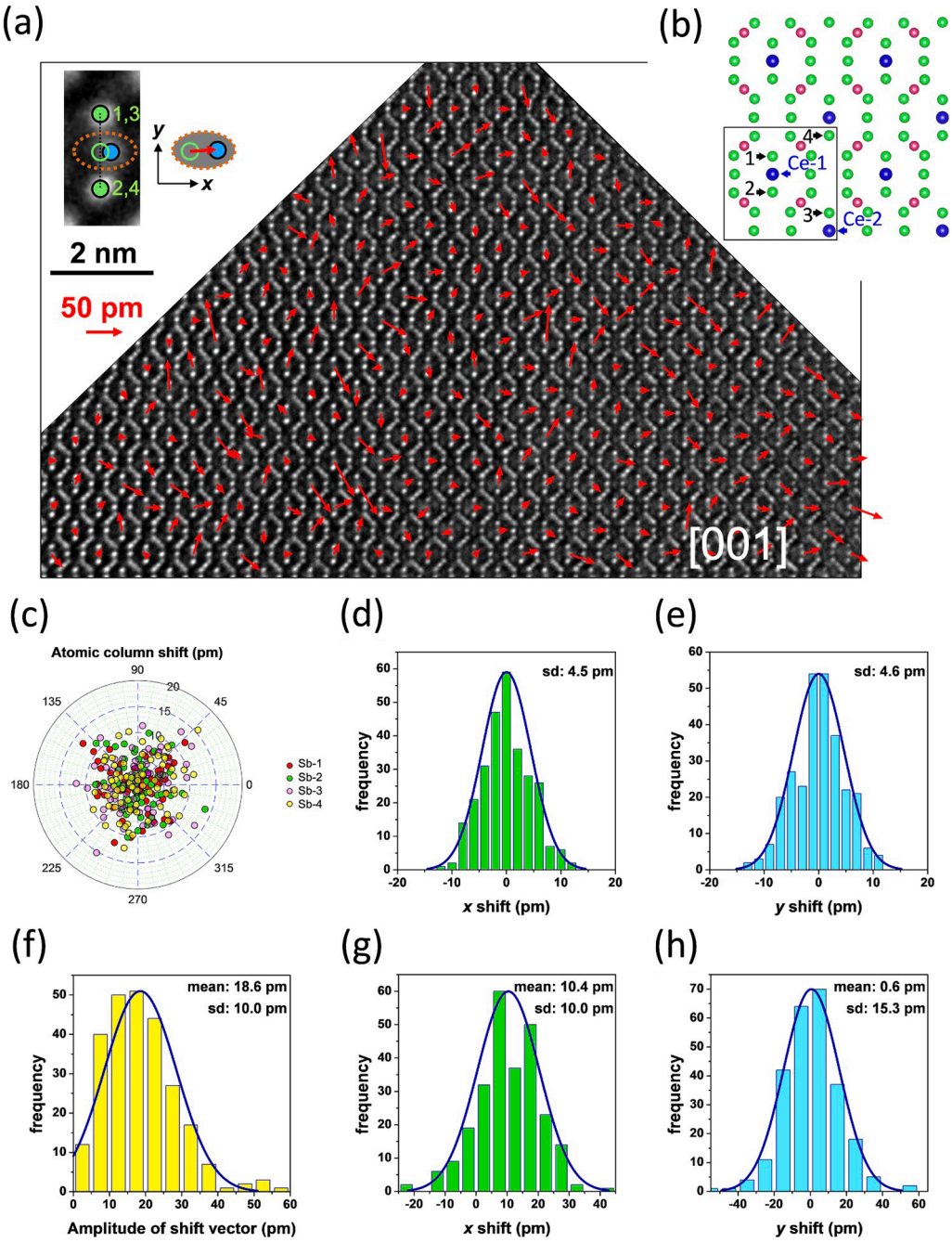

Fig. 45. Micrograph along [001] in NCSI mode of the skutterudite $Ce(CoFe_3)Sb_{12}$. (a) All three types of atoms are clearly imaged bright on a dark background. (b) shows a section of the skutterudite lattice in the [001] direction. A lattice unit cell is indicated (square). The blue symbols denote the two Ce atom positions, Ce-1 and Ce-2. In (a) the red arrows form the vector map of the off-center shifts of the Ce atoms. The inset on the upper left illustrates this central position (defined as the center of the line connecting the two vertical Sb atoms (denoted by "1" and "2" and "3" and "4", respectively in (b)). The position measurements on the fixed Sb atoms 1 to 4 allow to experimentally measure the precision, i.e. the measurement error. The results are displayed in (c). The precision defined as the standard deviation ("sd") is shown in (d) and (e) for the histograms in x- and y-direction; it is 4.5 pm and 4.6 pm, respectively. This provides the basis for the evaluation of the vector map, red arrows, of (a). The histogram for the modulus of the shift vector of the central Ce filler atoms is shown in (f). The mean value of is 18.6 pm with a standard deviation of 10 pm. Splitting this into components parallel to y and x (cf. inset in upper left of (a)) a mean value of 10.4 pm and sd = 10 pm is obtained in (g) for the x-component and 0.6 pm and sd = 15.3 pm is obtained for the y-component in (h). This indicates that the projected Ce-atom shift is preferentially aligned with the x-direction. On the basis of this low measurement error the results for the off-center Ce-atom shifts can be considered as statistically significant. (Reproduced from [210] with permission of the authors and Wiley -VCH GmbH).

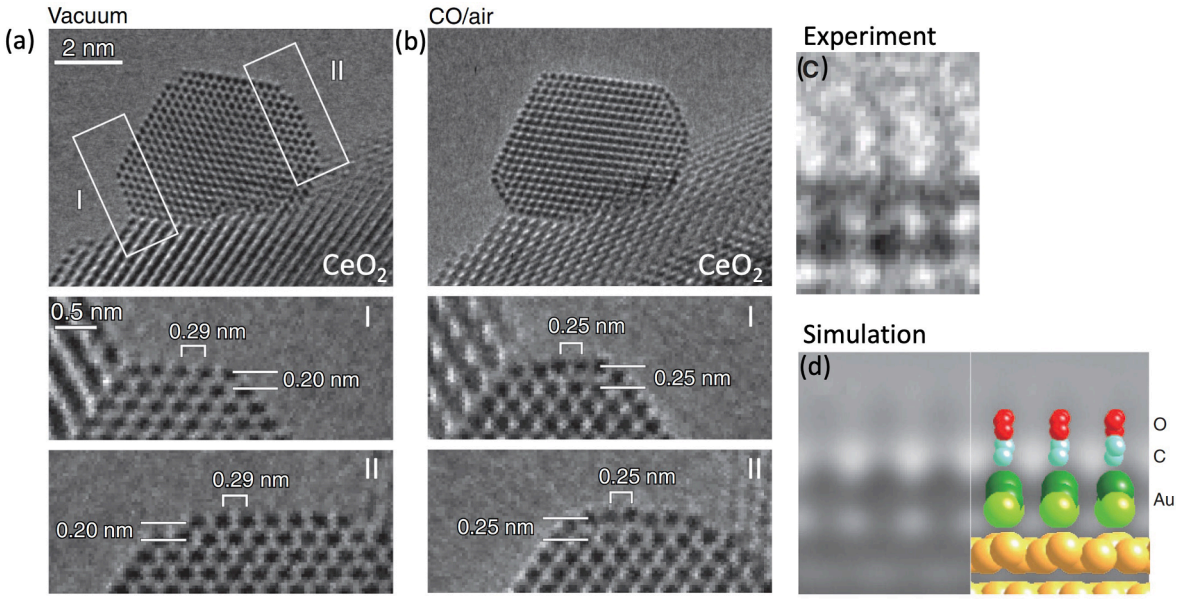

Fig. 46. A gold nanoparticle on CeO_2 in an environmental transmission electron microscope (ETEM) (a) in vacuum, and (b) in the reaction environment (1 vol.% CO in air at 45 Pa). PCSI: Atoms dark on a bright background. Two {100} facets are indicated by "I" and "II". The magnified images if the two facets are shown underneath. The measurement of the lattice parameters indicates that under reaction conditions (at ambient temperature) the sections I and II have transformed into the Au{100}-hex(1x5) reconstruction. (c) shows a magnification of the reconstructed facets. (d) depicts the results of image simulation on the basis of atom positions obtained by *ab-initio* calculations. The model is shown in the inset on the right. (Reproduced from [237] with permission from the American Association for the Advancement of Science).

voltage electron microscopy and exploited the fact that the comparatively large dimensions of the objective lens in these microscopes were favorable for accommodating miniaturized experimental equipment. There were dedicated microscopes in which this equipment was permanently installed and microscopes where the *in-situ* manipulation devices in the form of side-entry goniometer systems could be flexibly exchanged for other experimental stages or for normal goniometers. Facilities for microscopy at temperatures down to helium temperature [216] or at high temperatures above 1000 °C [217], which at the same time had a double tilt capability to do diffraction-contrast experiments, allowed the observation of e.g. phase transformations and plastic deformation under direct observation [218–220]. An overview on some of this early work can be found in Refs. [221–223]. For completeness, we also mention the monograph on *in-situ* experiments, Ref. [224].

After the introduction of aberration correction, *in-situ* electron microscopy entered a new phase. Here two fundamental points are of interest. Aberration-corrected optics allows higher resolving power and the analytical methods now available in modern electron microscopes, in particular EELS, can be used together with the *in-situ* capabilities [225,226]. On the other hand, ultra-high resolution requires very restrictive dimensions of the objective lens pole piece, so accommodating experimental devices is a challenge that requires micromechanics. In essentially all set-ups side-entry stages are used. Two groups of developments deserve particular mention here. The first is the development of closed gas and liquid reaction cells separated from the microscope vacuum by electron transparent windows, which are used to study catalytic and other reactions [227,228]. In general, the possibilities for true atomic resolution are limited because, for technical reasons, the device has only one tilt degree of freedom, making it difficult to set the Laue orientation necessary for atomic resolution. In most cases, the two windows sealing the wet cell against the vacuum consist of 20 to 100 nm thick SiN films (which in turn limit the possibilities for atomic dissolution). However, single-sheet (one atomic layer thick) graphene films are also used for liquid encapsulation. These allow atomic resolution and, because they are highly conductive, have the added advantage of significantly reducing radiation damage from radiolysis in many materials. Such a setup was successfully employed to study atomically resolved colloidal nanocrystal growth with the aberration-corrected TEAM instrument [229]. The second development concerns the construction of a line of dedicated *environmental transmission electron microscopes* (ETEMs), which allow physical and chemical experiments to be performed at variable temperature in a controlled gas atmosphere [230–233]. In this case the specimen and its reactive environment is open to the microscope chamber. The zones with an appropriate pressure, up to some hundred Pascal, of the reaction gas are separated by differential pumping from the zones for which a high vacuum quality is required for the microscope to function. Within the framework of this type of construction there is a lot of flexibility as far as the stages are concerned, e.g. double-tilt for precision adjustment of the specimen orientation, heating, cooling, and straining. And if a higher gas pressure (due to enhanced scattering of electrons) is a problem for microscopy, then the gas can be drained from the apparatus in order to achieve high optical resolution. Accordingly, if there is a risk that the kinetics of a reaction will be affected by radiolysis of the gas molecules when the electron beam is switched on, the microscope can be operated in an interval mode for gas reaction and imaging, respectively. Not all electron microscopes in which experiments have been performed in the second phase of *in-situ* electron microscopy since the late 2000s

have an aberration-corrected objective lens. Because we believe that the respective work is of general importance to the field, we will also briefly mention below some studies done in uncorrected microscopes. In this case, the lattice-fringe method for high-resolution imaging is used, whose possibilities for atomic imaging (see Section 2) are very limited, but which allow the determination of local lattice parameters or, for example, a dislocation Burgers vector.

Chou et al. [234] employed an aberration-corrected ETEM to study the dynamics of Si nanowire growth on AuSi and AuAgSi via the vapor-liquid-solid (VLS) route at temperatures between 350 and 450 °C in an atmosphere of $2x10^{-3}$ to $8x10^{-1}$ Pa of Si_2H_6 at close to atomic resolution. Employing the same instrument Panciera et al. studied the incorporation of $NiSi_2$, $CoSi_2$, MnSi nanocrystals formed by changing for a certain time from Si_2H_6 to $M(C_5H_5)_2$ (with M = Ni,Co,Mn, respectively) into growing Si(111) nanowires at 500 °C and took atomically resolving movies of the process at 400 frames per second [235]. Zhang et al. [236] studied the growth of $W_{18}O_{49}$ nanotubes in an ETEM at 700 °C in about 0.1 Pa of oxygen. As substrate they employed a tungsten filament heated by means of a temperature-calibrated electric current flowing through it. Employing lattice-fringe imaging during growth they could provide direct evidence for tube formation by adsorption of WO_3 formed from sublimated W in the oxygen atmosphere. The adsorption leads to atomic steps at the side walls growing along [010].

Yoshida et al. [237,238] studied in an aberration-corrected ETEM under atomic resolution the behavior of [110] oriented cubic gold nanoparticles on CeO_2 acting as catalysts for the oxidation of CO. They found that under 1 vol% CO in air (45 Pa) at room temperature the {100} surfaces of the Au particles undergo a transition to a reconstructed structure, the Au{100}-hex(1x5) structure (Figs. 46a,b). At high magnification, the authors were able to image the adsorbed oxygen atoms and measure the local correlation of the oxygen atoms with the atoms of the hexagonally reconstructed Au surface using quantitative image simulation (compare Fig. 46c, d). These observations provided evidence for a high affinity for CO adsorption on the {100} facets of the nanoparticles as a result of the reconstruction. This was confirmed by *ab-initio* calculations. He et al. [239] combined atomic-resolution electron microscopy in an ETEM with *ab-initio* molecular-dynamics calculations to study the dependence of the CO oxidation reaction on the size of Au nanoclusters. They found that the absorption energy of CO on Au increases steeply with decreasing Au cluster size, that the very small Au particles (<4 nm) under reaction conditions became structurally unstable, and that the density and the motion of Au-CO aggregates play an important role in the reaction rate.

Yuan et al [240] used an aberration corrected ETEM to study the interface between Au nanoparticles and a TiO_2 substrate while this system was used *in situ* for CO oxidation. Heating to 500 °C under oxygen atmosphere (650 Pa) inside the microscope resulted in perfect epitaxy between the Au crystals and the (001) oriented TiO_2 substrate surface with periodically arranged misfit dislocations between perfect interface regions. In this process, as indicated by lattice-fringe high-resolution imaging, Au [111] aligned parallel to TiO_2 [001]. Remarkably, when the atmosphere was changed from pure oxygen to a mixture of 1 part O_2 to 2 parts CO (500 Pa, 500 °C), the nanoparticles rotated around their [111] axis by 9°, perfectly preserving the alignment with TiO_2 [001]. The rotation was found to be reversible, if one brings the CO in and out alternately, the rotation oscillates accordingly. This behavior could be described using DFT and Bader charge calculations, treating the interfacial energy between the Au nanoparticles and the TiO_2 (001) surface at different degrees of the presence of oxygen in the interface. In fact, when the reaction mixture is admitted, the CO molecules consume the oxygen in the interface, and the rotated interface structure becomes energetically more favorable. This work also demonstrates the productive interplay between aberration-corrected electron microscopy and *ab-initio* calculations, which in this particular case allows insight into atomic details that are otherwise hardly accessible.

Koh et al. [241] used NCSI at 80 keV electron energy (i.e., below the value of threshold energy for atomic displacement) to study the oxidation of multiwall carbon nanotubes (CNT) at temperatures from 300 to 520 °C in an aberration-corrected ETEM equipped with a monochromator for the electron beam and an EEL spectrometer. The oxygen pressure in these experiments was 150 Pa. Using the EELS, they were able to demonstrate that oxygen is ionized by decomposition of the O_2 molecule by radiolysis in the electron beam. To prevent this ionization process in the microscope from affecting the results, the beam was switched off whenever oxygen was admitted to the microscope. It was switched on again only after purging the gas from the chamber. Under these conditions it was possible to investigate the “intrinsic” oxidation. It turned out that the oxidation of the CNT always takes place along the length of the outer graphene cylinder and that, in contrast to previous reports, the ending cap remains unaffected. This work shows that, on the one hand, radiation damage from the electron beam in the sample and in the gas or liquid environment can in principle play a role in *in-situ* experiments, but that often this influence on experimental results can be reduced or even avoided altogether by careful management of the experiment. The same applies to *in-situ* investigations of phase transformations and materials plasticity.

The following two papers highlight another aspect relevant to both classical structure electron microscopy and *in-situ* electron microscopy. In oxide materials, working under a moderate oxygen partial pressure can prevent or even reverse the damage caused by electron irradiation. Yuan et al. [242] studied in anatase (TiO_2) nanoparticles (nanosheets of 30 nm lateral and 5 nm thickness dimensions) the transition from unreconstructed (001) surfaces to a (1x4) reconstruction (Fig. 47). Their atomic-resolution ETEM investigations at 500 °C were carried out at an oxygen pressure of $5x10^{-2}$ Pa. Due to the particular dimensions of the nanosheets, they were able to follow the transformation via video directly in the side view and thus also observe the behavior of the atomic layers directly underneath the surface layer. The study was accompanied by *ab-initio* calculations, and many different models for the reconstruction could be tested by transforming the results into image simulations whose results could be compared with the experimental images. The transition from the (1x1) structure occurs via a mixed, fluctuating state where (1x3), (1x4) and (1x5) areas exist side by side or in sequence, with substantial rearrangements in the subsurface layers. Eventually, as depicted in the video frames in Fig. 47a and in the schematic of Fig. 47b, the (1x4) structure forms. These fluctuations explain, why neither STM nor other, non-microscopic techniques were successful to observe the transition. Investigating the role of the oxygen atmosphere, the authors found that it is not at all necessary for the surface phase transformation, but that it is indispensable to prevent damage to the specimen by the electron beam. In fact oxygen desorption by electron irradiation is a classical topic in surface physics [243–245]. In TiO_2,

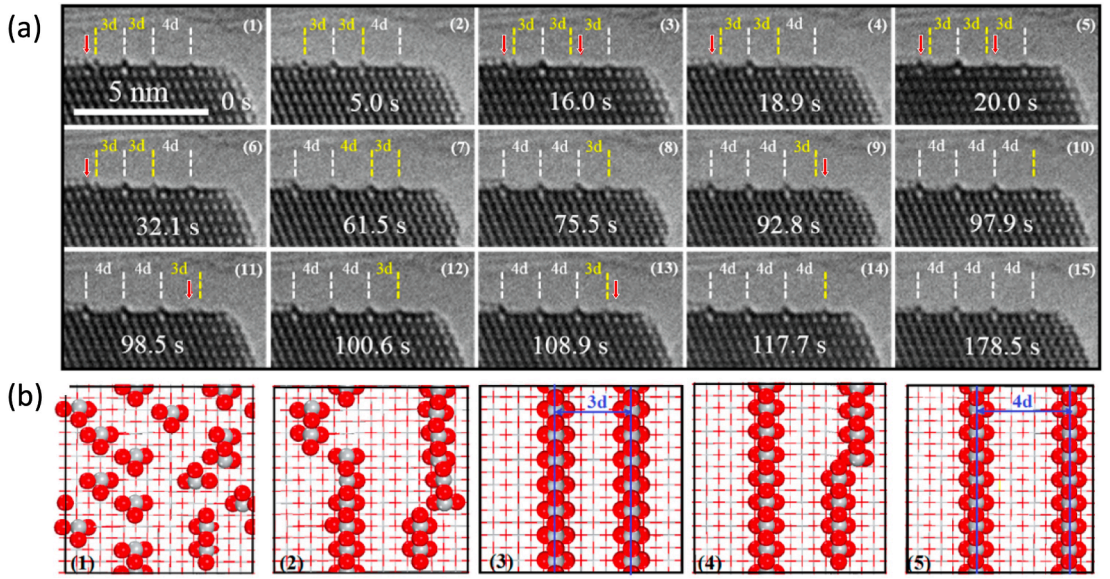

Fig. 47. Evolution of the atomic reconstruction of the (001) surface of anatase, TiO_2, at 500 °C in oxygen ($5x10^{-2}$ Pa) in an environmental electron microscope. (a) Sequential images (taken from a video recording) of the dynamic structural evolution, viewed along the [010] direction. "d" denotes the periodicity of the atomic arrangement of the unreconstructed (1x1) structure on the (001) surface. 4d refers to the final (1x4) reconstruction. The image shows fluctuations, e.g. in frames 2-3-4-5. Red arrows indicate metastable atom configurations. (b) Schematic of the transition seen "from top", i.e. perpendicular to the viewing direction in (a). Reproduced from [242] with permission of American Chemical Society).

electron irradiation creates a core shell hole that is filled via an Auger process involving electrons localized at the oxygen, with the result that the oxygen atom is desorbed. The topic of the 1x4 surface of anatase was recently revisited by Yuan et al. [246]. The authors were able to study *in situ* the structural changes on the surface that occur while TiO_2 is acting as a catalyst for the water-gas shift reaction ($CO + H_2O \rightleftarrows CO_2 + H_2$) inside the ETEM.

Normally, the change in chemical composition of an oxide due to radiolysis caused by the electron beam is a drawback for microscopy. However, a study in which this effect has been exploited for an interesting experiment that is otherwise not so easy to perform is the quantification of the order at the interface between liquid aluminum and sapphire (α-Al_2O_3) by Gandman et al. [247]. The authors prepared $[10\bar{1}0]$ and $[1\bar{2}10]$ oriented sapphire single crystals for observation at atomic resolution employing NCSI in the aberration corrected electron microscope at 300 kV. Making use of their earlier observation of the fact that under an intensive electron beam the sapphire crystals loose their oxygen leaving pure aluminum which above the melting point is liquid, they produced in situ a

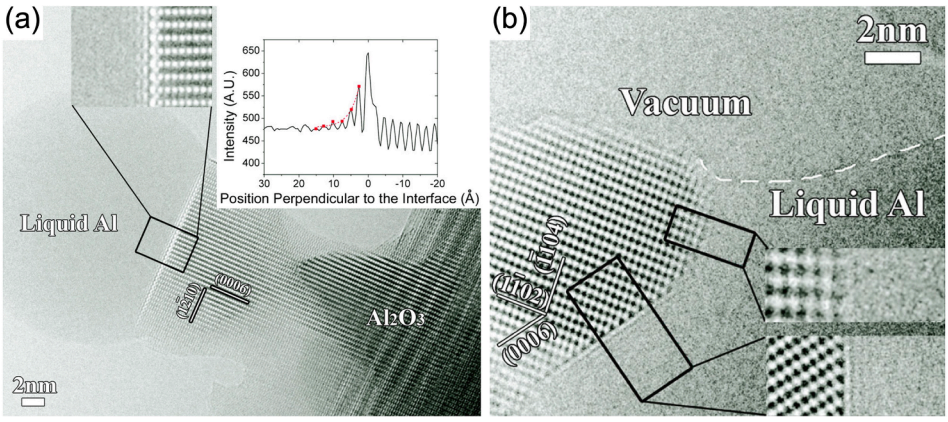

Fig. 48. The interface between a droplet of liquid aluminum and crystalline sapphire (α-Al_2O_3) at 750 °C imaged in NCSI mode. Atoms bright on a dark background. (a) $(1\bar{2}10)$ surface (b) (0006) and a $(\bar{1}104)$ surface. Intensity fringes interpreted as density fluctuations (see line traces in the insets) can be recognized in the liquid. For comparison (see upper part of (b) no intensity fringes occur (in the vacuum) when the sapphire crystal is directly adjacent to the vacuum. This indicates that, in the aberration-corrected instrument, the observed fringe pattern is a physical reality and not due to contrast delocalization. Since contrast delocalization is, as described in the text, unavoidable in an uncorrected microscope, such observations would not be feasible in uncorrected instruments. (Reproduced from [247], Copyright (2013) by the American Physical Society).

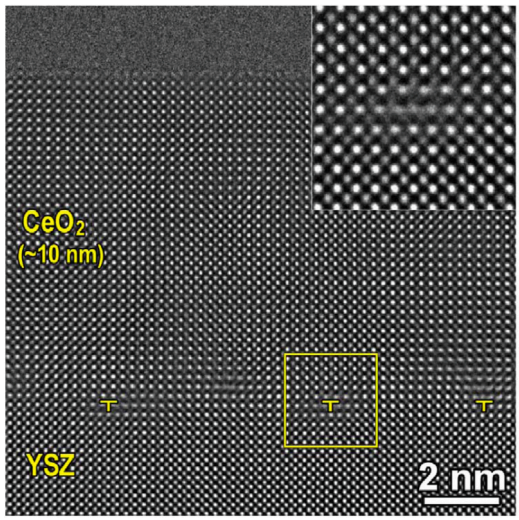

Fig. 49. NCSI of a heterostructure consisting of a ~ 10 nm thick CeO_2 layer on Y-stabilized ZrO_2 (YSZ). Atoms appear bright on a dark background, the cations are the brighter, the oxygen atoms are the weaker image spots. Interfacial dislocations are indicated. The inset on the upper right shows the boxed area (core of a single dislocation) at a higher magnification. (Reproduced from [249] with permission of Elsevier).

well oriented liquid-solid interface. Fig. 48 shows intensity fluctuations in situ in a liquid aluminum droplet at 750 °C in contact with a $(1\bar{2}10)$ sapphire surface in (a), and with a (0006) and a $(\bar{1}104)$ surface in (b), respectively. In agreement with theoretical predictions and earlier experimental results [248] these intensity fluctuations were interpreted as density variations in the liquid "in resonance" with the crystal structure of the sapphire surface. Also a reconstruction of the last (closest to the solid-liquid interface) layer of the $(10\bar{1}2)$ surface could be observed in the form of a substantially larger interplanar distance compared to that in the bulk of the crystal. From a fundamental point of view and thus for more insight into the technique of *in-situ* experimentation, this work contains a very critical point. And this concerns a possibly existing residual contrast delocalization (cf. Eqs. 6, 10, 14), which would lead to the formation of "ghost images" of the crystal structure in the liquid, which could be mistaken for density fluctuations. Since the authors were well aware of this problem, they examined the contrast generation for each of their images by means of computer simulations and a careful determination of the real value of the defocus, which (see Eq. (6)) is a sensitive factor in the magnitude of the contrast delocalization. The contrast delocalization proved to be sufficiently small to ensure that the observed contrast fluctuations in the liquid could indeed be interpreted as density fluctuations. This was supported by the important observation that in the case that the sapphire crystal was immediately adjacent to the vacuum (Fig. 48b), there were no fringes in the vacuum region, which would be expected in the case of contrast delocalization.

Sinclair et al. [249] carried out a high-resolution investigation on the epitaxy of CeO_2 thin films on yttria-stabilized ZrO_2 at 300 keV inside an ETEM that could be operated in CTEM (with an image corrector) and in (uncorrected) STEM mode. Fig. 49 shows by NCSI a cross-section of the heterostructure at atomic resolution, imaged along the [001] direction. Both the cations Zr and Ce and the oxygen are visible. The image shows misfit dislocations in the interface, whose Burgers vector component perpendicular to the viewing direction can be measured directly. The authors found that at moderate beam current densities (~2600 $eÅ^{-2}s^{-1}$) the atomic structure remains stable for tens of minutes, but that at higher beam current densities (about 15,000 $eÅ^{-2}s^{-1}$) an ordered superstructure forms, which, as confirmed by EELS, is related to oxygen vacancy ordering. The formation of oxygen vacancies is accompanied by a reduction of the valence from Ce^{4+} to Ce^{3+}. The authors took advantage of the fact that the investigation was made in an aberration-corrected ETEM to produce an atmosphere of 100 Pa oxygen. Not only did the order structure disappear in this atmosphere, but also its formation could be completely avoided. This investigation also gave evidence for the movement of atoms at the edge of the sample, which is shown in Fig. 50. The authors attributed this to an increase in sample temperature due to the electron beam, because room temperature is much too low for diffusion in the volume and at the surface in CeO_2. However, one could also suggest that the cause of this atomic motion is the irradiation-induced diffusion of atoms (at subthreshold energies) described above, assuming that the atoms are only weakly bound at the sample edge. The motion of atomic contrasts at the edges of atomically resolved samples, e.g. Au [55] and Pt [250], has been observed frequently. Here, the time scale of typically a few seconds between the observed jumps does not fit the known diffusion processes of atoms in the bulk (for a discussion see [124]). According to Arrhenius' law, volume diffusion is associated with jump rates that are generally many orders of magnitude higher [251] and therefore elude observation in the electron microscope. It seems appropriate in this context to point out that also at edges the observed atomic contrast generally originates from a column of

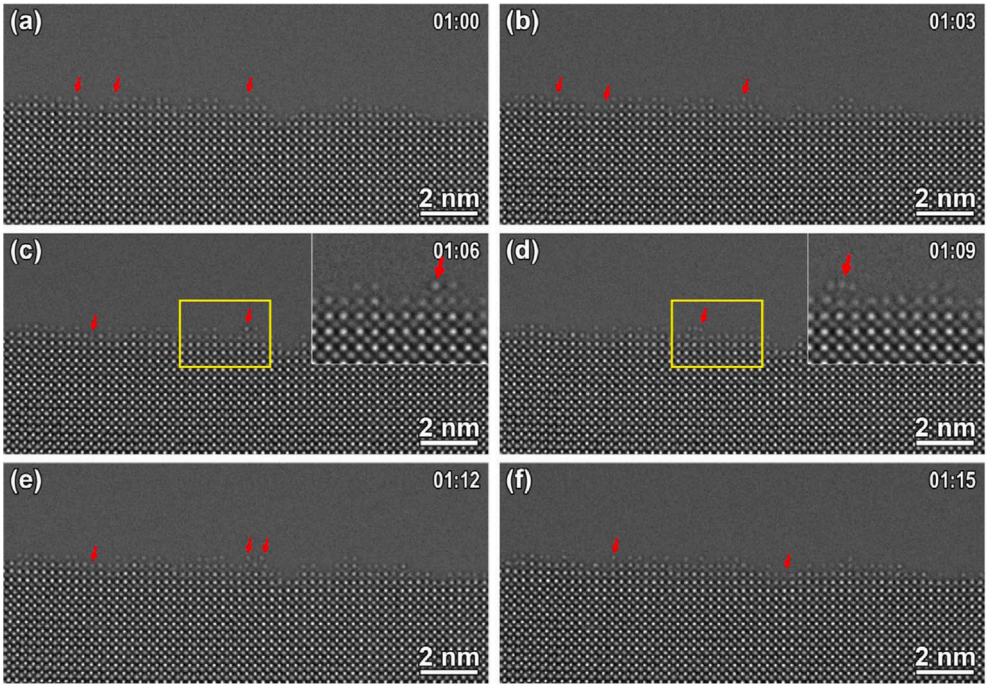

Fig. 50. A sequence of *in-situ* video frames showing the movement of atomic contrasts at the sample edge in CeO_2. The atomic jumps occur approximately every 3 s and their repositioning occurs between individual video frames (0.04 s). Inset in (c) and (d) are high magnification views of the boxed areas in the images showing a single atomic jump. The times in the upper right-hand corner of each frame are minutes:seconds. (Reproduced from [249] with permission of Elsevier).

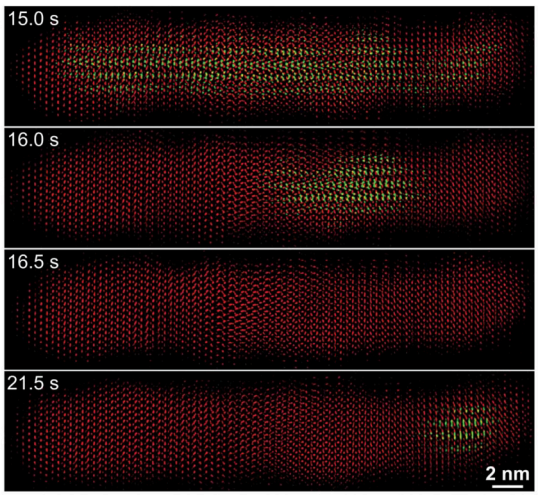

Fig. 51. Time sequence of the structural transformation in a Cu_2S nanorod from the low-chalcocite state (L, green) to the high-chalcocite state (H, red) observed in situ at about 337 K during a very slow temperature rise in the irradiated spot (intentionally induced by the electron beam). Sequential images of the same spot of the nanorod indicate fluctuations between the H and the L state. (Reproduced from [256] with permission from the American Association for the Advancement of Science).

atoms which is imaged end-on. The observed atomic site changes are therefore events where the entire atomic column shifts laterally, which is associated with effective activation energies that are only rather indirectly related to the corresponding atomic parameters[22].

Multivalent transition metal oxides have received special attention in recent years because they offer a wide range of possibilities for attractive device functions related to variable oxygen stoichiometry. Examples are catalytic activity, applications in solid oxide fuel cells, batteries, gas sensors and resistive-switching random access memories and neuromorphic circuits [252]. A prominent model system is $SrFeO_x$ which in the form of epitactic thin films exhibits a reversible topotactic phase transition between conducting perovskite $SrFeO_3$ and insulating brownmillerite $SrFeO_{2.5}$ in a redox process without loosing the lattice framework [253]. Xing et al. [254] studied *in situ* by NCSI the atomistics of the phase transition between perovskite $SrFeO_3$ and brownmillerite $SrFeO_{2.5}$ at 300 °C. This work is of fundamental importance because it demonstrates for the first time that one can use the special precision of NCSI to directly observe and measure diffusion in situ on an atomic scale using the time course of the intensity of the atomic maxima of a particular atomic species, in this case oxygen. Furthermore, this study demonstrates that *in-situ* observations at interfaces, which are not accessible by other techniques, allow for observations of elementary importance to the phase transition process. It turned out that the perovskite phase at the phase interface does not directly change into the stoichiometric brownmillerite phase, but that there first an intermediate state is formed which is hyperstoichiometric with respect to oxygen and has features of the brownmillerite structure. Once this state is developed, oxygen atoms migrate through the fast-oxygen-diffusion channels inherent to this structure involving the local atomic rearrangement of the FeO_4 tetrahedral chains. It is remarkable that the images along the channels show the oxygen atoms in them directly, from which it can be concluded that the diffusion occurs by means of an intersticialcy mechanism. Another exemplary feature of this experiment: the valence of Fe atoms was measured using EELS in the STEM configuration. This demonstrates that the use of double-corrected instruments, which allow both modes of operation, CTEM and STEM, is attractive for *in-situ* experiments. Indeed, the latest generation instruments allow rapid switching between the two operation modes without losing the alignment of the microscope. This allows the respective advantages of the two modes to be used in tandem for material investigations.

An atomic resolution electron microscope is also a useful tool to study size-effects in first-order phase transitions, see, e.g. [255]. Since in nanoscale dimensions the nucleation threshold becomes lower with the size of the system, this opens the possibility to study fluctuations between the initial and the final structure in nanoparticles. An example is the study by Zheng et al. [256] on the kinetics of the transformation from the low-temperature phase (low-chalcocite) to the high temperature phase (high-chalcocite) in Cu_2S. Both phases are characterized by a high degree of complexity and it has been shown that the high-temperature phase is a hybrid phase in which a quasi-liquid anion sublattice coexists with a crystalline cation lattice. The phase transition at 376 K is of first order in the thermodynamic limit. In this study, it was possible for the first time to investigate it *in situ* under atomic resolution conditions. For this the authors exploited the fact that, due to the size effect, in Cu_2S nanorods the phase-transition temperature is 39 K lower, and due to the low thickness of the nanorods, the phase transformation can be directly observed by NCSI. The temperature increase necessary for this purpose was produced by means of irradiation by the 80 keV electrons used for imaging (the electron energy was reduced in order to exclude atomic displacement damage). In this way, while the temperature was slowly increased (and also decreased again) by changing the beam current density, it was possible, as shown in Fig. 51, to observe and study for the first time during a transition period reversible fluctuations between the two phases.

Another investigation where the electron beam was employed as a stimulus to study reactions under conditions providing access to processes normally too fast to be observable is due to Wei et al. [257,258]. In $PbZrO_3$ heat-treated at temperatures above the transition temperature and then cooled in oxygen to introduce both lead vacancies and oxygen the authors studied the impact of the complex defect and domain structure on the phase transition from the antiferroelectric state via an antiferrodistortive-to-ferrodistortive state to the ferroelectric state occurring during electrostatic energy storage. Here the 300 keV electron beam was used for two purposes, to increase by atomic-defect formation the atomic mobility in the system and to deposit electrostatic energy by electric charging in the interaction with the electron beam. The dynamic study carried out at the atomic level employing the NCSI technique unveiled the unit-cell-scale pathway for electrostatic energy storage.

Experiments in the electron microscope on plastic deformation of metals can be considered as a classical field of *in-situ* electron microscopy since Saka and Imura (e.g. [218]) demonstrated and measured the dynamics of dislocation sources (e.g. the Frank-Read source), dislocation motion and dislocation interaction using video recordings in the Osaka University high voltage electron microscope (in Bragg-Diffraction contrast) in the seventies. Already at that time it was clear that such experiments as model experiments can contribute a lot to the basic understanding of the plasticity of crystals, but that due to the fact that they are experiments in very thin films, the results of the measurements are not easily applicable to a quantitative understanding of plasticity in the bulk. For a recent brief review of *in-situ* plasticity experiments employing aberration-corrected instruments we refer to [259]. As an example we select here the study of crack propagation during tensile deformation of tungsten crystals at 700 °C carried out by Zhang et al. [260]. Fig. 52 shows in (a) a low-magnification overview at the moment when a crack just starts to form in the thin-foil sample. In (b), taken at higher magnification, the crack tip can be recognized in the upper left corner. Crossed lattice fringes can be seen. Due to the high local mechanical stress, the fringe patterns are severely disturbed. The insets on the right-hand side show diffractograms taken in the framed blue and red areas I and II, respectively. They were identified as to belong to a $[100]_{BCC}$ zone axis (blue) and to a $[110]_{FCC}$ zone axis. This is interpreted as a bcc to fcc structural transformation in the high stress field at the crack tip. (c-f) show the same spot of the sample (white boxed area in (b)) at successive times during further straining at a rate of 1 $Å s^{-1}$. In (f) the crack has arrived in this spot. This

[22] Because of the high pre-exponential factor in the Arrhenius relation, of the order of $10^{12} s^{-1}$, the increase from very low jump-rate values to very high values, both of which are not accessible to electron microscopic observation, is extraordinarily steep. The probability of coincidentally being with the sample temperature in the steep rise at a jump rate of a few jumps s^{-1} is very low (see also [124]).

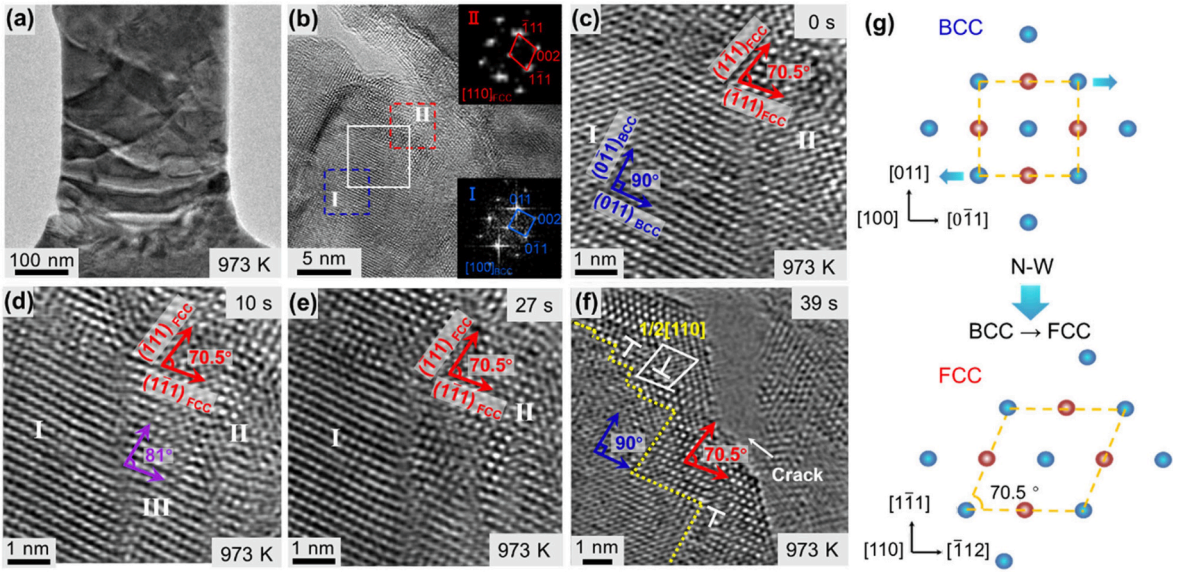

Fig. 52. Thin tungsten sample during tensile testing inside the electron microscope at 700 °C. (a) Low-magnification overview at the moment when a crack just starts to form at the lower left. (b) Image taken at higher magnification along the $[100]_{BCC}$ orientation. The crack tip can be recognized in the upper left corner. Crossed lattice fringes can be seen. Due to the high local strain, the fringe patterns are severely disturbed. The insets on the right-hand side show diffractograms taken in the framed blue and red areas "I" and "II", respectively. They were identified as to belong to a $[100]_{BCC}$ zone axis (blue) and to a $[110]_{FCC}$ zone axis, indicating a bcc to fcc structural transformation in the high stress field at the crack tip. (c-f) show the same spot of the sample (white boxed area in (b)) at successive times during further straining at a rate of 1 $Å s^{-1}$. In (f) the crack has arrived in this spot. Dislocations are indicated at the boundary (dotted yellow line) between bcc and fcc structure. (g) Schematic of the mutual crystallographic orientation relationship of the bcc and fcc phases. (Reproduced from [260]; licensed under Creative Commons Attribution 4.0).

work demonstrates ductile plastic deformation involving among other things a bcc to fcc structural transition in the high stress region at the crack tip, corroborating similar observations reported earlier in molybdenum likewise in thin microscopic foils [261].

The *heating of the sample* in the irradiated area or, as a whole, due to the heat dissipation of the electron beam is a complex problem [16,262,263]. Due to the small thickness and the usually very favorable geometry of the heat dissipation away from the irradiated spot, the temperature increases are generally rather low, in the range of a few degrees at most. However, if the thermal conductivity of the specimen material is poor, and especially if the thermal coupling of the specimen to the specimen holder is inadequate, the temperatures can reach high values. Therefore, estimating or measuring the temperature prevailing at the site in the specimen where a reaction occurs is an important problem in *in-situ* electron microscopy. For this the observation of phase transformations whose critical transformation temperature is known or the measurement of the temperature-dependent lattice parameter in quantitative diffraction experiments performed for this purpose is suitable. Spiecker et al. [264,265] have developed a very accurate method to measure the temperature in the irradiated spot based on the measurement of the lattice parameter in gold nanoclusters. Tests in the context of *in-situ* heating experiments showed that the precision of the temperature measurement in the range from room temperature to 890 °C is better than 3 °C.

We have briefly described above the two basic damage mechanisms by the electron beam, radiolysis and atom knock-on damage. For the nature of the effect of the damage, it is important to distinguish the primary process from the secondary processes occurring afterwards. In radiolysis, secondary processes include the movement of formed radicals or the decay of electronic excitations. In atomic displacement damage, the secondary processes are generally associated with the diffusion of interstitial atoms and vacancies. In both groups of secondary processes, the sample temperature is an important parameter. In electron cryo-microscopy in biological structure research, lowering the sample temperature down to the temperature of liquid nitrogen (77 K), has resulted in a significant increase in the tolerated electron dose for many materials and (according to the Rose criterion, see Section 5.2) a corresponding increase in resolution. In recent years, a number of research groups have undertaken to apply the methods used so successfully in electron cryo-microscopy in structural biology to materials research. One outstanding area is research into the compounds of lithium, which play an important role in modern battery technology. Li et al. [266] developed a workflow for the preparation of Li compounds using a plunge-freeze technique with liquid nitrogen. The specimen is then mounted under nitrogen in the liquid-nitrogen cooled specimen holder and transferred to the microscope without warming the specimen or exposing it to air. By evaporating lithium in vacuum, they deposited Li nanocrystals on carbon films and then covered them with typical battery electrolytes. They preserved this with the plunge-freeze technique to study the growth of the nanocrystals in the electrolyte *in situ* in the microscope. In this experiment they were able to successfully image the Li crystals along the <111> direction at atomic resolution using NCSI at a dose rate of 1000 $eÅ^{-2}s^{-1}$. This demonstrates high stability of lithium metal at liquid-nitrogen temperature under the electron beam. For the preparation of Li compounds for cryo-electron microscopy, the cryogenic focused ion beam (CFIB) device is now widely used in conjunction with a cold air-lock transfer [267]. A recent review on the progress achieved in the field of battery research by application of cryogenic techniques

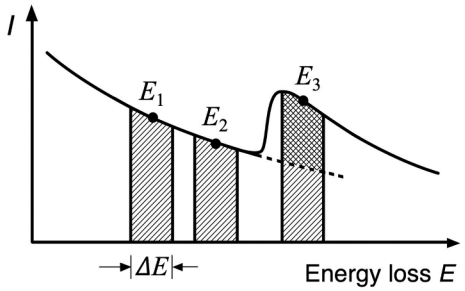

Fig. 53. Schematic illustrating the three-window technique in energy-filtered transmission electron microscopy (EFTEM) at an energy-absorption edge (see text). I is the intensity. ΔE denotes the width of the energy window of the spectrometer. E_1, E_2 and E_3 denote the central energy-loss value (center-window energy) of the respective image. The cross-hatched area represents the element-specific signal characterizing the absorption edge.

in the electron microscope is given in [268].

Although pure radiation damage experiments are rarely a topic nowadays, there are studies in which the formation of defects in graphene and their further development under the electron beam as well as the migration of doping atoms and doping atom clusters were observed *in situ* (see, e.g. [32,269]). Finally, we would like to note that also *in-situ* electron microscopy is a prominent example of the fact that aberration-corrected electron microscopy is successfully used in conjunction with molecular-dynamics and DFT calculations of the electronic and atomic structure. This shows that the two methods serve the same size scale and that electron microscopy can provide a good starting point for the *ab-initio* calculations, thus limiting the large parameter range for the elaborate calculations from the outset.

8. Energy-filtered transmission electron microscopy (EFTEM)

Energy-filtered transmission electron microscopy (EFTEM) is a technique in CTEM that images a specimen using inelastically scattered electrons that have undergone specific energy losses within the specimen [270–274]. By selecting energy windows that cover a range of energies pertinent to inner-shell ionization of elements present in the sample, it is possible to obtain chemical maps and bonding information of the different atomic species. The prerequisite for EFTEM is an imaging electron filter consisting of an electron spectrometer and the optics to produce and focus the image on a camera. Today, post-column filters are commonly used mounted underneath the microscope.

The basis of EFTEM is EELS. This means that the intensity of the electrons that have experienced a loss of slightly higher than a particular ionization energy value is used as a measure of the relative concentration of the chemical element. As is common with EELS the element-specific signal $I^{\mathrm{es}}(E,x,y)$ at energy loss E occurs on a very intense unspecific background $I^{\mathrm{b}}(x,y)$ that needs to be separated. A frequently employed method by which this is done is the three-window technique [17,270,275]. As shown in Fig. 53, two pre-edge images are taken with the intensity distribution $I_1(E_1,x,y)$ und $I_2(E_2,x,y)$ formed by electrons that have experienced the (unspecific) energy losses E_1 and E_2, respectively. Now the assumption is made that I_1 and I_2 are pure background and that the local variation of this unspecific intensity distribution is the same in a third image whose intensity distribution is given by

$$I_3(E_3,x,y) = I^{\mathrm{es}}(E_3,x,y) + I^{\mathrm{b}}(E_3,x,y), \tag{37}$$

where the functional dependence of the background intensity follows a power law of the form

$$I^{\mathrm{b}}(E,x,y) = AE^{-B} \tag{38}$$

and where the coefficients A and B are determined by fitting to I_1 and I_2 [17,270]. Subtracting I^{b} from I_3 yields the element specific signal intensity (per pixel). The directional distribution of core-loss scattered electrons is strongly forward directed so that the fraction of scattered electrons entering the spectrometer and contributing to the image is high. However, since the quantum physical effective cross section for core loss scattering is very small, the EELS technique basically suffers from a low signal-to-noise ratio. The latter increases (within certain restrictions) with the width of the energy window ΔE [276]. However, this is at the expense of optical resolution, because the chromatic aberration causes a change in the focal length of the objective lens of $Z_{\Delta E} = C_{\mathrm{c}}\Delta E/2E_0$, where E_0 is the energy of the incident electron beam [16,59]. Because of these competing effects, the width of the energy window in optically uncorrected instruments is limited to typically 10 to 20 eV and the optical resolution of the energy-filtered images is limited to at best about 4 Å [271,277,278]. The situation is entirely different in CTEM involving an objective lens corrected for both spherical and chromatic aberration. Experimental measurements carried out on the TEAM instrument equipped with the $C_{\mathrm{S}}/C_{\mathrm{C}}$ corrected CEOS C-COR objective lens demonstrated for $E_0 = 200$ keV and - 200 eV $\leq \Delta E \leq$ 200 eV a negligible value of defocus [59,279].

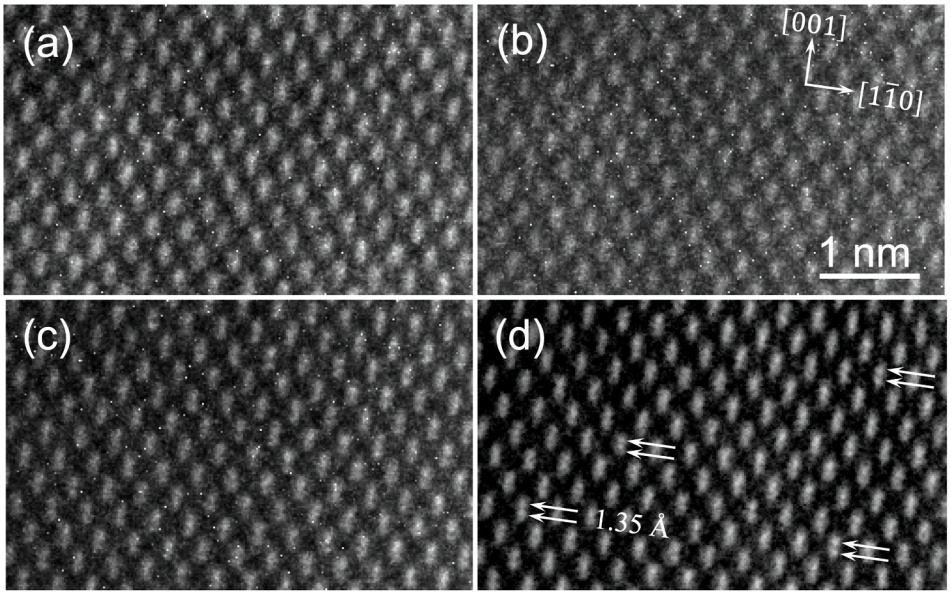

Fig. 54. EFTEM images used to construct the Si $L_{2,3}$ map by means of the three-window technique in the chromatic- and spherical-aberration corrected electron microscope (PICO, NCSI mode at 300 keV; $C_S = -8$ µm, $Z = 4$ nm). Viewing direction [110]. Edge onset at 100 eV. All images were taken using a 40 eV wide energy window. (a) Pre-edge image 1 centered at an energy loss of 55 eV. (b) Pre-edge image 2 centered at 75 eV. (c) Post-edge image 3 centered at 120 eV. (d) Resulting atomic-resolution intensity distribution, after background subtraction. The Si dumb-bell atom pair separation of 1.35 Å is resolved (arrows). A standard average image background-intensity subtraction filter was applied. As of today, this marks the record spatial resolution of EELS-related imaging. (Reproduced from [280], Copyright (2013) by the American Physical Society).

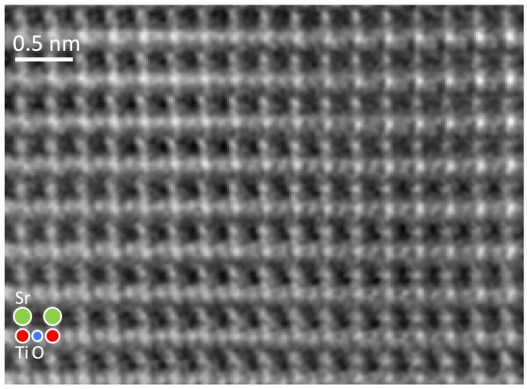

Fig. 55. PICO EFTEM image along the [110] crystallographic direction of $SrTiO_3$ employing electrons that have experienced a Ti $L_{2,3}$ energy loss (edge onset at 458 eV) in the chromatic- and spherical-aberration corrected electron microscope. Background subtraction was carried out using the power-law technique on the basis of a series of images taken in 10 eV energy steps between 390 eV and 560 eV at a window width of 25 eV. (NCSI mode at 200 keV; $C_S = -6$ µm, $Z = 3$ nm). (Reproduced from [281] with permission of Elsevier).

Fig. 54 shows the resolution of the dumb-bell atom pairs in [110] oriented silicon in the Jülich C_S/C_c corrected PICO instrument, operated at 300 keV[23], employing electrons that have suffered a Si $L_{2,3}$ core loss [280]. The onset of the corresponding ionization edge is at 100 eV [271,273]. The three-window technique was employed with $E_1 = 55$ eV, $E_2 = 75$ eV and $E_3 = 120$ eV and $\Delta E = 40$ eV. The resolved 1.35 Å atomic distance marks the current record lateral resolution in EELS based imaging in the electron microscope. Fig. 55 displays a likewise background-subtracted image of [110] oriented $SrTiO_3$ employing electrons that have experienced a Ti $L_{2,3}$ energy loss [281]. The edge onset is at 458 eV. In this case, in order to obtain more accurate data regarding the background, a series of images was taken in steps of 10 eV with an energy window of width 25 eV in the range of 390 eV to 560 eV. Background subtraction

[23] In order not to lose the optical adjustment of the microscope for the electrons of energy E_0, the acceleration voltage of the microscope is increased for each image such that after the energy loss of (see Figure 53) E_1, E_2, E_3, respectively, the resulting energy of the imaging electrons is again at E_0.

was then caried out fitting the pre-edge intensities to a power law. The Ti $L_{2,3}$ loss image shows the whole $SrTiO_3$ lattice (compare e.g. Fig. 5). Quite obviously the peaks in intensity in the image do not correspond directly to the location of the elements whose ionization we are considering. In order to understand atomic-resolution EFTEM images two phenomena have to be considered and treated quantitatively in the accompanying image simulations. These are the "delocalization" of the transition potential, and the "preservation of elastic contrast".

The interaction between an imaging electron with an energy of several tens to several hundreds of kiloelectronvolts and an inner-shell electron bound to an atom, in which a sufficiently high energy is transferred to induce an ionization event, extends over a certain distance. This means that the cross section for core-shell ionization is substantially wider than the extension of the corresponding bound-electron cloud and it is extended over atomic nearest neighbor distances. As a result an imaging electron channeling down an atomic string still interacts sufficiently strongly with a core-shell electron in an adjacent atomic string to ionize it. This is physically described by a transition potential that is *delocalized*.

Qualitatively the *phenomenon of preservation of elastic contrast* can be understood as follows. As described in Section 4.3 illumination of a crystal by a parallel electron beam leads, as a result of the interaction with the periodic scattering potential, to a Bloch-wave field as solution of the Schrödinger equation inside the crystal. The corresponding oscillatory electron motion down the atomic strings is described in terms of electron diffraction channeling [95]. Now let us assume that one of the electrons of this group of channeling

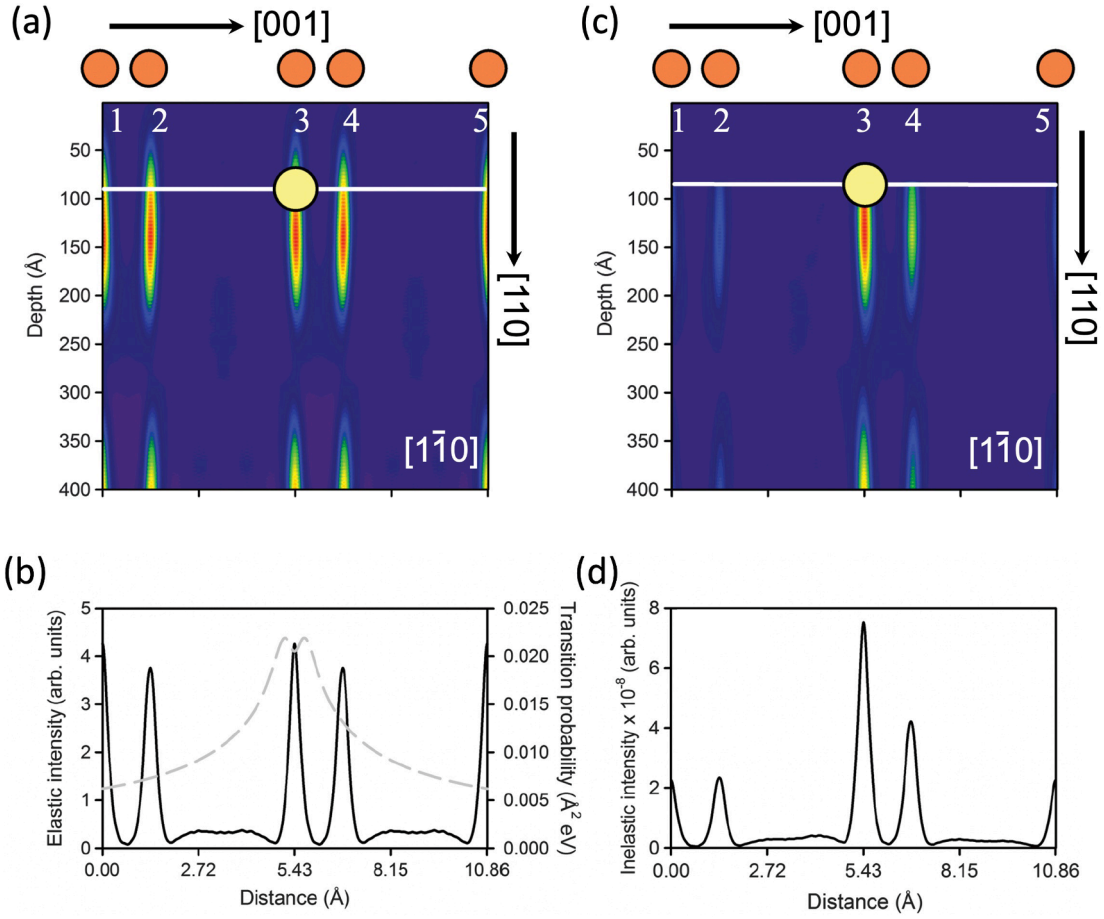

Fig. 56. Electron current density distribution inside a silicon crystal (300 keV). [1$\bar{1}$0] projected dumb-bell atom pairs shown at the top (red circles) and indicated by numbers underneath. Intensity distribution along the [110] viewing direction in Fig. 54 projected onto the (1$\bar{1}$0) plane. The top surface of the specimen is at depth value 0, the exit surface is at 400 Å. (a) Elastic intensity exhibiting electron diffraction channeling behavior (compare Fig. 7), the maximum intensity at the atom positions occurs at a depth of $\xi/2 \approx 130$ Å . The onset of the following maximum at $3/2\,\xi \approx 390$ Å can also be seen. (b) Line scan of the intensity distribution at a depth of 80 Å (horizontal white line in (a)). Note that the intensity of the right-hand partner (atoms "2" and "4) of the dumb bell is slightly lower compared to the left-hand one (atoms "1" and "3") since the former (seen from the entrance surface) is situated at higher depth. The transition probability $|H_{n,0}|^2$ for the inelastic transition $(l = 1, m_l = 0) \rightarrow (l' = 0, m_{l'} = 0)$ is shown as dashed grey line. (c) Intensity of the inelastic wave as a function of depth. The inelastic scattering event occurred at atom "3" at a depth of 80 Å. Comparison of (c) with (a) shows that the intensity distribution of the wave describing the behavior of the inelastically scattered electrons is similar to that of the elastic wave field. (d) Shows the convolution of the elastic intensity depicted in (b) and the transition probability. (Reproduced from [280], Copyright (2013) by the American Physical Society).

electrons interacts inelastically with a core-shell electron of one of the atoms in the atom string. In a plane (the x,y plane) perpendicular to the propagating electrons channeling along the z direction, the probability that such an inelastic event occurs is proportional to the local electron current density distribution, and it is therefore peaked at the atom positions. In other words, if we would plot the probability density for inner-shell ionization in the x,y plane, this would resemble an image of the atomic structure. Now take any of the corresponding inelastically scattered electrons (which will later be selected by the spectrometer to contribute to the image). Since the ionization energy of typically a few tens to a few hundred electronvolts is very small compared to the energy of the incident electrons the corresponding scattering angle involved in the inelastic event is very small too (we have intraband scattering [e.g. [16]). As a result the inelastically scattered electron will stay essentially "within the channel" it was in before it was inelastically scattered. This means that the inelastically scattered electrons are described by a Bloch-wave field rather similar to the wave field that described the electrons before the inelastic scattering event happened. This means that the lattice structure is *imprinted* on the Bloch-wave field (diffraction channeling pattern) before the inelastic scattering, it is *imprinted* in the same way on the x,y-pane probability-density distribution for inelastic scattering to occur, and it is *imprinted* in the channeling of the inelastically scattered electrons down the sample to the exit surface. The resulting fact that an image taken with inelastically scattered electrons resembles the image taken with unscattered electrons is called *preservation of elastic contrast* [282,283].

To understand the complex physics and electron optics underpinning the formation of the intensity distribution in an EFTEM image it is necessary to model both the elastic and the inelastic scattering of the high-energy electrons in the specimen. Detailed treatments are given in [284,280,281]. If the wave function associated with the imaging electrons prior to ionization at depth z is $\psi_0(\boldsymbol{r}_\perp, z)$, the wave function for the inelastically scattered electrons is given by

$$\psi_n(\boldsymbol{r}_\perp, z) = \frac{2\pi m}{\mathrm{i}h^2 k_n} H_{n,0}(\boldsymbol{r}_\perp)\psi_0(\boldsymbol{r}_\perp, z), \tag{39}$$

where k_n is the wave number of the imaging electron having lost the energy ε_n in exciting the crystal to state n (with the crystal electron ionized), $\boldsymbol{r}_\perp$ is the transverse coordinate of the fast electron and $H_{n,0}(\boldsymbol{r}_\perp)$ is the transition potential between the ground state 0 and the excited state n of the crystal, projected in the beam direction. The modulus squared of the transition potential gives the probability of that transition occurring [285,286]. Results of the detailed treatment of the [110] imaging at 300 keV of silicon employing Si $L_{2,3}$ core loss electrons are depicted in Fig. 56. In (a) this figure shows the electron current density distribution as a function of depth for the imaging electrons prior to inelastic scattering and in (c) for the inelastically scattered electrons [280]. The imaging electrons show electron diffraction channeling behavior with maxima of the electron current density at the atom strings (cf. Figs. 7,8). The channeling behavior is also evident from (b) showing an intensity line trace taken at a depth of 80 Å (white horizontal line in (a)). In (b) also the transition probability $|H_{n,0}|^2$ for the inelastic transition characterized by quantum numbers $(l = 1, m_l = 0) \rightarrow (l' = 0, m_{l'} = 0)$ occurring at atom "3" is depicted as a grey line. In (c) the ionization event has now indeed occurred at atom "3" at a depth of 80 Å. Plotted is now (starting at 80 Å) the intensity of the inelastic wave describing the electrons that have triggered core-shell electron excitation at atom "3" suffering the corresponding energy loss. Since (as shown in (b)) the transition probability is maximum for electrons moving on the atom string containing atom "3" the intensity exhibits a maximum just beneath atom "3". However, as can be recognized by finite intensity, core-shell ionization at atom "3" was also induced by electrons channeling down parallel atom strings, e.g. the strings that contain atoms "2", "4" or "5" albeit with a reduced transition probability. This means that an image taken by filtering out the

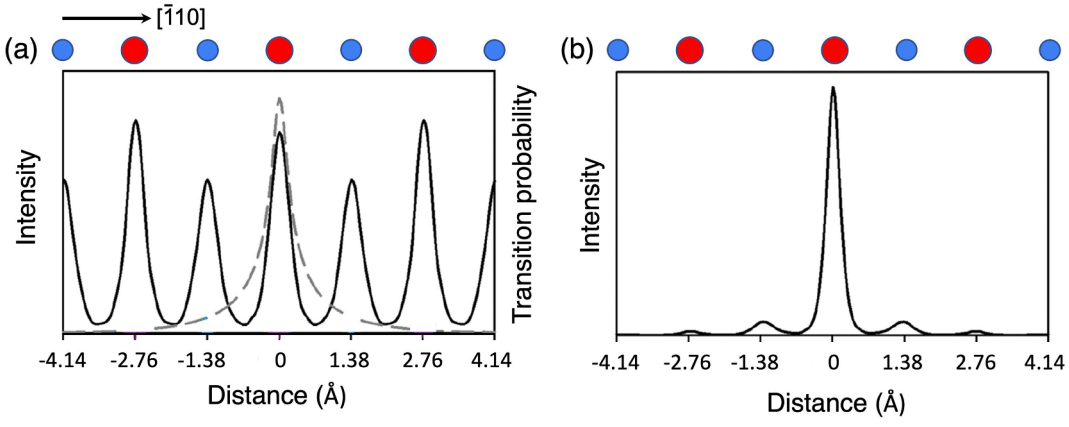

Fig. 57. Intensity (electron-current density distribution) at 200 keV inside a $SrTiO_3$ crystal. [110] projected [1̄10] O-Ti-O-Ti-O-Ti-O atom row shown at the top (Ti: large filled red circles, O: small filled blue circles). (a) The solid (black) line shows the intensity of the elastic wave (the imaging electron wave) prior to inelastic scattering at a depth of 83 Å. The dashed (grey) line shows $|H_{n,0}|^2$, the transition probability for the inelastic transition $(l = 1, m_l = 0) \rightarrow (l' = 2, m_{l'} = 0)$. (b) Intensity of the inelastically scattered wave created in the ionization event. It is peaked at the Ti-atom row on which the excited atom is sitting. However, due to the delocalization of the transition potential also the imaging electrons channeling along the O-atom columns on either side of the Ti-atom column induce an ionization event on this Ti-atom column. (Reproduced from [281] with permission of Elsevier).

electrons that have experienced an energy loss due to ionization of atom "3" would show an intensity distribution as depicted in (d) showing the overlap (convolution) of the elastic intensity and the transition probability of (b). Of course there are similar events for all Si atoms horizontally and vertically in the atomic rows along the z-direction. The total inelastic intensity at the exit surface of the specimen is the incoherent sum of all these events of which we have here, for simplicity, only considered a single one. This is again a demonstration of *preservation of elastic contrast*.

Fig. 57 shows the results of the calculation of the electron intensity for the imaging of $SrTiO_3$ employing electrons that have suffered a Ti $L_{2,3}$ energy loss [281]. (a) shows the intensity distribution (line trace) along a $[\bar{1}10]$ crystallographic direction. Due to electron diffraction channeling it is peaked at the oxygen (small symbols) and titanium atoms (large symbols). The dashed line also shows $|H_{n,0}|^2$, the transition probability for the inelastic transition $(l = 1, m_l = 0) \rightarrow (l' = 2, m_{l'} = 0)$. (b) depicts the intensity of the inelastic wave created in the ionization event of a Ti atom at position 0. It is peaked at the Ti-atom row on which the excited atom is sitting. However, due to the delocalization of the transition potential also the imaging electrons travelling along the O-atom columns on both sides of the Ti-atom column can induce an ionization event for an atom in the Ti-column. Again, the total inelastic intensity at the exit surface of the specimen is the incoherent sum of all these events. This clearly indicates that as a result of the delocalization of the interaction potential for a given inelastic transition the image in Fig. 55 is not a true chemical map. Only through detailed simulations can one understand how the features of the image correspond to local specimen composition. The Si $L_{2,3}$ (with $\Delta E = 100$ eV) transition potential is substantially broader compared to that for the Ti $L_{2,3}$ ($\Delta E = 458$ eV) transition. Although this improves the possibility to obtain more specific chemical information for higher nuclear-charge elements, the potential of EFTEM with atomic resolution can only be exploited if the experimental work is always accompanied by detailed quantitative image simulations.

9. Conclusions

We have provided a review of the fundamentals and materials science applications of atomic-resolution aberration-corrected conventional transmission electron microscopy. The purpose of this review was threefold: First, to remedy the fact that, although there is literature on aberration-corrected optics, there has up till now not been an introduction to working with this technique for the potential user. This introduction concerns in particular the handling and understanding of the practical and theoretical procedures, both of which must be mastered in order to perform microscopy in *quantum physical dimensions*. It is one of the contradictions with which atomic electron microscopy has to live, that every student learns in the beginner's lectures at university that the quantum physical world cannot be intuitively understood, but then the (at times) seemingly simple images of the electron microscope seduce the observer to ignore this warning and to regard these images as being as immediate and thus intuitively understandable as if they were obtained in a light microscope. Our aim was to give the beginner in electron microscopy as well as the user of electron microscopic images in atomic dimensions access to this field, the technical details of which are otherwise hidden in a specialized literature that is now almost impossible to survey. Secondly, we wanted to describe the techniques which have only become available since the introduction of optical aberration correction and which are not yet treated in the classical textbooks on electron microscopy. In particular this concerns NCSI, i.e. imaging under negative-spherical aberration conditions. We addressed both the scientists who are interested in the highest possible precision of measurements in picometer dimensions and the less ambitious users who are only interested in qualitative studies and who, by means of one of the numerous simulation programs, want to get an idea of which imaging conditions they have to set in order "to see" atoms without wanting to measure them. This twofold goal required compromises, which we have also made under the aspect that possibly the one, more theoretically interested, finds too little to read, and the other, more practically interested, would rather do without one or the other detail. On the other hand, we are convinced that especially for a technique like electron microscopy in atomic dimensions, which is basically quite complex but has a wide application potential with respect to its results, a presentation that is readable for both sides is needed. Thirdly, this review tried to show the reader the possibilities but also the limitations of atomic electron microscopy by a concise compilation of examples of its application. At this point, we would like to point out that we are well aware that many of the material science problems given here as examples are also investigated with STEM, and we often regretted during the compilation of this publication that we could not include the wonderful STEM results here. But this review should be limited to CTEM, not least because a comprehensive account of this technique seems long overdue.

One of the authors of this paper wrote an invited commentary article in 2009, just over 10 years after the first paper on genuine atomic resolution in aberration-corrected electron microscopy was published, entitled "Is science prepared for atomic resolution electron microscopy?" [22]. It is worthwhile now, on the silver jubilee of aberration correction, to reflect again on the answer to this question. A careful observer of the scene may then wish to point out that atomic resolution electron microscopy is still under obligation to provide evidence of the high quality of its results in the fields to which it hopes to contribute. Still the possibilities of picometer electron microscopy are poorly known outside the professional electron-microscopy circles, and the results of measurements in the picometer range, which define an entirely new category compared with what was possible in the old days of electron microscopy, are all too often viewed with reserve. In fact, atomic electron microscopy shares with almost all high-level, involved measurement methods in physics the problem that working with these methods and interpreting the results require a large amount of specialized knowledge that is difficult for the layman to access. On the other hand, in most cases the results obtained with the special methods are not an end in themselves, but in the general case they are supposed to contribute something to a subject area, into which the results of many methods flow simultaneously. It is then always the task of the specialists to make their results understandable to the non-specialists. In this sense, this review is also intended as a bridge-building exercise in an idealistic sense.

Declaration of Competing Interest

The authors declare that they have no known competing financial interests or personal relationships that could have appeared to influence the work reported in this paper.

Data availability

Data will be made available on request.

Acknowledgments

The authors are grateful to Prof. Leslie J. Allen, Prof. Rafal E. Dunin-Borkowski and Prof. Joachim Mayer for stimulating and clarifying discussions regarding details of the topics addressed in this review.

References

[1] Knoll M, Ruska E. Beitrag zur geometrischen Elektronenoptik I. Ann Physik 1932;12:607–40.
[2] Knoll M, Ruska E. Beitrag zur geometrischen Elektronenoptik II. Ann Physik 1932;12:641–61.
[3] Knoll M, Ruska E. Das Elektronenmikroskop. Z Physik 1932;78:318–39.
[4] von Ardenne M. Das Elektronen-Rastermikroskop. Theoretische Grundlagen. Z Physik 1938;109:553–572.
[5] von Ardenne M. Das Elektronen-Rastermikroskop. Praktische Ausführung. Z techn Physik 1938;19:407–416.
[6] Abbe E. On New Methods for Improving Spherical Correction, applied to the Construction of Wide-angled Object-glasses. J Roy Micr Soc 1879;II:812–24.
[7] Scherzer O. Über einige Fehler von Elektronenlinsen. Z Physik 1936;101:593–603.
[8] Scherzer O. Sphärische und chromatische Korrektur von Elektronenlinsen. Optik 1947;2:114–32.
[9] Hawkes PW. Aberration correction past and present. Phil Trans R Soc A 2009;367:3637–64.
[10] Rose H. History of direct aberration correction. Adv Imaging Electron Phys 2008;153:1–37.
[11] Urban KW. In quest of perfection in electron optics: A biographical sketch of Harald Rose on occasion of his 80th birthday. Ultramicroscopy 2015;151:2–10.
[12] Urban KW, Rose H. Reply to L.M. Brown et al. "Brief history of the Cambridge STEM aberration correction project and its progeny" in Ultramicroscopy 157, 88 (2015). Ultramicroscopy 2016;161:1–2.
[13] Haider M, Uhlemann S, Schwan E, Rose H, Kabius B, Urban K. Electron microscopy image enhanced. Nature 1998;392:768–9.
[14] Haider M, Rose H, Uhlemann S, Schwan E, Kabius B, Urban K. A spherical-aberration-corrected transmission electron microscope. Ultramicroscopy 1998;75:53–60.
[15] Dellby N, Krivanek OL, Nellist PD, Batson PE, Lupini AR. Progress in aberration-corrected scanning transmission electron microscopy. J Electron Microsc 2001;50:177–85.
[16] Reimer L, Kohl H. Transmission Electron Microscopy. 5th edn. Springer; 2008.
[17] Williams DB, Carter CB. Transmission Electron Microscopy. 2nd edn. Springer; 2009.
[18] Spence JCH. High Resolution Electron Microscopy. 4th edn. Oxford University Press; 2013.
[19] Rose H. Geometrical Charged-Particle Optics. 2nd edn. Springer; 2012.
[20] Erni R. Aberration-Corrected Imaging in Transmission Electron Microscopy: An Introduction. 2nd edn. Imperial College Press; 2015.
[21] Urban KW. Studying atomic structures by aberration-corrected transmission electron microscopy. Science 2008;321:506–10.
[22] Urban KW. Is science prepared for atomic resolution electron microscopy? Nat Mater 2009;8:260–2.
[23] Urban KW, Houben L, Jia C-L, Lentzen M, Mi S-B, Tillmann K, et al. Atomic-resolution aberration-corrected transmission electron microscopy. Adv Imaging Electron Phys 2008;153:320–44.
[24] Urban KW, Jia C-L, Houben L, Lentzen M, Mi S-B, Tillmann K. Negative spherical aberration ultrahigh-resolution imaging in corrected transmission electron microscopy. Phil Trans R Soc A 2009;367:3735–53.
[25] Urban KW, Barthel J, Houben L, Jia C-L, et al. Ultrahigh-Resolution Transmission Electron Microscopy at Negative Spherical Aberration. Handbook of Nanoscopy 2012;vol. 1:81–107.
[26] Sasaki T, Sawada H, Hosikawa F, Sato Y, Suenaga K. Aberration-corrected STEM/TEM imaging at 15 kV. Ultramicroscopy 2014;145:50–5.
[27] Morishita S, Mukai M, Suenaga K, Sawada H. Atomic Resolution Imaging at an Ultralow Accelerating Voltage by a Monochromatic Transmission Electron Microscope. Phys Rev Lett 2016;117:153004.
[28] Linck M, Hartel P, Uhlemann S, Kahl F, Müller H, Zach J, et al. Chromatic aberration correction for atomic resolution TEM imaging from 20 to 80 kV. Phys Rev Lett 2016;117:076101.
[29] Börrnert F, Kaiser U. Chromatic- and geometric-aberration-corrected TEM imaging at 80 kV and 20 kV. Phys Rev A 2018;98:023861.
[30] Meyer JC, Kisielowski C, Erni R, Rossell MD, Crommie MF, Zettl A. Direct imaging of lattice atoms and topological defects in graphene membranes. Nano Lett 2008;8:3582–6.
[31] Girit ÇÖ, Meyer JC, Erni R, Rossel MD, Kisielowski C, Yang L, et al. Graphene at the edge, stability and dynamics. Science 2009;323:1705–8.
[32] Robertson AW, Warner JH. Atomic resolution imaging of graphene by transmission electron microscopy. Nanoscale 2013;5:4079–93.
[33] Scherzer O. The theoretical resolution limit of the electron microscope. J Appl Phys 1949;20:20–9.
[34] Zernike F. Phase contrast: a new method for the microscopic observation of transparent objects. Part I. Physica 1942;9:686–98.
[35] Zernike F. Phase contrast, a new method for the microscopic observation of transparent objects. Part II. Physica 1942;9:974–86.
[36] Majorovits E, Barton B, Schultheiss K, Pérez-Willard F, Gerthsen D, Schröder RR. Optimizing phase contrast in transmission electron microscopy with an electrostatic (Boersch) phase plate. Ultramicroscopy 2007;107:213–26.
[37] Glaeser RM. Methods for imaging weak-phase objects in electron microscopy. Rev Sci Instrum 2013;84:111101.
[38] Frindt N, Hettler S, Gamm B. In-Focus Electrostatic Zach Phase Plate Imaging for Transmission Electron Microscopy with Tunable Phase Contrast of Frozen Hydrated Biological Samples. Microsc Microanal 2014;20:175–83.
[39] Danev R, Buijsse B, Khoshouei M, Plitzko JM, Baumeister W. Volta potential phase plate for in-focus phase contrast. PNAS 2014;111:15635–40.
[40] Hettler S, Dries M, Zeelen J, Oster M, Schröder RR, Gerthsen D. High-resolution transmission electron microscopy with an electrostatic Zach phase plate. New J Phys 2016;18:053005.
[41] Lichte H. Optimum focus for taking electron holograms. Ultramicroscopy 1991;38:13–22.
[42] Lentzen M, Jahnen B, Jia C-L, Thust A, Tillmann K, Urban K. High-resolution imaging with an aberration-corrected transmission electron microscope. Ultramicroscopy 2002;92:233–42.
[43] Lentzen M. The tuning of a Zernike phase plate with defocus and variable spherical aberration and its use in HRTEM imaging. Ultramicroscopy 2004;99:211–20.
[44] Rose H. Outline of a spherically corrected semiaplanatic medium-voltage transmission electron microscope. Optik 1990;85:19–24.

[45] Haider M, Müller H, Uhlemann S. Present and future hexapole aberration correctors for high-resolution electron microscopy. Adv Imaging Electron Phys 2008; 153:43–119.
[46] Born M, Wolf E. Principles of Optics. 6th edn. Pergamon Press; 1991.
[47] Hawkes PW. The geometrical aberrations of general electron optical systems I. Philos Trans R Soc A 1965;257:479–522.
[48] Hawkes PW. The geometrical aberrations of general electron optical systems II. Philos Trans R Soc A 1965;257:523–52.
[49] Rose H, Plies E. Correction of aberrations in electron optical systems with curved axis. Image Processing and Computer-aided Design in Electron Optics, ed. Hawkes PW, Academic Press 1973:344–369.
[50] Plies E. Korrektur der Öffnungsfehler elektronenoptischer Systeme mit krummer Achse und durchgehend astigmatismusfreien Gaußschen Bahnen. Optik 1973; 38:502–18.
[51] Beck VD. A hexapole spherical aberration corrector. Optik 1979;53:241–55.
[52] Uhlemann S, Haider M. Residual wave aberrations in the first spherical aberration-corrected transmission electron microscope. Ultramicroscopy 1998;72: 109–19.
[53] Müller H, Uhlemann S, Hartel P, Haider M. Advancing the hexapole C_S corrector for the scanning transmission electron microscope. Microsc Microanal 2006; 12:442–55.
[54] Ruska E. Über die Auflösungsgrenzen des Durchstrahlungs-Elektronenmikroskops. Optik 1965;22:319–48.
[55] Kisielowski C, Freitag B, Bischoff M, van Lin H, Lazar S, Knippels G, et al. Detection of single atoms and buried defects in three dimensions by aberration-corrected electron microscope with 0.5-Å Information Limit. Microsc Microanal 2008;14:469–77.
[56] Müller H, Maßmann I, Uhlemann S, Hartel P, Zach J, Haider M. Aplanatic imaging systems for the the transmission electron microscope. Nucl Instrum Methods Phys Res Sect A 2011;645:20–7.
[57] Rose H. Über die Korrigierbarkeit von Linsen für schnelle Elektronen. Optik 1967;26:289–98.
[58] Haider M, Müller H, Uhlemann S, Zach J, Löbau U, Hoeschen R. Prerequisites for a Cc/Cs-corrected ultrahigh-resolution TEM. Ultramicroscopy 2008;108: 167–78.
[59] Haider M, Hartel P, Müller H, Uhlemann S, Zach J. Information transfer in a TEM corrected for spherical and chromatic aberration. Microsc Microanal 2010; 16:393–408.
[60] Ercius P, Boese M, Duden T, Dahmen U. Operation of TEAM I in a User Environment at NCEM. Microsc Microanal 2012;18:676–83.
[61] Uhlemann S, Müller H, Hartel P, Zach J, Haider M. Thermal magnetic field noise limits resolution in transmission electron microscopy. Phys Rev Lett 2013; 111:046101.
[62] Uhlemann S, Müller H, Zach J, Haider M. Thermal magnetic field noise: electron optics and decoherence. Ultramicroscopy 2015;151:199–210.
[63] Jin L, Barthel J, Jia C-L, Urban K. Atomic resolution imaging of $YAlO_3$: Ce in the chromatic and spherical aberration-corrected PICO electron microscope. Ultramicroscopy 2017;176:99–104.
[64] Zemlin F, Weiss K, Schiske P, Kunath W, Herrmann KH. Coma-free alignment of high-resolution electron microscopes with the aid of optical diffractograms. Ultramicroscopy 1978;3:49–60.
[65] Barthel J, Thust A. Aberration measurement in HRTEM; Implementation and diagnostic use of numerical procedures for the highly precise recognition of diffractogram patterns. Ultramicroscopy 2010;111:27–46.
[66] Barthel J, Thust A. On the optical stability of high-resolution transmission electron microscopes. Ultramicroscopy 2013;134:6–17.
[67] Stadelmann PA. EMS - A software package for electron diffraction analysis and HREM image simulation in materials science. Ultramicroscopy 1987;21: 131–45.
[68] Kilaas R. Interactive simulation of high resolution electron micrographs. In: Bailey GW, editor. Proc 45th Annual EMSA Meeting. San Francisco Press; 1987. p. 66–7.
[69] Barthel J. Dr-Probe; A software for high-resolution STEM image simulation. Ultramicroscopy 2018;193:1–11.
[70] Lobato I, Van Dyck D. MULTEM: A new multislice program to perform accurate and fast electron diffraction and imaging simulations using Graphics Processing Units with CUDA. Ultramicroscopy 2015;156:9–17.
[71] Allen LJ, D'Alfonso AJ, Findlay SD. Modelling the inelastic scattering of fast electrons. Ultramicroscopy 2015;151:11–22.
[72] Grillo V, Rotunno E. STEM_CELL: A software tool for electron microscopy; Part I – simulations. Ultramicroscopy 2013;125:97–111.
[73] Kirkland EJ. Advanced Computing in Electron Microscopy. 3rd edn. Springer; 2020.
[74] List of current links to image simulation computer codes (incomplete):
COMPUTEM - https://sourceforge.net/projects/computem/;
Dr. Probe - https://er-c.org/barthel/drprobe/index.html;
HREM - https://www.hremresearch.com/index.html;
JEMS - https://www.jems-swiss.ch/;
MacTempas - https://www.totalresolution.com/;
MULTEM - https://github.com/Ivanlh20/MULTEM;
μSTEM - https://github.com/HamishGBrown/MuSTEM/blob/master/readme.md;
QSTEM - https://www.physics.hu-berlin.de/en/sem/software/software_qstem;
STEM_CELL - http://tem-s3.nano.cnr.it/.
[75] Rother A, Scheerschmidt K. Relativistic effects in elastic scattering of electrons in TEM. Ultramicroscopy 2009;109:154–60.
[76] Lentzen M. Progress in aberration-corrected high-resolution transmission electron microscopy using hardware aberration correction. Microsc Microanal 2006; 12:191–205.
[77] Lentzen M. Contrast transfer and resolution limits for sub-angström high-resolution transmission electron microscopy. Microsc Microanal 2008;14:16–26.
[78] Hanszen K-J, Trepte L. The influence of voltage and current fluctuations and of a finite energy width of the electrons on contrast and resolution in electron microscopy. Optik 1971;32:519–38.
[79] Barthel J, Thust A. Quantification of the information limit of transmission electron microscopes. Phys Rev Lett 2008;101:200801.
[80] O'Keefe MA. "Resolution" in high-resolution electron microscopy. Ultramicroscopy 1992;47:282–97.
[81] Zhang Z, Kaiser U. Structural imaging of β-Si_3N_4 by spherical aberration-corrected high-resolution transmission electron microscopy. Ultramicroscopy 2009; 109:1114–20.
[82] Meyer JC, Kurasch S, Park HJ, Skakalova V, Künzel D, Groß A, et al. Experimental analysis of charge redistribution due to chemical bonding by high-resolution transmission electron microscopy. Nat Mater 2011;10:209–15.
[83] Jia C-L. Unpublished data. 2001.
[84] Jia C-L, Lentzen M, Urban K. Atomic-resolution imaging of oxygen in perovskite ceramics. Science 2003;299:870–3.
[85] Jia C-L, Urban K. Atomic-resolution measurement of oxygen concentration in oxide materials. Science 2004;303:2001–4.
[86] Spence JCH. Oxygen in Crystals – Seeing is Believing. Science 2003;299:839–41.
[87] Thomas JM, Zhou W. Atomic Resolution of Oxygen in Solid Oxides by Electron Microscopy: What Next? ChemPhysChem 2003;4:927–9.
[88] Ourmazd A, Rentschler JA, Spence JCH, O'Keefe M, Graham RJ, Johnson Jr DW, et al. Microstructure, oxygen ordering and planar defects in the high Tc superconductor $YBa_2Cu_3O_{6.9}$. Nature 1987;327:308–10.
[89] Gibson MJ. Now you see them, now you don't. Nature 1987;329:763–4.
[90] Huxford NP, Eaglesham DJ, Humphreys CJ. Limits on Quantitative information from high-resolution electron microscopy of $YBa_2Cu_3O_7$ superconductors. Nature 1987;329:812–3.
[91] Horiuchi S, Matsui Y, Kitami Y, Yokoyama M, Suehara S, Wu XJ, et al. Ultra-high resolution HVEM (H-1500) newly constructed at NRIM II. Application to materials. Ultramicroscopy 1991;39:231–7.

[92] Jia CL, Thust A. Investigation of atom displacements at a Σ3 {111} twin boundary in $BaTiO_3$ by means of phase-retrieval electron microscopy. Phys Rev Lett 1999;82:5052–5.
[93] Kisielowski C, Hetherington CJD, Wang YC, Kilaas R, O'Keefe MA, Thust A. Imaging columns of the light elements carbon, nitrogen and oxygen with sub-Angström resolution. Ultramicroscopy 2001;89:243–63.
[94] Jia CL, Lentzen M, Urban K. High resolution transmission electron microscopy using negative spherical aberration. Microsc Microanal 2004;10:174–84.
[95] Howie A. Diffraction channelling of fast electrons and positrons in crystals. Phil Mag 1966;14:223–37.
[96] Urban K, Yoshida N. The effect of electron diffraction channelling on the displacement of atoms in electron-irradiated crystals. Rad Eff Def in S 1979;42:1–15.
[97] Van Dyck D, Op de Beeck M. A simple intuitive theory for electron diffraction. Ultramicroscopy 1996;64:199–207.
[98] Scherzer O. Die Strahlenschädigung der Objekte als Grenze für Hochauflösende Elektronenmikroskopie. Ber Bunsenges 1970;74:1154–67.
[99] Lentzen M, Urban K. Reconstruction of the projected crystal potential in transmission electron microscopy by means of a maximum-likelihood refinement algorithm. Acta Cryst A 2000;56:235–47.
[100] Jia C-L, Houben L, Thust A, Barthel J. On the benefit of the negative spherical-aberration imaging technique for quantitative HRTEM. Ultramicroscopy 2010;110:500–5.
[101] Hÿtch M, Stobbs W. Quantitative comparison of high resolution TEM images with image simulations. Ultramicroscopy 1994;53:191–203.
[102] Coene W, Janssen G, Op de Beeck M, Van Dyck D. Phase retrieval through focus variation for ultra-resolution in field emission transmission electron microscopy. Phys Rev Lett 1992;69:3743–6.
[103] Coene WMJ, Thust A, Op de Beeck M, Van Dyck D. Maximum-likelihood method for focus-variation image reconstruction in high resolution transmission electron microscopy. Ultramicroscopy 1996;64:109–35.
[104] Thust A, Coene WMJ, Op de Beeck M, Van Dyck D. Focal-series reconstruction in HRTEM: Simulation studies on non-periodic objects. Ultramicroscopy 1996;64:211–30.
[105] Thust A, Overwijk MHF, Coene WMJ, Lentzen M. Numerical correction of lens aberrations in phase-retrieval HRTEM. Ultramicroscopy 1996;64:249–64.
[106] O'Keefe MA, Hetherington CJD, Wang YC, Nelson EC, Turner JH, Kisielowski C, et al. Sub-Ångström high-resolution transmission electron microscopy at 300 keV. Ultramicroscopy 2001;89:215–41.
[107] Jinschek JR, Yucelen E, Calderon HA, Freitag B. Quantitative atomic 3-D imaging of single/double sheet graphene structure. Carbon 2011;49:556–62.
[108] Chen F-R, Van Dyck D, Kisielowski C. In-line three-dimensional holography of nanocrystalline objects at atomic resolution. Nat Commun 2015;7:10603.
[109] Winkler F, Barthel J, Tavabi AH, Borghardt S, Kardynal BE, Dunin-Borkowski RE. Absolute scale quantitative off-axis electron holography at atomic resolution. Phys Rev Lett 2018;156101.
[110] Tillmann K, Thust A, Urban K. Spherical aberration correction in tandem with exit-plane wave function reconstruction: Interlocking tools for the atomic scale imaging of lattice defects in GaAs. Microsc Microanal 2004;10:185–98.
[111] Houben L, Thust A, Urban K. Atomic-precision determination of the reconstruction of a 90° tilt boundary in $YBa_2Cu_3O_7$ by aberration-corrected HRTEM. Ultramicroscopy 2006;106:200–14.
[112] Jia C-L, Thust A, Urban K. Atomic-scale analysis of the oxygen configuration at a $SrTiO_3$ dislocation core. Phys Rev Lett 2005;95:225506.
[113] Bloch F. Zur Bremsung rasch bewegter Teilchen beim Durchgang durch Materie. Ann Phys 1933;16:285–320.
[114] Makin MJ. Electron displacement damage in copper and aluminum in a high voltage electron microscope. Phil Mag A 1968;18:637–53.
[115] Urban K. Voids in Nickel after Electron Irradiation. Phys Stat Sol (a) 1970;3:K167.
[116] Kiritani M, Yoshida N, Takata H, Maehara Y. Growth of interstitial type dislocation loops and vacancy mobility in electron-irradiated metals. J Phys Soc Japan 1975;38:1677–86.
[117] Egerton RF. Radiation damage in organic and inorganic specimens in the TEM. Micron 2019;119:72–87.
[118] Rose A. Vision: Human and Electron. Plenum Press; 1973.
[119] Glaeser RM. Limitations to significant information in biological electron microscopy as a result of radiation damage. J Ultrastructure Res 1971;36:466–82.
[120] Kisielowski C, Frei H, Specht P, Sharp D, Haber JA, Helveg S. Detecting structural variances of Co_3O_4 catalysts by controlling beam-induced sample alterations in the vacuum of a transmission electron microscope. Adv Struct Chem Imag 2016;2:13.
[121] Barthel J, Lentzen M, Thust A. On the influence of the electron dose rate on the HRTEM image contrast. Ultramicroscopy 2017;176:37–45.
[122] Urban K, Seeger A. Radiation-induced diffusion of point defects during low-temperature electron irradiation. Phil Mag 1974;30:1395–418.
[123] Kisielowski C, Wang LW, Specht P, Calderon HA, Barton B, Jiang B, et al. Real-time sub-Ångström imaging of reversible and irreversible conformations in rhodium catalysts and graphene. Phys Rev B 2013;88:024305.
[124] Jia CL, Jin L, Chen Y-H, Urban KW, Wang H. Atomic-scale evidence for displacive disorder in bismuth zinc niobate pyrochlore. Ultramicroscopy 2018;192:57–68.
[125] Van Dyck D, Lobato I, Chen F-R, Kisielowski C. Do you believe that atoms stay in place when you observe them in HREM? Micron 2014;68:158–63.
[126] Kisielowski C, Specht P, Freitag B, Kieft ER, Verhoeven W, van Rens JFM, et al. Discovering hidden material properties of $MgCl_2$ at atomic resolution with structured temporal electron illumination of picosecond time resolution. Adv Funct Mater 2019;29:1807818.
[127] Hecht E. Optics. 6th edn. Addison Wesley; 2015.
[128] Frank J. The envelope of electron microscopic transfer functions for partially coherent illumination. Optik 1973;38:519–36.
[129] Wade RH, Frank J. Electron microscope transfer functions for partially coherent axial illumination and chromatic defocus spread. Optik 1977;49:81–92.
[130] Van Dyck D, de Jong AF. Ultimate resolution and information in electron microscopy I; general principles. Ultramicroscopy 1992;47:266–81.
[131] De Jong AF, Van Dyck D. Ultimate resolution and information in electron microscopy II; The information limit of transmission electron microscopes. Ultramicroscopy 1993;49:66–80.
[132] Ishizuka K. Contrast transfer of crystal images in TEM. Ultramicroscopy 1980;5:55–65.
[133] Boothroyd CB. Why don't high-resolution simulations and images match? J Microscopy 1997;190:99–108.
[134] Thust A. High-resolution transmission electron microscopy on an absolute contrast scale. Phys Rev Lett 2009;102:220801.
[135] Chang SLY, Dwyer C, Barthel J, Boothroyd CB, Dunin-Borkowski RE. Performance of a direct detection camera for off-axis electron holography. Ultramicroscopy 2016;161:90–7.
[136] Meyer RR, Kirkland AI, Dunin-Borkowski RE, Hutchison JL. Experimental characterization of CCD cameras for HREM at 300 kV. Ultramicroscopy 2000;85:9–13.
[137] Meyer RR, Kirkland AI. Characterization of the signal and noise transfer of CCD cameras for electron detection. Micros Res Tech 2000;49:269–80.
[138] Frank J. Determination of source size and energy spread from electron micrographs using the method of Young's fringes. Optik 1976;44:379–91.
[139] Den Dekker AJ, Van Aert S, van den Bos A, Van Dyck D. Maximum likelihood estimation of structure parameters from high resolution electron microscopy images. Part I; A theoretical framework. Ultramicroscopy 2005;104:83–106.
[140] Van Aert S, den Dekker AJ, van den Bos A, Van Dyck D, Chen JH. Maximum likelihood estimation of structure parameters from high resolution electron microscopy images. Part II; A practical example. Ultramicroscopy 2005;104:107–25.
[141] Mi S-B, Jia C-L, Vaithyanathan V, Houben L, Schubert J, Schlom DG, et al. Atomic structure of the interface between $SrTiO_3$ thin films and Si (001) substrates. Appl Phys Lett 2008;93:101913.
[142] Jia C-L, Mi SB, Urban K, Vrejoiu I, Alexe M, Hesse D. Effect of a single dislocation in a heterostructure layer on the local polarization of a ferroelectric layer. Phys Rev Lett 2009;102:117601.
[143] Kleiner R, Buckel W. Superconductivity: An Introduction. 3rd edn. Wiley-VCH; 2015.
[144] Poppe U, Klein N, Dähne U, Soltner H, Jia C-L, Kabius B, et al. Low-resistivity epitaxial YBaCuO thin films with improved microstructure and reduced microwave losses. J Appl Phys 1992;71:5572–8.
[145] Rečnik A, Bruley J, Mader W, Kolar D, Rühle M. Structural and spectroscopic investigation of (111) twins in barium titanate. Phil Mag B 1994;70:1021–34.
[146] Grey IE, Li CH, Cranswick LMD, Roth RS, Vanderah TA. Structure Analysis of the 6H-Ba(Ti, Fe^{3+}, Fe^{4+})$O_{3-\delta}$ Solid Solution. J Sol State Chem 1998;135:312–21.

[147] An J, Koh AL, Park JS, Sinclair R, Gür TM, Prinz FB. Aberration-corrected TEM imaging of oxygen occupancy in YSZ. Phys Chem Lett 2013;4:1156–60.
[148] An J, Park JS, Koh AL, Lee HB, Jung HJ, Schoonman J, et al. Atomic scale verification of oxide-ion vacancy distribution near a single grainboundary in YSZ. Sci Rep 2013;3:2680.
[149] Guo X, Maier J. Grain boundary blocking effect in zirconia: a schottky barrier analysis. J Electrochem Soc 2001;148:E121–6.
[150] Lai M-W, Kurata H. Understanding ordered structure in hematite nanowhiskers synthesized via thermal oxidation of iron-based substrates. Mater Design 2020; 191:108596.
[151] Kelly A, Groves GW, Kidd P. Crystallography and Crystal Defects. Wiley; 2000.
[152] Hull D, Bacon DJ. Introduction to dislocations. Elsevier; 2011.
[153] Cockayne DJH, Ray ILF, Whelan MJ. Investigations of dislocation strain fields using weak beams. Phil Mag 1969;20:1265–70.
[154] Cockayne DJH. Weak-beam electron microscopy. Ann Rev Mater Sci 1981;11:75–95.
[155] Jia C-L, Houben L, Urban K. Atom vacancies at a screw dislocation core in SrTiO3. Phil Mag Lett 2006;86:683–90.
[156] Eshelby JD, Stroh AN. Dislocations in thin plates. The London, Edinburgh, and Dublin Philosophical Magazine and Journal of Science 1951;42:1401–5.
[157] Sigle W. High-resolution electron microscopy and molecular dynamics study of the (a/2)[111] screw dislocation in molybdenum. Phil Mag A 1999;79: 1009–20.
[158] Duesbery MS, Vitek V. Plastic anisotropy in bcc transition metals. Acta Mater 1998;46:1481–92.
[159] Heuer AH, Jia C-L, Lagerlöf KPD. The core structure of basal dislocations in deformed sapphire (α-Al_2O_3). Science 2010;330:1227–31.
[160] Shibata N, Chrisholm MF, Nakamura A, Pennycook SJ, Yamamoto T, Ikuhara Y. Nonstoichiometric dislocation cores in α-alumina. Science 2007;316:82–5.
[161] Zhang W, Yu R, Du K, Cheng Z, Zhu J, Ye H. Undulating slip in laves phase and implications for deformation of brittle materials. Phys Rev Lett 2011;106: 165505.
[162] Catalan G, Seidel J, Ramesh R, Scott JF. Domain wall nanoelectronics. Rev Mod Phys 2012;84:119–56.
[163] Jia C-L, Mi S-B, Urban K, Vrejoiu I, Alexe M, Hesse D. Atomic-scale study of electric dipoles near charged and uncharged domain walls in ferroelectric films. Nat Mater 2008;7:57–61.
[164] Lee D, Behera RK, Wu P, Xu H, Li YL, Sinnott SB, et al. Mixed Bloch-Néel-Ising character of 180° ferroelectric domain walls. Phys Rev B 2009;80:060102(R).
[165] Zhong W, King-Smith RD, Vanderbilt D. Giant LO-TO splittings in perovskite ferroelectrics. Phys Rev Lett 1994;72:3618–21.
[166] Stephenson GB, Elder KR. Theory for equilibrium 180° stripe domains in $PbTiO_3$ films. J Appl Phys 2006;100:051601.
[167] Prosandeev S, Bellaiche L. Asymmetric screening of the depolarizing field in a ferroelectric thin film. Phys Rev B 2007;75:172109.
[168] Jia C-L, Urban K, Alexe M, Hesse D, Vrejoiu I. Direct observation of continuous electric dipole rotation in flux-closure domains in ferroelectric Pb(Zr, Ti)O_3. Science 2011;331:1420–3.
[169] Wei X-K, Jia C-L, Sluka T, Wang B-X, Ye Z-G, Setter N. Néel-like domain walls in ferroelectric $Pb(Zr,Ti)O_3$ single crystals. Nat Commun 2016;7:12385.
[170] Wei X-K, Tagantsev AK, Kvasov A, Roleder K, Jia C-L, Setter N. Ferroelectric translational antiphase boundaries in nonpolar materials. Nat Commun 2014;5: 3031.
[171] Ohtomo A, Hwang HY. A high-mobility electron gas at the LaAlO/SrTiO heterointerface. Nature 2004;427:423–6.
[172] Jia C-L, Mi S-B, Faley M, Poppe U, Schubert J, Urban K. Oxygen octahedron reconstruction in the $SrTiO_3/LaAlO_3$ heterointerfaces investigated using aberration-corrected ultrahigh-resolution transmission electron microscopy. Phys Rev B 2009;79:081405(R).
[173] Jia C-L, Barthel J, Gunkel F, Dittmann R, Hoffmann-Eifert S, Houben L, et al. Atomic-scale measurement of structure and chemistry of a single-unit-cell layer of $LaAlO_3$ embedded in $SrTiO_3$. Microsc Microanal 2013;19:310–8.
[174] Hashimoto H, Howie A, Whelan MJ. Anomalous electron absorption effects in metal foils: theory and comparison with experiment. Proc Roy Soc A 1962;21: 80–103.
[175] Jia C-L, Nagarajan V, He J-Q, Houben L, Zhao RR, Urban K, et al. Unit-cell scale mapping of ferroelectricity and tetragonality in epitaxial ultrathin ferroelectric films. Nat Mater 2007;6:64–9.
[176] Muralt P. The emancipation of ferroelectricity. Nat Mater 2007;6:8–9.
[177] Kinyanjui MK, Lu Y, Gauquelin N, Wu M, Frano A, Wochner P, et al. Lattice distortions and octahedral rotations in epitaxially strained $LaNiO_3/LaAlO_3$ superlattices. Appl Phys Lett 2014;104:221909.
[178] Qi HY, Kinyanjui MK, Biskupek J, Geiger D, Benckiser E, Habermeier H-U, et al. Local octahedral rotations and octahedral connectivity in epitaxially strained $LaNiO_3/LaGaO_3$ superlattices. J Mater Sci 2015;50:5300–6.
[179] Qi HY, Kinyanjui MK, Chen XD, Biskupek J, Geiger D, Benckiser E, et al. Control of octahedral rotations via octahedral connectivity in an epitaxially strained [1 u.c.//4 u.c.] $LaNiO_3/LaGaO_3$ superlattice. J Mater Sci 2016;51:8168–76.
[180] Qi H, Chen X, Benckiser E, Wu M, Cristiani G, Logvenov G, et al. Formation mechanism of Ruddlesden-Popper faults in compressive-strained ABO_3 perovskite superlattices. Nanoscale 2021;13:20663–9.
[181] Du H, Groh C, Jia C-L, Ohlerth T, Dunin-Borkowski RE, Simon U, et al. Multiple polarization orders in individual twinned colloidal nanocrystals of centrosymmetric HfO_2. Matter 2021;4:986–1000.
[182] Scott JF. Applications of Modern Ferroelectrics. Science 2007;315:954–9.
[183] Mi S-B, Jia C-L, Vrejoiu I, Alexe M, Hesse D. Atomic-scale structure and properties of epitaxial $PbZr_{0.2}Ti_{0.8}O_3/SrRuO_3$ heterointerfaces. Adv Mater Interfaces 2015;2:1500087.
[184] Abrahams SC, Kurtz SK, Jamieson PB. Atomic displacement relationship to curie temperature and spontaneous polarization in displacive ferroelectrics. Phys Rev 1968;172:551–3.
[185] Lu S, Kormondy KJ, Ngo TQ, Aoki T, Posadas A, Ekerdt JG, et al. Spectrum and phase mapping across the epitaxial γ-$Al_2O_3/SrTiO_3$ interface. Appl Phys Lett 2016;108:051606.
[186] Gontard LC, Chang L-Y, Hetherington CJD, Kirkland AI, Ozykaya D, Dunin-Borkowski RE. Aberration-corrected imaging of active sites on industrial catalyst nanoparticles. Angew Chem Int Ed 2007;46:3683–6.
[187] Su DS, Jacob T, Hansen TW, Wand D, Schlögl R, et al. Surface Chemistry of Ag Particles: Identification of Oxide Species by Aberration-Corrected TEM and by DFT Calculations. Angew Chem Int Ed 2008;47:5005–8.
[188] Bar Sadan M, Houben L, Enyashin AN, Seifert G, Tenne R. Atom by atom: HRTEM insights into inorganic nanotubes and fullerene-like structures. PNAS 2008; 41:15643–8.
[189] Pohl D, Wiesenhütter U, Mohn E, Schultz L, Rellinghaus B. Near-surface strain in icosahedra of binary metallic alloys: segregational versus intrinsic effects. Nano Lett 2014;14:1776–84.
[190] Bieniek B, Pohl D, Schultz L. The effect of oxidation on the surface-near lattice relaxation in FeNi nanoparticles. J Nanopart Res 2011;13:5935–46.
[191] Yu R, Hu LH, Cheng ZY, Li YD, Ye Q, Zhu J. Direct subangström measurement of surfaces of oxide particles. Phys Rev Lett 2010;105:226101.
[192] He M-R, Yi R, Zhu J. Subangstrom profile imaging of relaxed ZnO (1010) surfaces. Nano Lett 2012;12:704–8.
[193] He M-M, Yu R, Zhu J. Reversible wurtzite-tetragonal reconstruction in ZnO (1010). Surfaces. Angew Chem 2012;124:7864–7.
[194] Lu N, Wan Q, Zhu J. Surface structure of Zigzag SnO_2 nanobelts. J Phys Chem Lett 2010;1:1468–71.
[195] Liu S, Liu L, Cheng Z, Zhu J, Yu R. Atomic structure and properties of SnO_2 (100) and (101) surfaces and (301) steps in the (100) surface. J Phys Chem C 2020; 124:27631–6.
[196] Bergermayer W, Tanaka I. Reduced SnO surfaces by first-principles calculations. Appl Phys Lett 2004;84:909–11.
[197] Reuter K, Scheffler M. Composition, structure, and stability of RuO_2 (110) as a function of oxygen pressure. Phys Rev B 2001;65:035406.
[198] Urban K, Martin G. Precipitate coarsening induced by point-defect recombination in alloys under irradiation. Acta Metall 1982;30:1209–18.
[199] Banerjee S, Urban K, Wilkens M. Order-disorder transformation in Ni_4Mo under electron irradiation in a high-voltage electron microscope. Acta Metall 1984; 32:299–311.
[200] Martin G, Bellon P. Driven Alloys. Sol State Phys 1996;50:189–331.

[201] Liu L, Cheng Z, Li Y, Zhu J, Yu R. Structure and stability of the (001) surface of Co_3O_4. J Phys Chem C 2020;124:25790–5.
[202] Bliem R, McDermott E, Ferstl P, Setvin M, Gamba O, Pavelec J, et al. Subsurface cation vacancy stabilization of the magnetite (001) surface. Science 2014;346:1215–8.
[203] Liu L, Sun Y, Cheng Z, Zhu J, Yu R. Subsurface reconstruction and saturation of surface bonds. Sci Bull 2018;63:1570–5.
[204] Xing W, Sha H, Meng H, Yu R. Defect structures of the Cr_2O_3 (1,1,-2,0) surface: effect of electron beam irradiation. J Mater Chem C 2021;9:6324–31.
[205] Jia C-L, Mi S-B, Barthel J, Wang DW, Dunin-Borkowski RE, Urban KW, et al. Determination of the 3D shape of a nanoscale crystal with atomic resolution from a single image. Nat Mater 2014;13:1044–9.
[206] Allen LJ. Shape of a crystal from one image. Nat Mater 2014;13:1000–1.
[207] Lu SR, Yu R, Zhu J. Atomic steps on the MgO(100) surface. Phys Rev B 2013;87:165436.
[208] Tasker PW. The stability of ionic crystal surfaces. J Phys C: Sol State Phys 1979;12:4977–84.
[209] Tsong IST, Knipping U, Loxton CM, Magee CW, Arnold GW. Carbon on surfaces of magnesium oxide and olivine single crystals. Diffusion from the bulk or surface oxide contamination? Phys Chem Minerals 1985;12:261–70.
[210] Ge Z-H, Li W-J, Feng J, Zheng F, Jia C-L, Wu D, et al. Atomic-scale observation of off-centering rattlers in filled skutterudites. Adv Energy Mater 2022;2103770.
[211] Rull-Bravo M, Moure A, Fernández M-G. Skutterudites as thermoelectric materials: revisited. RSC Adv 2015;5:41653–67.
[212] Chakoumakos BC, Sales BC, Mandrus D, Keppens V. Disparate atomic displacements in skutterudite-type $LaFe_3CoSb_{12}$, a model for thermoelectric behavior. Acta Cryst B 1999;55:341–7.
[213] Fu Y, He X, Zhang L, Singh DJ. Collective-goldstone-mode-induced ultralow lattice thermal conductivity in Sn-filled skutterudite $SnFe_4Sb_{12}$. Phys Rev B 2018;97:024301.
[214] von Ardenne M. Reaktionskammer-Übermikroskopie mit dem Universal-Elektronenmikroskop. Zeitschr Phys Chem 1942;52:61–71.
[215] Ruska E. Beitrag zur übermikroskopischen Abbildung bei höheren Drucken. Kolloid Zeitschr 1942;100:212–9.
[216] Heide HG, Urban K. A novel specimen stage permitting high-resolution electron microscopy at low temperatures. J Phys E 1972;5:803–8.
[217] Messerschmidt U, Bartsch M. High-temperature straining stage for in-situ experiments in the high-voltage electron microscope. Ultramicroscopy 1994;56:163–71.
[218] Saka H, Imura T. Direct measurement of mobility of edge and screw dislocations in 3% silicon-iron by high voltage transmission electron microscopy. J Phys Soc Japan 1972;32:702–16.
[219] Mayer J, Urban K. Spinodal ordering in Ni_4Mo. Acta Metall 1985;33:539–43.
[220] Wollgarten M, Bartsch M, Messerschmidt U, Feuerbacher M, Rosenfeld R, Urban K. In-situ observation of dislocation motion in icosahedral Al-Pd-Mn single quasicrystals. Phil Mag Lett 1995;71:99–105.
[221] Thomas G, Fulrath RM, Fisher RM. Electron Microscopy and Structure of Materials. Univ California Press;1972. Reprint De Gruyter;2020.
[222] Butler EP. In situ experiments in the transmission electron microscope. Rep Prog Phys 1979;42:833–95.
[223] Robertson IM, Kirk M, Messerschmidt U, Yang J, Hull R. (Editors). in situ transmission electron microscopy. J Mat Res 2005;20:1617–926.
[224] Sun L, Xu T, Zhang Z. In-situ transmission electron microscopy. Springer; 2023. In press.
[225] Hansen TW, Wagner B, Dunin-Borkowski RE. Aberration corrected and monochromated environmental transmission electron microscopy: challenges and prospects for materials science. Mat Sci Techn 2010;26:1338–44.
[226] Hansen TW, Wagner JB, editors. Controlled Atmosphere Transmission Electron Microscopy – Principles and Practice. Springer; 2016.
[227] De Jonge N, Ross FM. Electron microscopy of specimens in liquid. Nat Nanotech 2011:695–704.
[228] Ross F. Opportunities and challenges in liquid cell electron microscopy. Science 2015;350:aaa9886-1–9886-9.
[229] Yuk JM, Park J, Ercius P, Kim K, Hellebusch GJ, Crommie MF, et al. High-resolution EM of colloidal nanocrystal growth using graphene liquid cells. Science 2012;336:61–4.
[230] Kamino T, Yaguchi T, Konno M, Watabe A, Marukawa T, Mima T, et al. Development of a gas injection/specimen heating holder for use with transmission electron microscope. J Electron Microsc 2005;54:497–503.
[231] Zhang XF, Kamino T. Imaging gas-solid interactions in an atomic resolution environmental TEM. Microscopy Today 2006;14:16–8.
[232] Jinschek JR, Helveg S. Image resolution and sensitivity in an environmental transmission electron microscope. Micron 2012;43:1156–68.
[233] Sinclair S, Kempen PJ, Chin R, Koh AL. The Stanford nanocharacterization laboratory (SNL) and recent applications of an aberration-corrected environmental transmission electron microscope. Adv Eng Mat 2014;16:476–81.
[234] Chou Y-C, Panciera F, Reuter MC, Stach EA, Ross FM. Nanowire growth kinetics in aberration corrected environmental transmission electron microscopy. Chem Commun 2016;52:5686–9.
[235] Panciera F, Chou Y-C, Reuter MC, Zakharov D, Stach EY, Hofmann S, et al. Synthesis of nanostructures in nanowires using sequential catalyst reactions. Nat Mater 2015;14:820–5.
[236] Zhang Z, Chen J, Li H, Zhang Z, Wang Y. Vapor−solid nanotube growth via sidewall epitaxy in an environmental transmission electron microscope. Cryst Growth Design 2017;17:11–5.
[237] Yoshida H, Kuwauchi Y, Jinschek JR, Sun K, Tanaka S, Kohyama M, et al. Visualizing gas molecules interacting with supported nanoparticulate catalysts at reaction conditions. Science 2012;335:317–9.
[238] Takeda S, Yoshida H. Atomic-resolution environmental TEM for quantitative in-situ microscopy in materials science. Microscopy 2013;62:193–203.
[239] He Y, Liu J-C, Luo L, Wang Y-G, Zhu J, Du Y, et al. Size-dependent dynamic structures of supported gold nanoparticles in CO oxidation reaction condition. PNAS 2018;115:7700–5.
[240] Yuan W, Zhu B, Fang K, Li X-Y, Hansen TW, Ou Y, et al. In situ manipulation of the active Au-TiO_2 interface with atomic precision during CO oxidation. Science 2021;371:517–21.
[241] Koh AL, Gidcumb E, Zhou O, Sinclair R. Observations of carbon nanotube oxidation in an aberration-corrected environmental transmission electron microscope. ACS Nano 2013;7:2566–72.
[242] Yuan W, Wang Y, Li H, Wu H, Zhang Z, Selloni A, et al. Real-time observation of reconstruction dynamics on TiO_2(001) surface under oxygen via an environmental transmission electron microscope. Nano Lett 2016;16:132–7.
[243] Menzel D. Electron stimulated desorption: principles and recent developments. Surf Sci 1975;47:370–83.
[244] Knotek ML, Feibelman PJ. Ion desorption by core hole auger decay. Phys Rev Lett 1978:964–7.
[245] Franchy R, Menzel D. Adsorbate core ionization as primary process in electron and photon-stimulated desorption from metal surfaces. Phys Rev Lett 1979;43:865–7.
[246] Yuan W, Zhu B, Li X-Y, Hansen TW, Ou Y, Fang K, et al. Visualizing H_2O molecules reacting at TiO_2 active sites with transmission electron microscopy. Science 2020;367:428–30.
[247] Gandman M, Kauffmann Y, Koch CT, Kaplan WD. Direct quantification of ordering at a solid-liquid interface using aberration corrected transmission electron microscopy. Phys Rev Lett 2013;110:086106.
[248] Kaplan WD, Kauffmann Y. Structural order in liquids induced by interfaces with crystals. Annu Rev Mater Res 2006;36:1–48.
[249] Sinclair R, Lee SC, Shi Y, Chueh WC. Structure and chemistry of epitaxial ceria thin films on yttria-stabilized zirconia substrates, studied by high resolution electron microscopy. Ultramicroscopy 2017;176:200–11.
[250] Schneider S, Surrey A, Pohl D, Schultz L, Rellinghaus B. Atomic surface diffusion on Pt nanoparticles quantified by high-resolution transmission electron microscopy. Micron 2014;63:52–6.
[251] Mehrer H. Diffusion in Solids. Springer; 2007.
[252] Nallagatla VR, Heisig T, Baeumer C, Feyer V, Jugovac M, Zamborlini G, et al. Topotactic phase transition driving memristive behavior. Adv Mater 2019;31:1903391.
[253] Khare A, Shin D, Yoo TS, Kim M, Kang TD, Lee J, et al. Topotactic metal-insulator transition in epitaxial SrFeOx thin films. Adv Mater 2017;29:1606566.

[254] Xing Y, Kim I, Kang KT, Park B, Wang Z, Kim JC, et al. Atomic-scale operando observation of oxygen diffusion during topotactic phase transition of a perovskite oxide. Matter 2022;5:1–14.
[255] Challa MSS, Landau DP, Binder K. Monte Calo studies of finite-size effects at first-order transitions. Phase Trans 1990;24–26:343–69.
[256] Zheng H, Rivest JB, Miller TA, Sadtler B, Lindenberg A, Toney MF, et al. Observation of transient structural-transformation dynamics in a Cu_2S nanorod. Science 2011;333:206–9.
[257] Wei X-K, Jia C-L, Du HC, Roleder K, Mayer J, Dunin-Borkowski RE. An unconventional transient phase with cycloidal order of polarization in energy-storage antiferroelectric $PbZrO_3$. Adv Mater 2020;32:1907208.
[258] Wei X-K, Jia C-L, Roleder K, Dunin-Borkowski RE, Mayer J. In situ observation of point-defect-induced unit-cell-wise energy storage pathway in antiferroelectric $PbZrO_3$. Adv Funct Mater 2021;31:2008609.
[259] Spiecker E, Oh SH, Shan Z-W, Ikuhara Y, Mao SX. Insights into fundamental deformation processes from advanced *in situ* transmission electron microscopy. MRS Bull 2019;44:443–9.
[260] Zhang J, Li Y, Li X, Zhai Y, Zhang Q, Ma D, et al. Timely and atomic-resolved high-temperature mechanical investigation of ductile fracture and atomistic mechanisms of tungsten. Nat Commun 2021;12:2218.
[261] Wang SJ, Wang H, Du K, Zhang W, Sui ML, Mao SX. Deformation-induced structural transition in body-centred cubic molybdenum. Nat Commun 2014;5:3433.
[262] Fisher SB. On the temperature rise in electron irradiated foils. Radiation effects 1970;5:239–43.
[263] Egerton RF, Li P, Malac M. Radiation damage in TEM and STEM. Micron 2004;35:399–409.
[264] Niekiel F, Kraschewski MJ, Butz B, Spiecker E. Local temperature measurement in TEM by parallel beam electron diffraction. Ultramicroscopy 2017;176:161–9.
[265] Fritsch B, Hutzler A, Wu M, Khadivianazar S, Vogl L, Jank MPM, et al. Accessing local electron-beam induced temperature changes during in situ liquid-phase transmission electron microscopy. Nanoscale Adv 2021;3:2466–74.
[266] Li YZ, Li YB, Pei A, Yan K, Sun Y, Wu C-L, et al. Atomic structure of sensitive battery materials and interfaces revealed by cryo–electron microscopy. Science 2017;358:506–10.
[267] Lee JZ, Wynn TA, Schroeder MA, Alvarado J, Wang X, Xu K, et al. Cryogenic focused ion beam characterization of lithium metal anodes. ACS Energy Lett 2019;4:489–93.
[268] Cheng D, Lu B, Raghavendran G, Zhang M, Meng YS. Leveraging cryogenic electron microscopy for advancing battery design. Matter 2022;5:26–42.
[269] Chen Q, Koh AL, Robertson AW, He K, Lee S, Yoon E, et al. Rotating anisotropic crystalline silicon nanoclusters in graphene. ACS Nano 2015;9:9497–506.
[270] Egerton RF. Electron Energy-Loss Spectroscopy in the Electron Microscope. 3rd edn. Springer; 2011.
[271] Jäger W, Mayer J. Energy-filtered transmission electron microscopy of Si_mGe_n superlattices and Si-Ge heterostructures. I. Experimental results. Ultramicroscopy 1995;59:3–45.
[272] Hofer F, Grogger W, Kothleitner G, Warbichler P. Quantitative analysis of EFTEM elemental distribution images. Ultramicroscopy 1997;67:83–103.
[273] Ahn CC. Transmission Electron Energy Loss Spectrometry in Materials and the EELS Atlas. 2nd edn. Wiley-VCH; 2004.
[274] Verbeeck J, Van Dyck D, Van Tendeloo G. Energy-filtered transmission electron microscopy: an overview. Spectrochimica Acta B 2004;59:1529–34.
[275] Jeanguillaume C, Trebbia P, Colliex C. About the use of electron energy-loss spectroscopy for chemical mapping of thin foils with spatial resolution. Ultramicroscopy 1978;3:237–42.
[276] Kothleitner G, Hofer F. Optimization of the signal to noise ratio in EFTEM elemental maps with regard to different ionization edge types. Micron 1998;29:349–57.
[277] Freitag B, Mader W. Element specific imaging with high lateral resolution: an experimental study on layer structures. J Microscopy 1999;194:42–57.
[278] Walther T. Electron energy-loss spectroscopic profiling of thin film structures: 0.39 nm line resolution and 0.04 eV precision measurement of near-edge structure shifts at interfaces. Ultramicroscopy 2003;96:40–411.
[279] Kabius B, Hartel P, Haider M, Müller H, Uhlemann S, Loebau U, et al. First application of Cc-corrected imaging for high-resolution and energy-filtered TEM. J Electron Microsc 2009;58:147–55.
[280] Urban KW, Mayer J, Jinschek JR, Neish MJ, Lugg NR, Allen LJ. Achromatic elemental mapping beyond the nanoscale in the transmission electron microscope. Phys Rev Lett 2013;110:185507.
[281] Forbes BD, Houben L, Mayer J, Dunin-Borkowski RE, Allen LJ. Elemental mapping in achromatic atomic-resolution energy-filtered transmission electron microscopy. Ultramicroscopy 2014;147:98–105.
[282] Howie A. Inelastic scattering of electrons by crystals. I. The theory of small-angle inelastic scattering. Proc Roy Soc A 1963;271:268–87.
[283] Stallknecht P, Kohl H. Computation and interpretation of contrast in crystal lattice images formed by inelastically scattered electrons in a transmission electron microscope. Ultramicroscopy 1996;261:261–75.
[284] Lugg N, Freitag B, Findlay SD, Allen LJ. Energy-filtered transmission electron microscopy based on inner-shell ionization. Ultramicroscopy 2010;110:981–90.
[285] Coene W, Van Dyck D. Inelastic scattering of high-energy electrons in real space. Ultramicroscopy 1990;33:261–7.
[286] Forbes BD, Martin AV, Findlay SD, D'Alfonso AJ, Allen LJ. Quantum mechanical model for phonon excitation in electron diffraction and imaging using a Born-Oppenheimer approximation. Phys Rev B 2010;82:104103.